

AD 738862

**MEASUREMENTS OF DYNAMIC PROPERTIES OF MATERIALS**  
**Volume IV**  
**ALPHA TITANIUM**  
**FINAL REPORT**

by  
D. R. Christman  
T. E. Michaels  
W. M. Isbell  
S. G. Babcock

*Details of illustrations in  
this document may be better  
studied on microfiche*

Materials and Structures Laboratory  
Manufacturing Development, General Motors Corporation  
General Motors Technical Center, Warren, Michigan 48090

Prepared For  
HEADQUARTERS  
Defense Nuclear Agency  
Washington, D.C. 20305

Under Contract DASA01-JB-C-0134

D O C  
RECEIVED  
MAR 21 1972  
REC'D

Approved for public release; distribution unlimited

reproduced by  
**NATIONAL TECHNICAL  
INFORMATION SERVICE**  
Springfield, Va. 22151

**MEASUREMENTS OF DYNAMIC PROPERTIES OF MATERIALS**  
**Volume IV**  
**ALPHA TITANIUM**  
**FINAL REPORT**

“ This work was supported by the Defense Nuclear Agency under NWER Subtask AA 106”

by

D. R. Christman  
T. E. Michaels  
W. M. Isbell  
S. G. Babcock

Materials and Structures Laboratory  
Manufacturing Development, General Motors Corporation  
General Motors Technical Center, Warren, Michigan 48090

\*Presently with Lawrence Livermore Laboratory, Livermore, California

Prepared For  
HEADQUARTERS  
Defense Nuclear Agency  
Washington, D.C. 20305

*Details of illustrations in  
this document may be better  
studied on microfiche*

Under Contract DASA01-68-C-0114

“ Approved for public release; distribution unlimited”

## ABSTRACT

Results of an experimental study on the dynamic properties of alpha titanium are presented. Areas studied included stress-strain-strain rate and reverse loading behavior, elastic constants, equation of state, compressive and release wave characteristics, and spall fracture. The material showed approximately elastic-plastic behavior with some strain hardening under uniaxial stress compression (0.005 to 1000/sec strain rates). The material also exhibited strain-rate sensitivity which was temperature dependent. Longitudinal and shear wave velocities at 20°C were 6.118 and 3.246 mm/μsec, and temperature and pressure dependence was also measured and various elastic constants were calculated. The shock wave equation of state (EOS) up to 90 kbar was determined as  $\sigma_H = 2.5 + 225 u_p + 49.9 u_p^2$ . Shock wave measurements indicate a possible phase change between 90 and 125 kbars. The EOS was also calculated from the elastic constants and comparisons made with the shock wave EOS. Compressive wave tests showed an elastic-plastic wave structure with a well-defined precursor. The impact velocity required for spall fracture was found to increase with decreasing pulse width, and to increase with increasing temperature.

FOREWORD

The prediction of reentry vehicle response to impulsive loading resulting from energy deposition has been studied extensively during the last decade. Analytical models and computer routines have been developed to assess the vulnerability of such vehicles to the initial loading phase, in which stress waves are generated and propagated through the structure, and to subsequent phases, where elastic vibration, plastic deformation and/or fracture may occur.

A Defense Nuclear Agency (DNA) program was initiated with the objective of improving computer codes for the prediction of damage induced by X-rays (PREDIX). The PREDIX metals program has combined the efforts of several contractors under the direction of DNA. The primary contributions of each contractor can be summarized as follows:

General Motors Corporation--Measurement of material properties, including stress-strain-strain rate behavior, elastic constants, equations of state, shock wave profiles and spall fracture.

Effects Technology Inc.--Spall fracture tests and analysis (exploding foil) and underground testing.

KMS Technology Center--Constitutive modeling.

Physics International Company--Energy deposition and spall fracture studies (electron beam).

Systems, Science and Software--Energy deposition and front surface phenomena, constitutive modeling and code development, and underground testing.



## TABLE OF CONTENTS

	<u>Page</u>
ABSTRACT	iii
FOREWORD	iv
LIST OF ILLUSTRATIONS	vii
LIST OF SYMBOLS	xi
INTRODUCTION	1
SECTION I - MATERIAL PROPERTIES	3
SECTION II - STRESS-STRAIN STUDIES	8
Uniaxial Stress Tests	8
Reverse Loading Tests	14
SECTION III - ELASTIC BEHAVIOR	16
Wave Velocity Measurements	16
Elastic Constants	18
Gruneisen Parameter	19
Debye Temperature	22
SECTION IV - EQUATION OF STATE	24
Shock Wave Equation of State	24
Ultrasonic Equation of State	33
Yield Behavior	37
Metallographic Studies	39
SECTION V - WAVE PROPAGATION	44
Compressive Wave Behavior	44
Release Waves and Wave Attenuation	53

MSL-70-23, Vol. IV

TABLE OF CONTENTS (Continued)

	<u>Page</u>
SECTION VI - SPALL FRACTURE	60
Recovery Tests	60
Spall Profiles	72
SUMMARY	77
ACKNOWLEDGMENTS	80
REFERENCES	81
APPENDIX A - ELASTIC CONSTANTS EQUATIONS	88
APPENDIX B - GRUNEISEN PARAMETER ESTIMATES	92
APPENDIX C - GRUNEISEN PARAMETER, PRESSURE DERIVATIVE	96
APPENDIX D - DEVIATORIC STRESS ESTIMATES	99
APPENDIX E - EQUATIONS OF STATE, ULTRASONICS	102
APPENDIX F - WAVE PROFILES	105
DISTRIBUTION LIST	121
DD FORM 1473 DOCUMENT CONTROL DATA - R&D	128

## LIST OF ILLUSTRATIONS

<u>Figure</u>		<u>Page</u>
1	Alpha Titanium Grain Structure, 3.2 mm and 12.7 mm Stock	5
2	Alpha Titanium Grain Structure, 6.4 mm Stock	5
3	As-received and Annealed Alpha Titanium	6
4	Compressive Stress vs. Strain, Titanium	9
5	Compressive Stress vs. Log Strain Rate, Titanium	11
6	Compressive Stress vs. Strain, Stock Dependence, Titanium (20°C)	12
7	Tensile Stress vs. Strain, Titanium	13
8	Tensile Yield Stress vs. Log Strain Rate, Titanium	14
9	Reverse Loading Behavior for Titanium, Strain Effects	15
10	Quartz Gage Records, Titanium	25
11	Streak Camera Record, "Hat" Target	27
12	Stress-Particle Velocity Hugoniot, Titanium	29
13	Stress or Mean Pressure-Compression Hugoniot, Titanium	30
14	Shock Velocity-Particle Velocity Hugoniot, Titanium	31
15	X-ray Diffraction Patterns, Titanium (CuK $\alpha$ Radiation, Ni Filter)	32
16	Titanium Microstructure, As-Received and Shocked (12.7 mm Plate)	40

MSL-70-23, Vol. IV

## LIST OF ILLUSTRATIONS (Continued)

<u>Figure</u>		<u>Page</u>
17	Titanium Microstructure, Shocked (12.7 mm Plate)	40
18	Titanium Microstructure, Shocked to 40 kbar (12.7 mm Plate)	41
19	As-Received Titanium Foil, Trans- mission Electron Micrographs	42
20	Shocked (39 kbar) Titanium Foil, Transmission Electron Micrographs	42
21	Compressive Waves, Propagation Distance Dependence (3.2 mm and 6.4 mm Stock)	45
22	Compressive Waves, Propagation Distance Dependence (25.4 mm Stock)	46
23	Compressive Waves, As-Received and Annealed Material (12.7 mm Stock)	48
24	Compressive Waves, Peak Stress Dependence (25.4 mm Stock)	49
25	Elastic Precursor Decay in Titanium	51
26	Compressive Waves, Material Differences	52
27	Complete Wave Profile, Titanium	54
28	Wave Attenuation in Titanium, Low Pressure	56
29	Wave Attenuation in Titanium, High Pressure	57
30	Peak Stress Attenuation in Titanium	59
31	Spall Data for Titanium, 3.2 mm Stock (20°C)	63
32	Spall Data for Titanium (20°C)	64

## LIST OF ILLUSTRATIONS (Continued)

<u>Figure</u>		<u>Page</u>
33	Spall Fractures in Titanium, 3.2 mm Stock (20°C)	66
34	Spall Fractures in Titanium, 12.7 mm Stock (20°C)	67
35	Spall Fractures in Titanium, Material Effects (1 mm → 2 mm, 20°C)	67
36	Spall Fracture Surfaces in Titanium, Material Effects (20°C)	68
37	Spall Fracture Surface in Titanium, 3.2 mm Stock (0.5 mm → 1 mm, 20°C)	69
38	Spall Data for Titanium, Temperature Effect (1 mm → 2 mm, 3.2 mm Stock)	70
39	Spall Fractures in Titanium, Temperature Effects (1 mm → 2 mm, 3.2 mm Stock)	71
40	Spall Fractures in Titanium, Temperature Effects (1 mm → 2 mm, 3.2 mm Stock)	71
41	Spall Fracture Surfaces in Titanium, Temperature Effects (1 mm → 2 mm, 3.2 mm Stock)	72
42	Wave Interaction in Spall Test and Velocity-Time History	73
43	Spall Wave Profiles in Titanium	74
44	Measured and Calculated Spall Profiles, Titanium	75
45	Attenuated Spall Profile in Titanium	76

MSL-70-23, Vol. IV

## LIST OF TABLES

<u>Table</u>		<u>Page</u>
I	Alpha Titanium Chemical Composition	4
II	Alpha Titanium Mechanical Properties	4
III	Elastic Constants for Alpha Titanium (P = 0, T = 20°C)	20
IV	Equations of State Comparison-Hydrostat, Alpha Titanium	35
V	Velocity Interferometer Test Data, Alpha Titanium	55
VI	Incipient Spall Data for Alpha Titanium	62

LIST OF SYMBOLS

MSL-70-23, Vol. IV

$C_B$	Bulk Wave Velocity, mm/ $\mu$ sec
$C_L$	Longitudinal Wave Velocity, mm/ $\mu$ sec
$C_S$	Shear Wave Velocity, mm/ $\mu$ sec
$c_p$	Specific Heat, cal/g
$G$	Shear Modulus, kbar
$K$	Bulk Modulus, kbar
$P_H$	Mean Pressure, Hydrostat, kbar
$P_S$	Mean Pressure, Adiabatic, kbar
$P_T$	Mean Pressure, Isotherm, kbar
$T$	Temperature, $^{\circ}$ C
$U_S$	Shock Wave Velocity, mm/ $\mu$ sec
$u_p$	Particle Velocity, mm/ $\mu$ sec
$v$	Specific Volume, cc/g
$V_I$	Impact Velocity, mm/ $\mu$ sec
$X$	Target Thickness, mm
$X_O$	Impactor Thickness, mm
$X^S$	Adiabatic Modulus, kbar
$X^T$	Isothermal Modulus, kbar
$X_{OS}^{S'}$ , $X_{OS}^{T'}$	Adiabatic Pressure Derivative @ Zero Pressure $\left( = \left( \frac{\partial X^S}{\partial P} \right)_S \Big _{P=0} \right)$
$X_{OT}^{T'}$ , $X_{OT}^{S'}$	Isothermal Pressure Derivative @ Zero Pressure $\left( = \left( \frac{\partial X^T}{\partial P} \right)_T \Big _{P=0} \right)$
$\beta$	Volume Coefficient of Expansion, / $^{\circ}$ C $= - \frac{1}{v} \left( \frac{\partial v}{\partial T} \right)_{P=0}$
$\gamma$	Gruneisen Parameter
$u$	Compression $(= v_0/v - 1)$
$\nu$	Poisson's Ratio
$\rho$	Density, g/cc
$\sigma_H$	Stress, Hugoniot, kbar

## INTRODUCTION

This report is one of a series of six giving results of a study of dynamic properties of four metals. The principal objectives of this study were:

- Provide measurements of dynamic properties of materials to be used as inputs to model development for shock wave propagation and dynamic fracture.
- Provide data to establish accuracy of computer code predictions.
- Provide physical interpretation of experimentally observed material response to dynamic test conditions.

The primary areas studied included: (1) Stress-strain-strain rate behavior in uniaxial stress, including Bauschinger effect; (2) Elastic constants, including temperature and pressure dependence; (3) Hugoniot equation of state; (4) Compressive and release wave profiles, including elastic precursor decay and wave attenuation; and (5) Spall fracture studies, including pulse width dependence. The six reports in this series are:

- Vol. I: Summary of Results, DASA 2501-1 (AD712847)
- Vol. II: Experimental Methods and Techniques,  
DASA 2501-2 (AD 730750)
- Vol. III: 6061-T6 Aluminum, DASA 2501-3
- Vol. IV: Alpha Titanium, DASA 2501-4
- Vol. V: OFHC Copper, DASA 2501-5 (AD 728846)
- Vol. VI: Tantalum, DASA 2501-6



## MSL-70-23, Vol. IV

The experimental techniques utilized in this study are reviewed in Vol. II (DASA 2501-2). Briefly, the principal techniques applied were:

**Stress-strain Studies**--A laboratory-type universal testing machine was used for rates  $< 0.1/\text{sec}$ , a medium strain rate machine for rates of  $10^{-3}/\text{sec}$  to  $10^2/\text{sec}$ , and a Hopkinson bar device for rates of about  $10^2$  to  $5 \times 10^3/\text{sec}$ .

**Elastic Constants**--The pulse superposition method was used for measuring longitudinal and shear wave velocities as functions of temperature and hydrostatic pressure.

**Equation of State**--Gun-launched, flat-plate impact techniques were used to generate uniaxial strain conditions. Velocities up to  $0.6 \text{ mm}/\mu\text{sec}$  were achieved with 63.5 mm and 102 mm single-stage compressed-gas guns, and velocities of  $0.3$  to  $2 \text{ mm}/\mu\text{sec}$  were achieved with a 64 mm single-stage, powder gun. Hugoniot data were obtained with x-cut quartz gage and streak camera techniques.

**Wave Propagation and Spall Fracture**--Flat-plate impact techniques were also used. Wave profiles were measured with x-cut quartz gages and a laser velocity interferometer.

A literature search on dynamic properties of materials was carried out under the PREDIX program and a listing of recent publications (including abstracts) on dynamic properties of materials is given in Reference 1.

## SECTION I

## MATERIAL PROPERTIES

Alpha titanium has a hexagonal-close-packed structure and the type studied was commercially pure Grade 55 of 99+% purity. It is not heat treatable and different strength levels result from either slight changes in interstitial content or by cold-working. The material was purchased as sheet and plate stock in thicknesses of 1.6, 3.2, 6.4, 12.7 and 25.4 mm. Chemical composition is given in Table I and mechanical properties and grain size are given in Table II. Although all material was ordered to the Grade 55 specification, there were significant differences in composition and properties for the different thicknesses.

All except the 6.4 mm stock showed approximately equiaxed structure, although there was some variation in average grain size. Grain structure of the 3.2, 12.7 and 6.4 mm stock is shown in Figures 1 and 2. Note that the 6.4 mm stock shows "flattened" grains elongated in the rolling direction. Unless noted, all data reported are for a test direction normal to the plane of the sheet, e.g., vertical in Figures 1 and 2. Two pieces of 12.7 mm stock were annealed in a nitrogen atmosphere, one for 1 hour @ 540°C and the other for 2 hours @ 760°C. There was no change in microstructure as shown in Figure 3 and only a slight decrease in hardness.

The average measured density was 4.500 g/cc (0.1625 lb/in.<sup>3</sup>). For use in equation of state and energy deposition calculations,

MSL-70-23, Vol. IV

TABLE I  
ALPHA TITANIUM CHEMICAL COMPOSITION<sup>1</sup>

Stock (mm)	Element (Wt. Percent)				
	C	Fe	N <sub>2</sub>	H <sub>2</sub>	O <sub>2</sub>
1.6	0.04	0.27	0.015	0.0036	0.19
3.2	0.024	0.121	0.0177	0.0027	0.149
6.4	0.029	0.203	0.0059	0.0035	0.150
12.7	0.023	0.12	0.012	0.004	0.19
25.4	0.023	0.15	0.017	0.008	0.19

<sup>1</sup> Universal Titanium Company, Inc., test certification.

TABLE II  
ALPHA TITANIUM MECHANICAL PROPERTIES

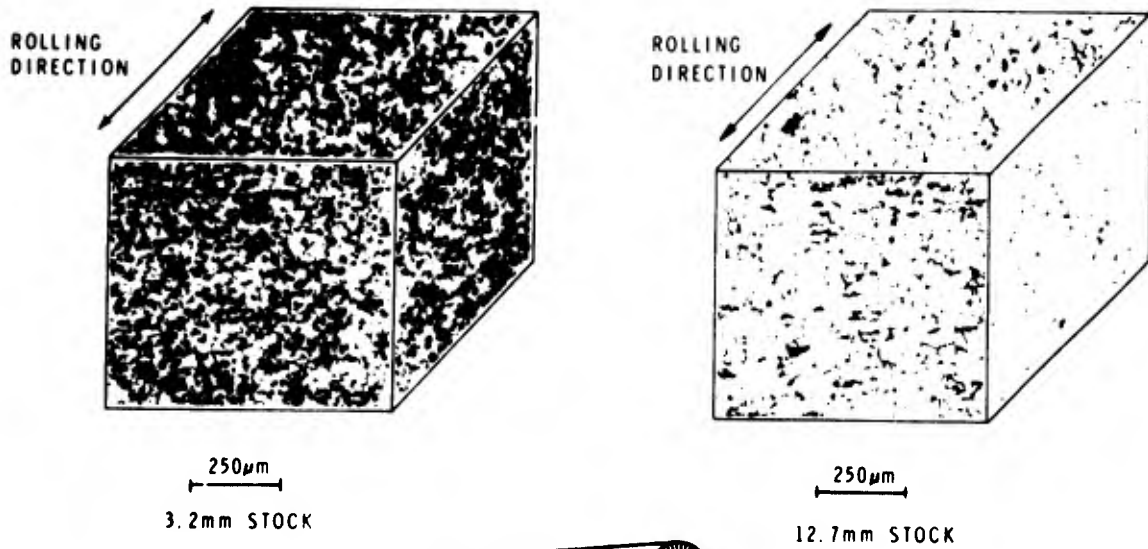
Stock (mm)	Tensile Yield Strength <sup>1</sup> (kbar)	Ultimate Tensile Strength <sup>1</sup> (kbar)	Percent Elong. <sup>1</sup> (2-in.)	Hardness		Avg. Grain Diameter (μm)
				R <sub>A</sub> <sup>2</sup>	Bhn <sup>3</sup>	
1.6	5.3	6.1	26	57	167	25
3.2	5.0	5.7	24	59	179	20
6.4	4.9	6.0	22	61	195	~15 <sup>4</sup>
12.7	4.0	5.5	24	59	179	40
25.4	4.2	5.9	28	55	154	40

<sup>1</sup> Universal Titanium Company, Inc., test certification, measured in the plane of the sheet.

<sup>2</sup> Measured.

<sup>3</sup> Estimated.

<sup>4</sup> Elongated grain structure.



Reproduced from  
best available copy. 

Figure 1 Alpha Titanium Grain Structure,  
3.2 mm and 12.7 mm Stock

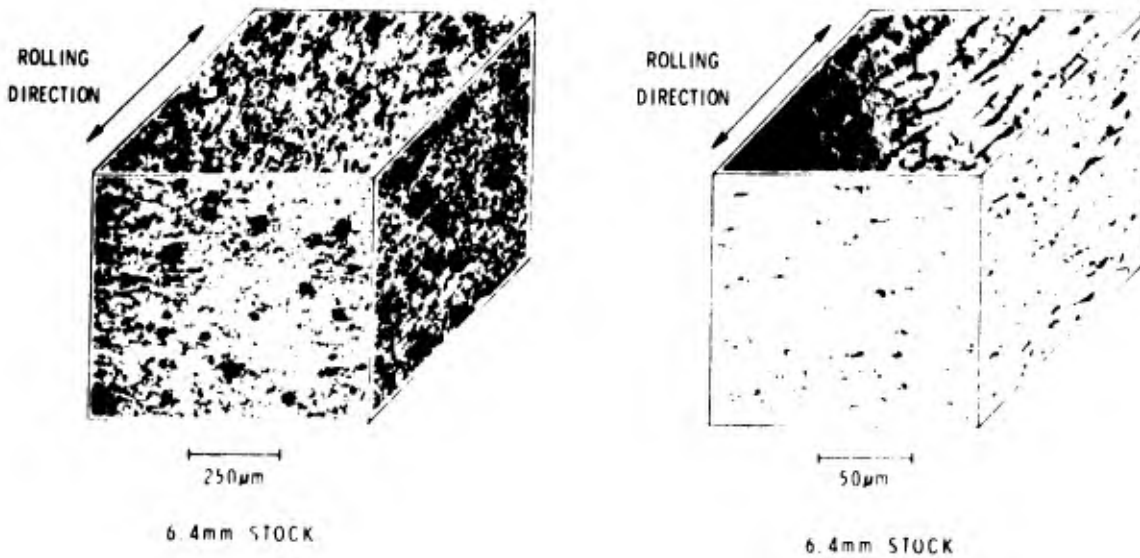


Figure 2 Alpha Titanium Grain Structure,  
6.4 mm Stock

MSL-70-23, Vol. IV

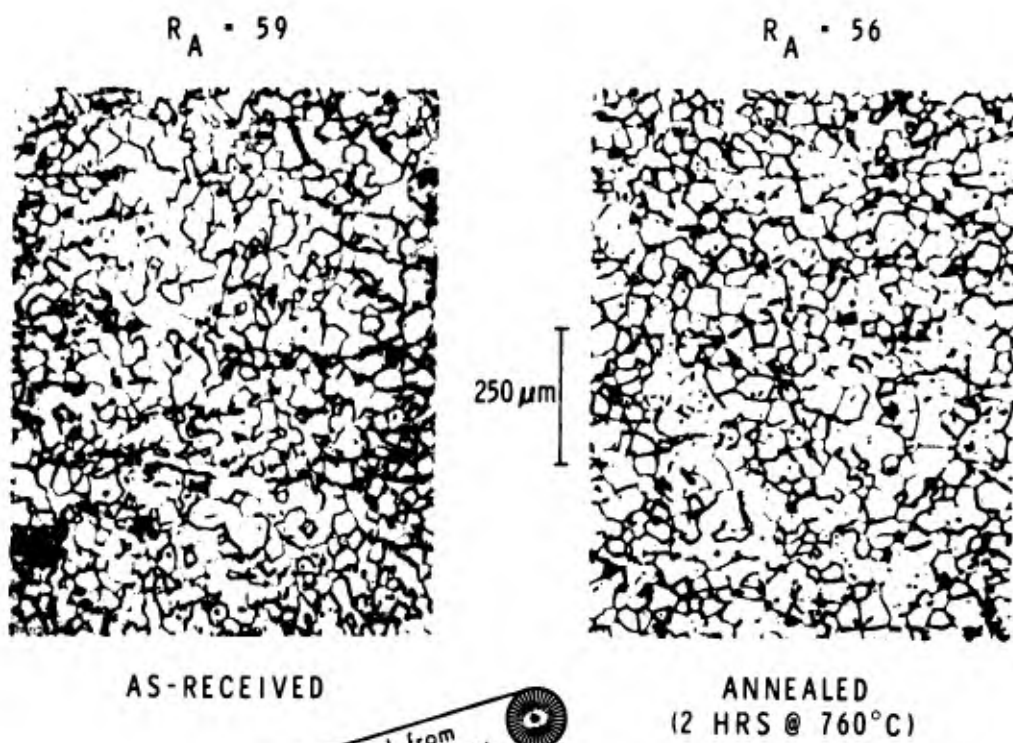


Figure 3 As-received and Annealed Alpha Titanium

several physical constants were compiled from the literature<sup>(2-7)</sup> and are listed below:

Volume coefficient of thermal expansion,  $\beta$ :

$$24.8 \times 10^{-6} + 0.0036 \times 10^{-6} T / ^\circ\text{C}$$

Specific heat,  $c_p$ :

$$0.124 + 0.00004 T \text{ cal/g-}^\circ\text{C}$$

Melting temperature:  $1670^\circ\text{C}$

Boiling temperature:  $3260^\circ\text{C}$

Latent heat of fusion:  $94 \text{ cal/g}$

Latent heat of vaporization:  $2014 \text{ cal/g}$

(T in  $^\circ\text{C}$ )

MSL-70-23, Vol. IV

## SECTION II

## STRESS-STRAIN STUDIES

Shock wave and structural response code input requirements include constitutive equations relating stress to strain, strain rate and temperature. Uniaxial stress tests at various strain rates and temperatures give yield and flow stress behavior, strain rate sensitivity and work hardening characteristics. Although it is recognized that heating rate and time-at-temperature, as well as final temperature, are important in assessing material properties under short-time ( $< 10^{-6}$  sec) energy deposition conditions,<sup>(8)</sup> data reported here are for relatively long heating times only. Bauschinger effect tests were conducted to provide information on unloading and subsequent yield.

## UNIAXIAL STRESS TESTS\*

Results of compressive stress-strain tests on alpha titanium are shown in Figure 4 for strain rates of 0.005/sec to 1100/sec and test temperatures of 20° and 370°C, with each curve the average of three tests. As noted, the heating rate for the 370°C tests was  $\sim 0.5^\circ\text{C}/\text{second}$ .

---

\* Deformation mechanisms of titanium (primarily under uniaxial stress conditions) have been studied by a number of other investigators. The reader is referred to the literature for details in such areas as anisotropy (Refs. 10-12), temperature effects (Refs. 13-20), strain rate effects (Refs. 17-22), stress relaxation (Refs. 17, 20, 23), grain size effects (Refs. 16, 20, 21, 24), impurity content (Refs. 16, 18) twinning (Refs. 11, 12, 25), and fracture (Refs. 16, 26, 27).

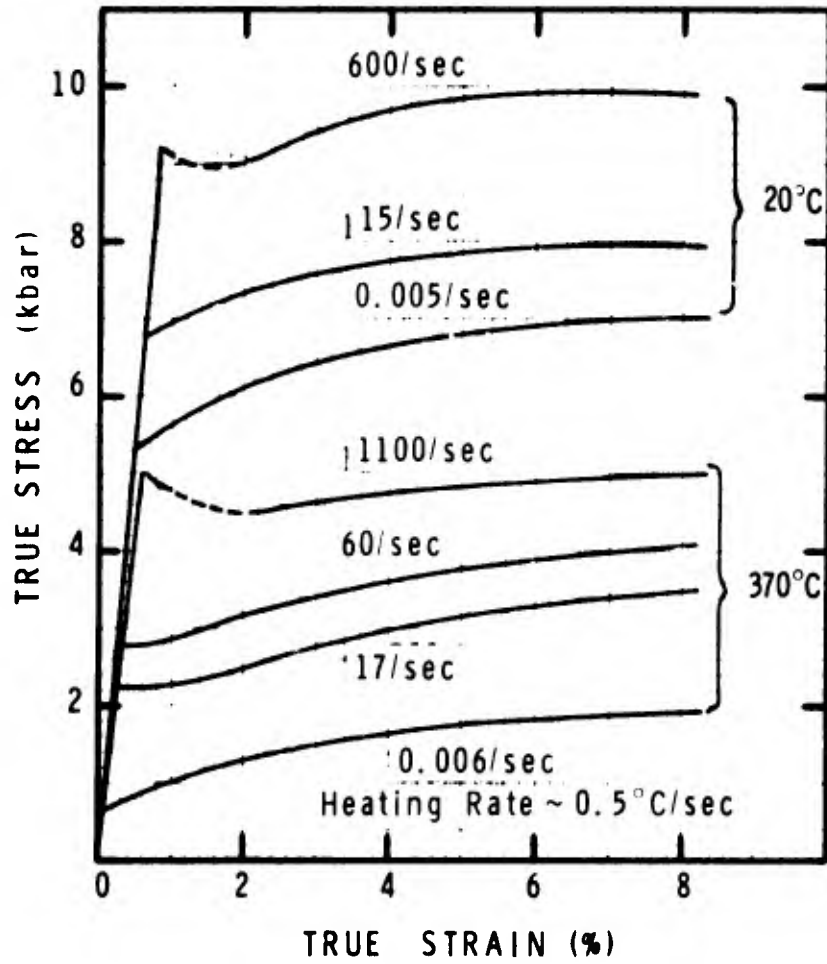


Figure 4 Compressive Stress vs. Strain, Titanium



## MSL-70-23, Vol. IV

This material shows significant rate sensitivity at 20°C (as opposed to 6061-T6 aluminum which is rate insensitive at 20°C<sup>(9)</sup>). At 370°C, the rate sensitivity is about the same as at 20°C on an absolute scale, but is much greater on a percentage basis since the yield and flow stress have decreased. An apparent yield drop (or stress relaxation) was observed at the highest rate at 20°C, while at 370°C some relaxation is evident above  $\sim 10$ /second. This relaxation is shown with a dashed line at the highest rate because these results are from Hopkinson bar tests, and interpretation of stress-strain behavior is difficult at small ( $< 2\%$ ) strains.

The results in Figure 4 are for 9.5 mm diameter by 12.7 mm long specimens taken from 12.7 mm stock with the loading direction normal to the plane of the plate. Additional tests were conducted on specimens taken with axis parallel to the rolling direction. Results are compared in Figure 5 with stress at yield and at 6% strain plotted against log strain rate. Loading normal to the plate (propagation direction for shock wave tests reported below) gave higher yield and flow stress, with the differences increasing at higher strain rates. Anisotropy of rolled titanium can also be significant in the plane of the sheet, i.e., it may not be transversely isotropic in this plane.<sup>(11,12)</sup> The shaded areas in Figure 5 represent the boundary for characterizing this particular material for loading in any direction.

The stress-strain behavior of specimens from three different sheets (3.2, 6.4 and 12.7 mm) is compared in Figure 6 for 0.005/sec and 20°C (all tests normal to the plane of the sheet). Yield data shows a correlation with grain size (with the highest yield and flow stress corresponding to the smallest grain diameter), but correlation of macrohardness with grain size is inconclusive.

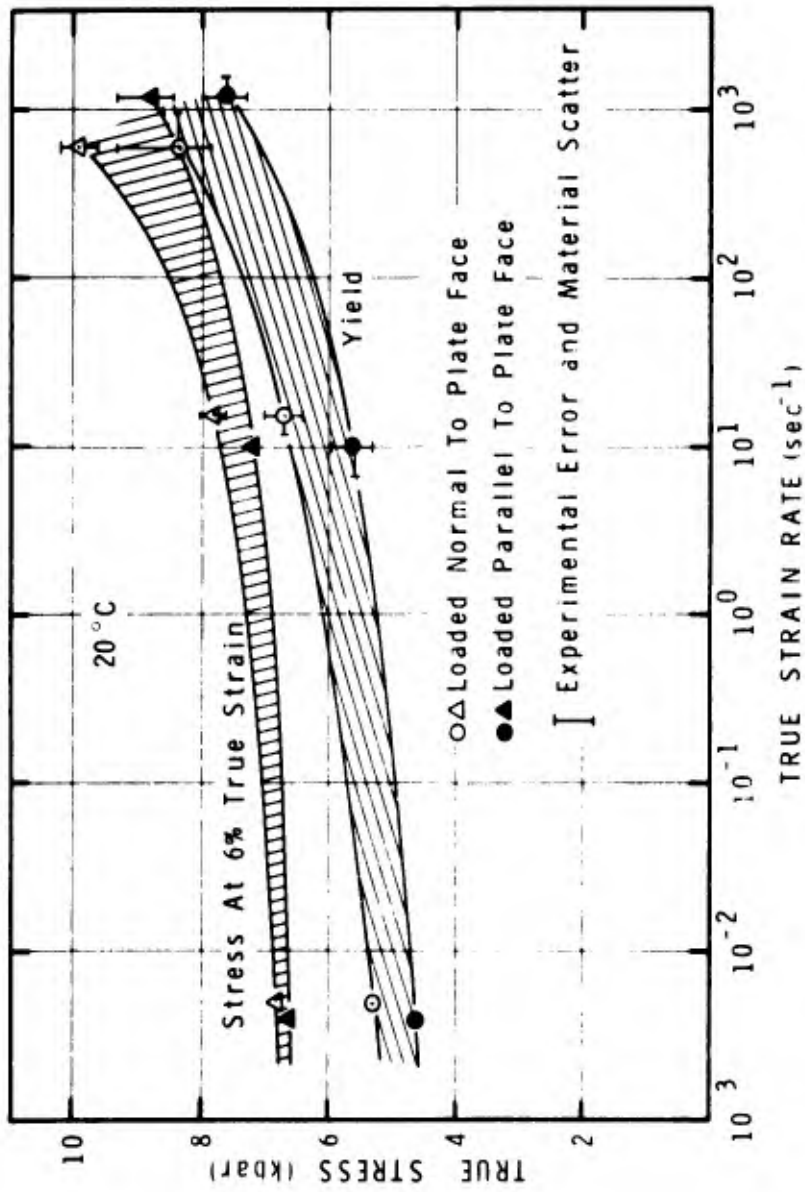


Figure 5 Compressive Stress vs. Log Strain Rate, Titanium

MSL-70-23, Vol. IV

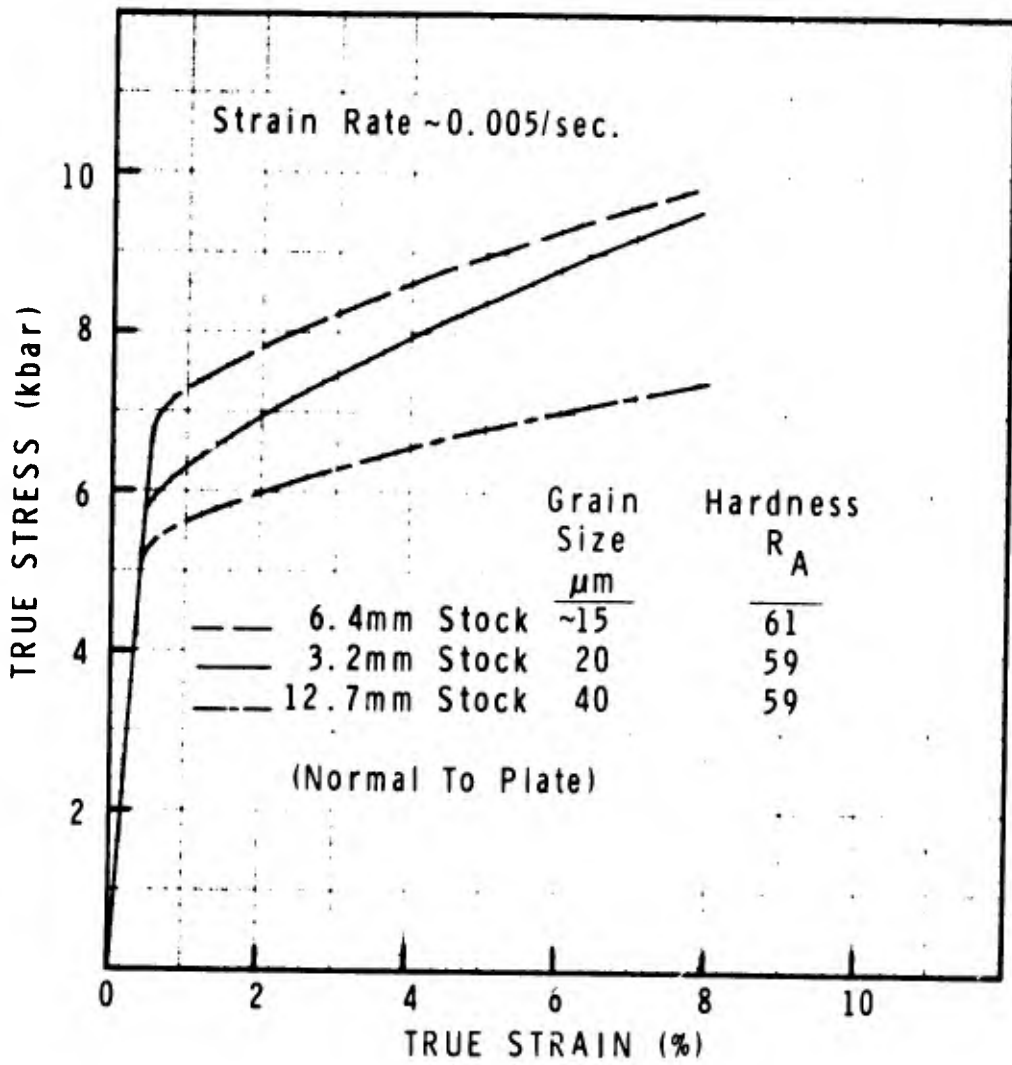


Figure 6 Compressive Stress vs. Strain, Stock Dependence, Titanium (20°C)

Tensile tests were conducted on specimen taken from 12.7 mm stock with the test direction parallel to the rolling direction and results are given in Figure 7. The rate sensitivity and temperature effects are comparable to those found for compression. The yield data from Figure 7, plus additional results from tests at intermediate temperatures, are plotted in Figure 8 as a function of log strain rate.

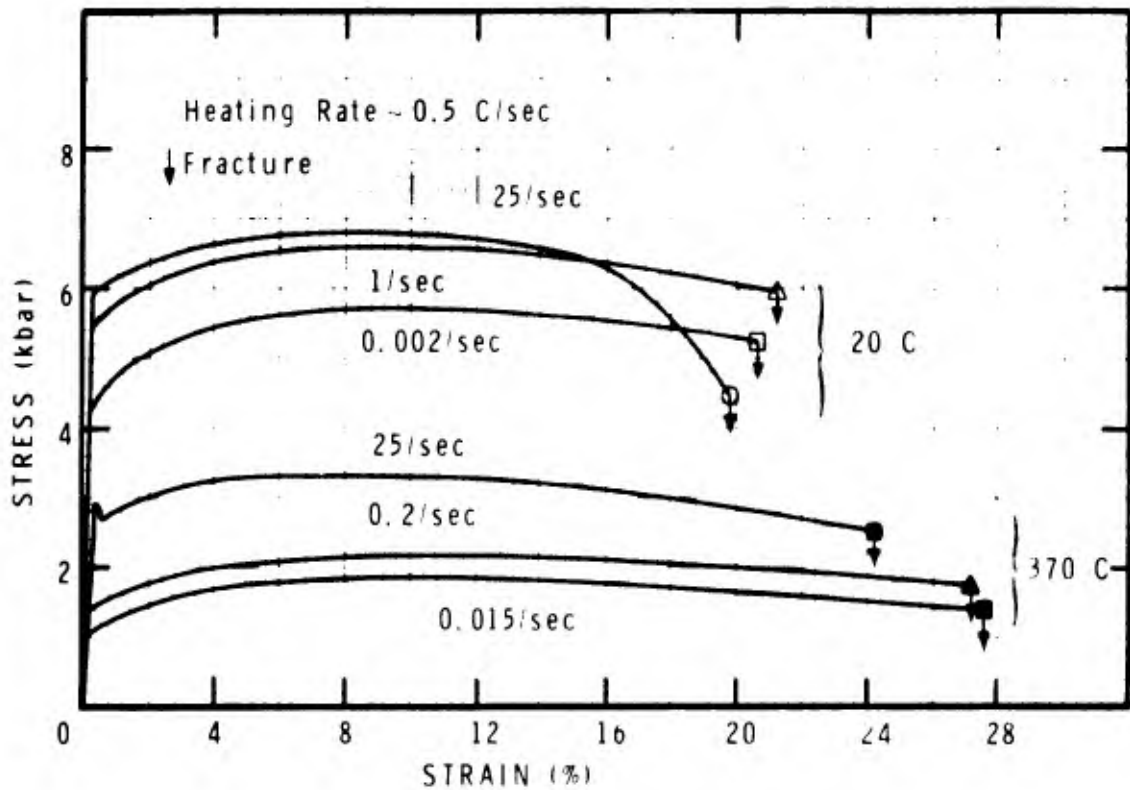


Figure 7 Tensile Stress vs. Strain, Titanium

MSL-70-23, Vol. IV

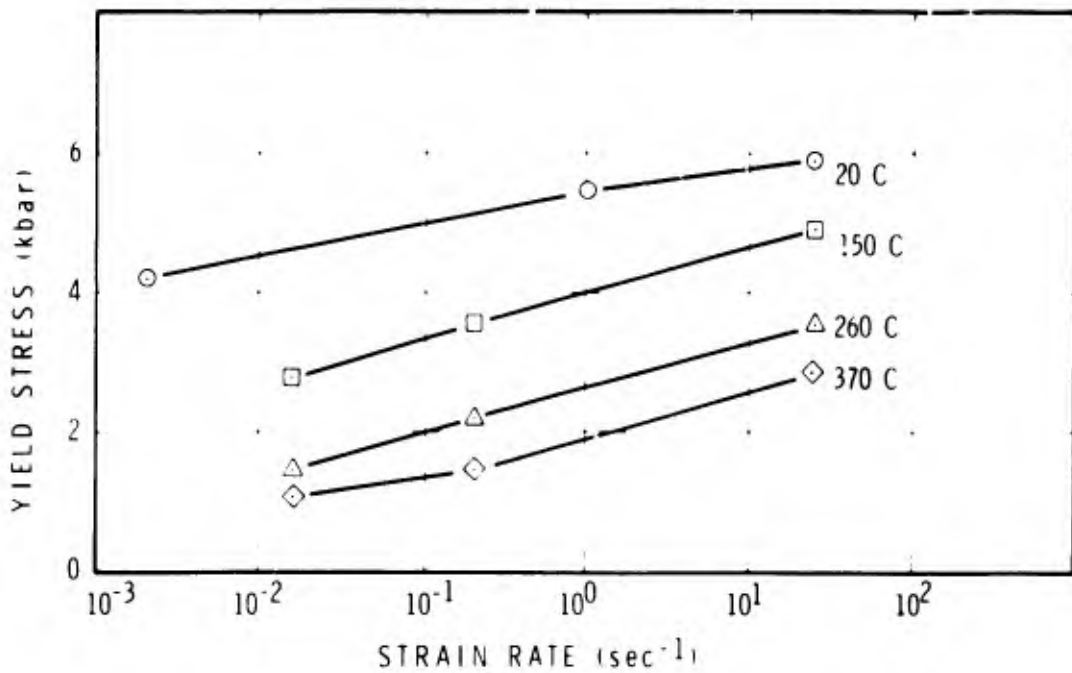


Figure 8 Tensile Yield Stress vs. Log Strain Rate, Titanium

#### REVERSE LOADING TESTS

The reverse loading behavior or Bauschinger effect was studied by performing uniaxial tensile stress tests after the material had been prestrained in the opposite (compressive) sense. Results from low strain rate ( $\sim 0.001/\text{sec}$ ) tests are given in Figure 9 and show the reduction in yielding when the load is reversed. The Bauschinger strain (defined here as the plastic strain in the reverse loading path at 3/4 of the initial yield stress) is insensitive to compressive prestrain, at least up to 3%. The rate of work hardening is slightly lower on tensile reloading than on the initial compressive loading.

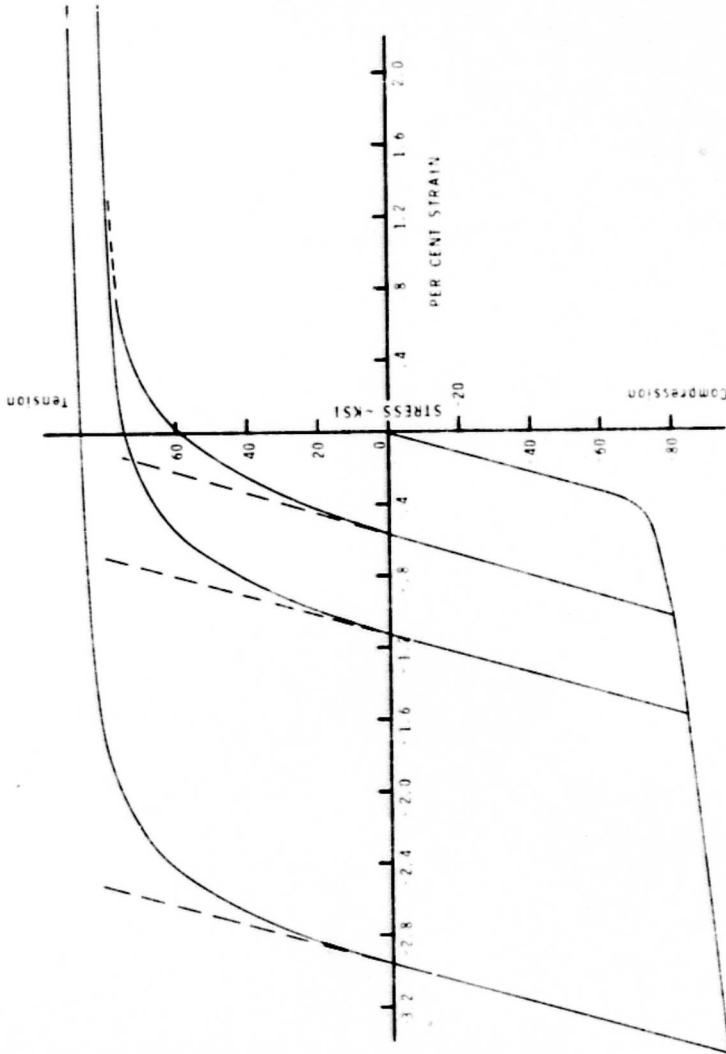


Figure 9 Reverse Loading Behavior for Titanium, Strain Effects

MSL-70-23, Vol. IV

## SECTION III

## ELASTIC BEHAVIOR

Measurement of elastic constants provides additional inputs to the study of material response. Three basic measurements are density, longitudinal (dilatational) wave velocity and shear (transverse) wave velocity. Measurements of temperature and pressure dependence of the wave velocities lead to prediction of pressure-compression isotherms, adiabats and hydrostats. If these measurements are made with sufficient accuracy ( $\sim 0.1\%$ ), the calculated pressure-compression behavior can frequently be extrapolated with reasonable confidence to higher pressures than covered in the actual measurements.

## WAVE VELOCITY MEASUREMENTS

Initial measurements of longitudinal and shear wave velocities were made at 20°C and atmospheric pressure (i.e.,  $P = 0$ ). Values obtained normal to the plane of the plate for 25.4 mm stock were:

$$C_L = 6.118 \pm 0.006 \text{ mm}/\mu\text{sec}$$

$$C_S = 3.246 \pm 0.003 \text{ mm}/\mu\text{sec}$$

Although the accuracy of these measurements are estimated to be about  $\pm 0.1\%$ , it should be noted that  $C_L$  and  $C_S$  may vary depending on the structural form of the material (i.e., plate, bar, etc.), its thermal and mechanical history, and the measurement direction relative to any structural anisotropy. For

example, Seaman, et al.<sup>(28)</sup>, reported  $C_L$  and  $C_S$  for grade 50A alpha titanium plate at room temperature. Normal to the plate gave  $C_L = 6.18$  mm/ $\mu$ sec and  $C_S = 3.13$  mm/ $\mu$ sec. In the plane of the plate, they found  $C_L = 6.12$  mm/ $\mu$ sec and  $C_S = 3.00$  mm/ $\mu$ sec in the rolling direction and  $C_L = 6.02$  mm/ $\mu$ sec and  $C_S = 2.99$  mm/ $\mu$ sec transverse to the rolling direction. Although it is recognized that elastic anisotropy as well as plate-to-plate variation exist for alpha titanium, it will be assumed that these variations have a negligible effect on wave propagation and the elastic constant calculations given below will be for an isotropic material.

Measurements were made of the temperature and hydrostatic pressure dependence of the wave velocities and the data corrected for thermal expansion and hydrostatic compression to give:

Temperature Dependence, 0-100°C, P = 0

$$C_L = 6.135 - 0.00083T \text{ mm}/\mu\text{sec}$$

$$C_S = 3.261 - 0.00076T \text{ mm}/\mu\text{sec}$$

(T in °C)

Pressure Dependence, 0-9 kbar, T = 20°C

$$C_L = 6.118 + 0.0056P \text{ mm}/\mu\text{sec}$$

$$C_S = 3.246 + 0.00104P \text{ mm}/\mu\text{sec}$$

(P in kbar)



MSL-70-23, Vol. IV

## ELASTIC CONSTANTS

Assuming polycrystalline alpha titanium\* is isotropic ( $C_L$  and  $C_S$  are independent of direction of measurement in a polycrystalline specimen), wave velocity data are used to calculate various elastic constants. At 20°C and zero pressure, the following adiabatic constants were obtained (see Appendix A):

Bulk wave velocity,  $C_B = 4.83$  mm/μsec  
 Sound wave velocity,  $C_E = 5.24$  mm/μsec  
 Rayleigh wave velocity,  $C_R = 3.03$  mm/μsec  
 Poisson's ratio,  $\nu = 0.304$   
 Bulk modulus,  $K = 1056$  kbar  
 Shear modulus,  $G = 479$  kbar  
 Elastic modulus,  $E = 1237$  kbar  
 Lamé's parameter,  $\lambda = 736$  kbar

The bulk and shear moduli are used in the development of the ultrasonic equation of state. They were obtained first as functions of T and P from the following:

$$K = \rho \left( C_L^2 - \frac{4}{3} C_S^2 \right) \quad (1)$$

$$G = \rho C_S^2 \quad (2)$$

---

\* The elastic moduli for single-crystal titanium have been reported by Fisher and Renken<sup>(29)</sup> as a function of temperature. At 20°C, they give  $C_{11} = 1627$ ,  $C_{33} = 1809$ ,  $C_{44} = 468$ ,  $C_{13} = 690$  and  $C_{12} = 918$  (all in kbars). The use of these moduli in determining the stiffness of polycrystalline titanium sheet is discussed by Morris.<sup>(10)</sup>

This gave:

Temperature dependence,  $P = 0$

$$K^S = 1056 - 0.187T \text{ kbar}$$

$$G^S = 479 - 0.235T \text{ kbar}$$

Pressure dependence,  $T = 20^\circ\text{C}$

$$K^S = 1052 + 3.65P \text{ kbar}$$

$$G^S = 474 + 0.75P \text{ kbar}$$

where the superscript S indicates adiabatic.

Finally, isothermal values of K and G as well as adiabatic and isothermal pressure and temperature derivatives at  $20^\circ\text{C}$  and zero pressure were calculated using the equations given in Appendix A. Results are given in Table III. Use of these constants in calculating the isotherm, adiabat and hydrostat is discussed in the section on Ultrasonic Equation of State.

#### GRUNEISEN PARAMETER

The Gruneisen ratio  $\gamma$  is a parameter in the solid equation of state relating pressure to volume and energy,  $\gamma = V (\partial P / \partial E)_V$  (see, e.g., Ref. 30). This parameter can be expressed thermodynamically as:

$$\gamma = - \frac{1}{\rho c_p} \left( \frac{\partial V}{\partial T} \right)_P \left( \frac{\partial P}{\partial V} \right)_S = \frac{P K^S}{\rho c_p} \quad (3)$$

MSL-70-23, Vol. IV

TABLE III

ELASTIC CONSTANTS FOR ALPHA TITANIUM

(P = 0, T = 20°C)

PARAMETER	VALUE
$K^S$	1052 kbar
$(\frac{\partial K^S}{\partial P})_T = K_{0T}^{S'}$	3.68
$(\frac{\partial K^S}{\partial T})_P$	-0.187 kbar/°C
$(\frac{\partial K^S}{\partial P})_S = K_{0S}^{S'}$	3.62
$(\frac{\partial K^S}{\partial T})_S$	11.5 kbar/°C
$K^T$	1043 kbar
$(\frac{\partial K^T}{\partial P})_T = K_{0T}^{T'}$	3.76
$(\frac{\partial K^T}{\partial T})_P$	-0.215 kbar/°C
$(\frac{\partial K^T}{\partial P})_S = K_{0S}^{T'}$	3.70
$(\frac{\partial K^T}{\partial T})_S$	11.8 kbar/°C
$G^S = G^T$	474 kbar
$(\frac{\partial G}{\partial P})_T = G_{0T}'$	0.75
$(\frac{\partial G}{\partial T})_P$	-0.234 kbar/°C
$(\frac{\partial G}{\partial P})_S = G_{0S}'$	0.68
$(\frac{\partial G}{\partial T})_S$	2.18 kbar/°C

For an isotropic elastic solid, this gives:

$$\gamma = \frac{\beta}{c_p} \left( c_L^2 - \frac{4}{3} c_S^2 \right) \quad (4)$$

where  $c_L$  and  $c_S$  are measured under adiabatic conditions.

At 20°C and zero pressure:

$$\gamma_0 = 1.11$$

The zero-pressure Gruneisen parameter can also be estimated by several other methods, including those of Slater<sup>(31)</sup>, Dugdale and MacDonald<sup>(32)</sup>, Anderson and Dienes<sup>(33,34)</sup>, and Schuele and Smith<sup>(33,35)</sup>. These methods are discussed in Appendix B.

An estimate of the temperature dependence of the Gruneisen parameter can be obtained by differentiating Equation 3 with respect to temperature. At constant pressure ( $P = 0$ ,  $T = 20^\circ\text{C}$ ):

$$\left( \frac{\partial \gamma}{\partial T} \right)_P = \gamma_0 \left[ \frac{1}{\beta} \left( \frac{\partial \beta}{\partial T} \right)_P + \frac{1}{K^S} \left( \frac{\partial K^S}{\partial T} \right)_P - \frac{1}{c_p} \left( \frac{\partial c_p}{\partial T} \right)_P - \frac{1}{c_p} \left( \frac{\partial c_p}{\partial T} \right)_P \right] = - 0.00036/^\circ\text{C} \quad (5)$$

The pressure dependence can be estimated by differentiating with respect to pressure (see Appendix C). At constant temperature ( $T = 20^\circ\text{C}$ ,  $P = 0$ ):

MSL-70-23, Vol. IV

$$\left(\frac{\partial \gamma}{\partial P}\right)_T = \frac{\gamma_0}{K^S} \left[ \left(\frac{\partial K^S}{\partial P}\right)_T + \frac{1}{\beta K^T} \left(\frac{\partial K^S}{\partial T}\right)_P - 1 - \gamma - T \left(\frac{\partial \gamma}{\partial T}\right)_P \right] = -0.0058/\text{kbar} \quad (6)$$

Another approach is to assume  $\gamma/V$  constant, which permits  $(\partial \gamma / \partial P)_T$  to be estimated directly from the bulk modulus data (see Appendix C). At constant temperature (20°C):

$$\begin{aligned} \left(\frac{\partial \gamma}{\partial P}\right)_T &= \frac{-\gamma_0}{\left(\frac{1}{K_0^T}\right) \left(1/K_{0T}^{T'}\right) \left(K_0^T + K_{0T}^{T'P}\right) \left(1+K_{0T}^{T'}\right) / K_{0T}^{T'}} \\ &= \frac{-7.05}{(1043+3.76P)^{1.266}} \\ &= -0.00106/\text{kbar} @ P = 0 \\ &= -0.00086/\text{kbar} @ P = 50 \text{ kbar} \end{aligned} \quad (7)$$

#### DEBYE TEMPERATURE

The Debye temperature  $\theta$  is important in thermal energy calculations and indicates the temperature above which variations due to temperature for some thermodynamic parameters such as  $\gamma/V$  and  $\alpha$  are small. It also indicates the temperature above which variations due to temperature for some thermodynamic parameters such as

specific heat, thermal expansion and Gruneisen ratio become small. There are a number of methods for calculating the Debye temperature<sup>(36)</sup>, and one approximation suitable for use with elastic wave velocity data for polycrystalline metals is:

$$\theta = \frac{h}{k} \left( \frac{9N}{4\pi V} \right)^{1/3} \left( \frac{1}{C_L^3} + \frac{2}{C_S^3} \right)^{-1/3}$$

where h is Planck's constant, k is Boltzmann's constant, N is number of mass points and V is sample volume.

At 20°C, the elastically-determined Debye temperature for alpha titanium is:

$$\theta = 4.3 \times 10^{-5} \left( \frac{N}{V} \right)^{1/3} \left( \frac{1}{C_L^3} + \frac{2}{C_S^3} \right)^{-1/3} \quad (8)$$

$$\theta = 415^\circ\text{K}$$

for  $N = 2$  (atoms per unit cell),  $V^* = 35.3 \times 10^{-21} \text{ mm}^3$ ,  
 $C_L = 6.118 \text{ mm}/\mu\text{sec}$  and  $C_S = 3.246 \text{ mm}/\mu\text{sec}$ .

---

\* The unit cell volume =  $0.866a^2c$ , where  $a = 2.9504\text{\AA}$   
 $c = 4.6833\text{\AA}$ . (37)

MSL-70-23, Vol. IV

## SECTION IV

## EQUATION OF STATE

The development of material response models and computational codes requires data on material behavior under uniaxial strain conditions, including equation of state, wave propagation and spall fracture. Most data are used directly in developing models of material behavior, although independent check data (attenuated wave shapes and spall wave profiles) are necessary to determine accuracy of the calculations. This section presents the equation of state analysis, and the following two sections cover wave propagation and spall fracture.

## SHOCK WAVE EQUATION OF STATE

The Hugoniot equation of state is the locus of equilibrium states reached after shocking of a material, and data are usually obtained either as stress-particle velocity points or as shock velocity-particle velocity points. The shock wave Hugoniot data presented in this report were obtained with x-cut quartz gages and optical techniques. Representative quartz gage records for direct impact and transmitted wave tests are shown in Figure 10. The buffered direct impact method (tungsten carbide buffer plate on front of the quartz) permitted stresses up to 90 kbar in titanium while keeping the stress in quartz at an acceptable level. The use of quartz gages for transmitted wave tests was primarily for the study of compressive wave development and elastic precursor decay, and results are discussed in the Wave Propagation section.

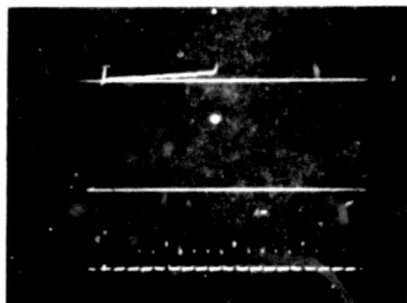


**DIRECT IMPACT**

Ti → Q

$V_I = 0.155 \text{ mm}/\mu\text{s}$

$\sigma_H = 15.2 \text{ kbar}$



**DIRECT IMPACT, BUFFERED**

Ti → WC/Q

$V_I = 0.317 \text{ mm}/\mu\text{s}$

$\sigma_H = 63.2 \text{ kbar}$

Reproduced from  
best available copy.



**TRANSMITTED WAVE**

Ti → Ti/Q

$V_I = 0.304 \text{ mm}/\mu\text{s}$

$\sigma_H = 37.9 \text{ kbar}$

Figure 10 Quartz Gage Records, Titanium



## MSL-70-23, Vol. IV

The direct impact records, which gave stress-particle velocity points since the hugoniot of quartz is known, showed a rise-time of less than 10 nsec. The slight rounding at the front of the direct impact records in Figure 10 is due to impact tilt, and the ramped peak stress region results from finite-strain effects in the quartz which are corrected in the data analysis.<sup>(38)</sup>

Hugoniot data at 160 and 185 kbar were obtained by using a streak camera and a target in the form of a two-step cylinder ("hat" configuration). A schematic of the technique and a sample record are shown in Figure 11. The two surfaces of the target are viewed through the camera slit and shock arrival is observed as a change in surface reflectance. The average shock velocity is obtained from the record, and particle velocity is assumed to be  $1/2 V_I$  (impact velocity) since impactor and target are the same material.

The hugoniot may be expressed in several forms. A convenient form for experimental work is that established by a least-squares fit to the data in the stress-particle velocity ( $\sigma_H - u_p$ ) plane. Transformation of the hugoniot into various planes, such as shock velocity-particle velocity ( $U_S - u_p$ ) and stress-volume ( $\sigma_H - v$ ), is performed by assuming a material model. This was done by assuming an ideal elastic-plastic wave structure with equilibrium initial and final states and applying the mass and momentum conservation equations:

$$\sigma_H = \sigma_e + \rho_e (U_S - u_e) (u_p - u_e) \quad (9)$$

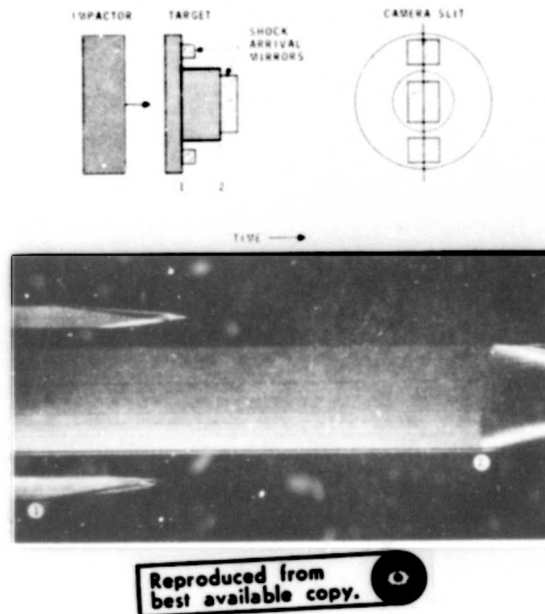


Figure 11 Streak Camera Record, "Hat" Target

and

$$v = v_0 \left( 1 - \frac{u_e}{C_L} \right) \left( \frac{U_S - u_p}{U_S - u_e} \right)$$

where  $\rho_e$  and  $u_e$  are density and particle velocity at the elastic limit  $\sigma_e$ .

Therefore, when either  $\sigma_H - u_p$  or  $U_S - u_p$  relations are established and  $\sigma_e$ ,  $\rho_e$ ,  $u_e$  and  $C_L$  are known,  $\sigma_H$ ,  $U_S$ ,  $u_p$  and  $v$  are uniquely determined. The resulting huginots for titanium at 20°C are given in Figures 12, 13 and 14. A phase change is indicated at  $\sim 100$  kbars. This phase change is apparently from

## MSL-70-23, Vol. IV

the  $\alpha$  or hexagonal-close-packed phase to the  $\omega$  or distorted body-centered-cubic phase, and has been reported under hydrostatic pressure<sup>(39-41)</sup> and shock wave<sup>(28,42-44)</sup> conditions. However, there is considerable variation in the reported stress or pressure level at which this transformation takes place, ranging from 50 to 175 kbar for shock waves, and 80 to 130 kbar for hydrostatic pressure. The quartz gage results reported here are consistent up to 90 kbars in that there is no evidence of a shift in the  $\sigma_H - u_p$  curve. Also, slanted resistance wire (free surface) and manganin gage (in-material) tests at  $\sigma_H < 90$  kbar showed no clear indication of a three-wave structure that might result from a phase change. The General Motors data referred to by Seaman, et al.,<sup>(28)</sup> in support of a phase change at  $\sim 50$  kbar is now believed to be the result of interaction of the reflected elastic wave with the plastic wave front. The streak camera data at 160 and 185 kbar gave  $U_S - u_p$  points much lower than would be expected on the basis of the low pressure data, thus supporting existence of a phase change below 160 kbar.

One test specimen was shocked to  $\sim 125$  kbar, recovered and then examined with an X-ray diffractometer in an attempt to identify the  $\omega$  phase. Recorded diffraction patterns (partial) are shown in Figure 15.\* There is no evidence of change in crystal structure as a result of shocking, although there is significant line broadening due to residual strain and twins in the recovered specimen. Although hydrostatic pressure tests indicate the  $\omega$  phase would be retained upon release of pressure, the relatively short times ( $\sim 1$   $\mu$ sec) and the slight temperature rise ( $\sim 10^\circ\text{C}$ ) associated with shock wave loading, as well as the complicated unloading path and possible recovery damage,

---

\* Line identification was based on American Society for Testing and Materials STP-48, Chemical Analysis Data Cards.

may have prevented retention of a sufficient amount of  $\alpha$  phase to be identified. X-ray diffraction tests by Seaman, et al.,<sup>(28)</sup> on a specimen shocked to 56 kbar also failed to show evidence of a new phase.

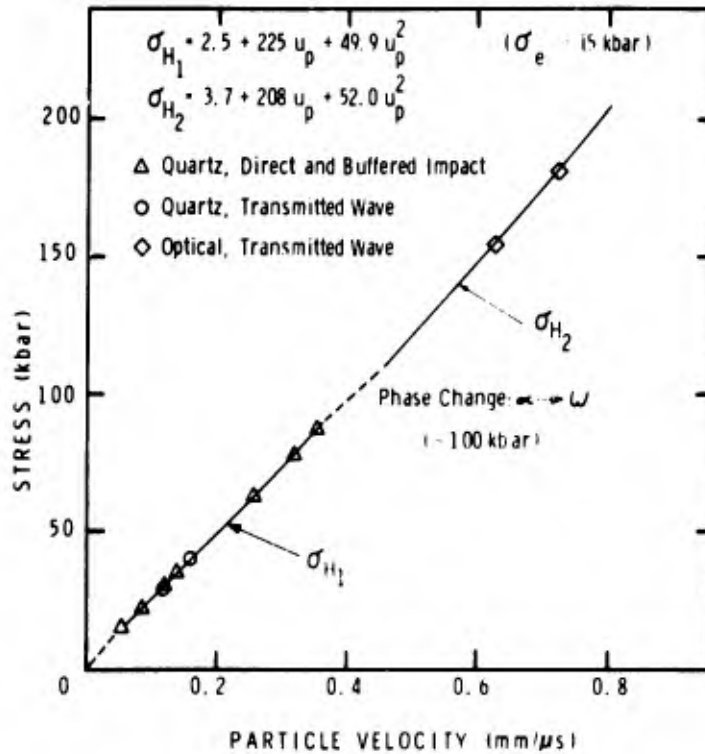


Figure 12 Stress-Particle Velocity Hugoniot, Titanium

The low pressure ( $\sigma_H < 90 \text{ kbar}$ ) equations of state for titanium are:

$$\left. \begin{aligned}
 \sigma_{H_1} &= 2.5 + 225 u_p + 49.9 u_p^2 \quad (\text{Std. Error} = 0.3 \text{ kbar}) \\
 \sigma_{H_1} &= 4.5 + 1130 u_p + 1410 u_p^2 \\
 P_{H_1} &= 1130 u_p + 1410 u_p^2 \quad (\text{Hydrostat}) \\
 U_{S_1} &= 5.02 + 1.245 u_p
 \end{aligned} \right\} (11)$$

MSL-70-23, Vol. IV

The previous equations are based on the measurements indicated in Figure 12 and on  $\sigma_e = 15$  kbar. Accuracy of the data points are estimated to be  $\pm 2\%$  for  $\sigma_H$  and  $\pm 1\%$  for  $u_p$ . Hugoniot points reported by Seaman, et al.,<sup>(28)</sup> at 56.5, 62.2 and 211 kbar are within  $\sim 2\%$  of the fits to the data given in Figure 12.

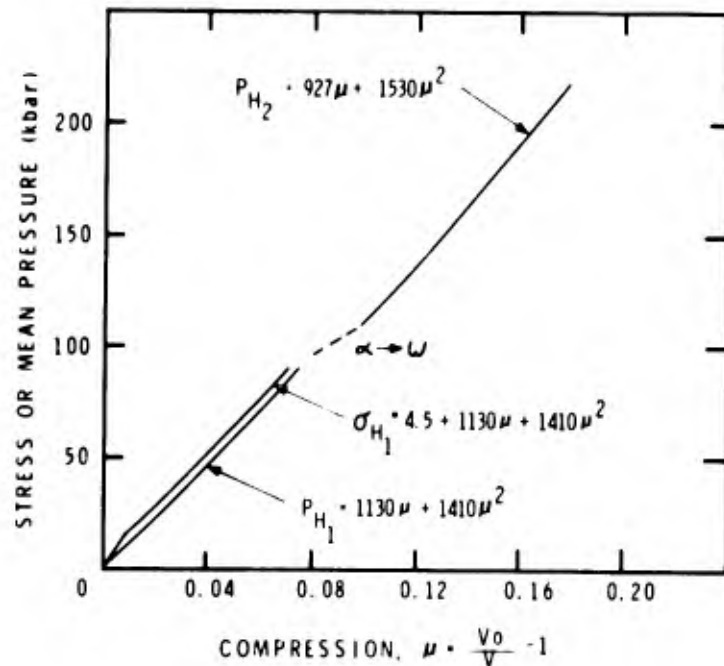


Figure 13 Stress or Mean Pressure-Compression Hugoniot, Titanium

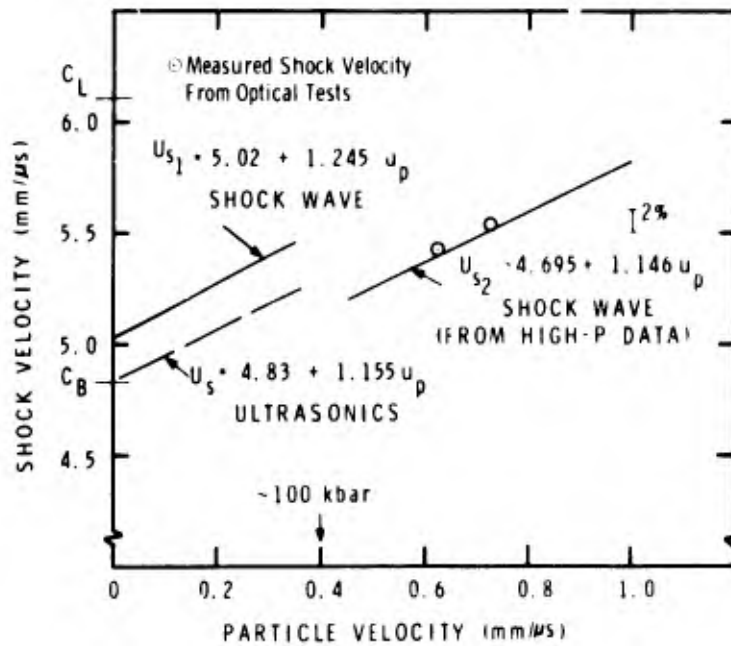


Figure 14 Shock Velocity-Particle Velocity Hugoniot, Titanium

The high pressure ( $\sigma_H > 150$  kbar) equations of state given in Figures 12 to 14 are based on the  $U_S - u_p$  fit reported by Isbell, et al.,<sup>(45)</sup> and conversion to the  $\sigma_H - u_p$  and  $P_{H_2} - u_p$  planes was based on  $\sigma_e = 15$  kbar:

$$\left. \begin{aligned}
 \sigma_{H_2} &= 3.7 + 208 u_p + 52.0 u_p^2 \\
 \sigma_{H_2} &= 6.8 + 927u + 1530u^2 \\
 P_{H_2} &= 927u + 1530u^2 \\
 U_{S_2} &= 4.695 + 1.146 u_p
 \end{aligned} \right\} \quad (12)$$

In Equations 11 and 12 the hydrostat ( $P_{H_2} - u$ ) was obtained by subtracting the stress-axis intercept value from the  $\sigma_H - u$ .

MSL-70-23, Vol. IV

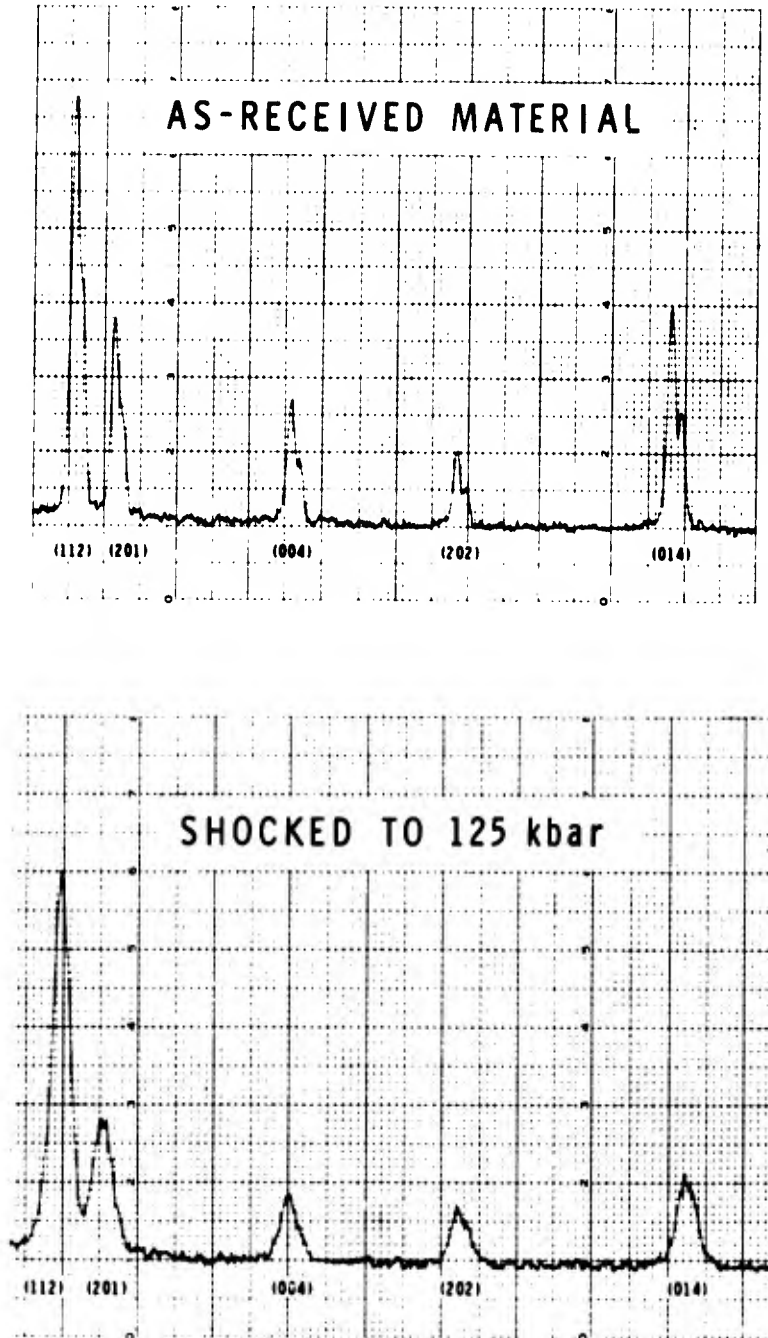


Figure 15 X-ray Diffraction Patterns, Titanium  
(CuK $\alpha$  Radiation, Ni Filter)

equation. This approach satisfies the requirement that the  $P_H - \mu$  function pass through the origin and assumes the deviatoric stress ( $\sigma_D$ ) is constant (no strain hardening). Alternative ways of estimating  $\sigma_D$  for the low-pressure region are discussed in Appendix D.

For comparison, the  $U_S - u_p$  fits reported by McQueen, et al.,<sup>(44)</sup> were  $U_S = 5.22 + 0.767 u_p$  for low pressure and  $U_S = 4.81 + 1.10 u_p$  for high pressures. These are significantly different than given in this report, and these differences may be due to the influence of structural or crystallographic anisotropy in the material (i.e., material variability), as well as to effects of different experimental and data analysis techniques.

#### ULTRASONIC EQUATIONS OF STATE

The equation of state can also be determined from ultrasonics measurements. Accurate measurement of elastic wave velocities (and, therefore, bulk modulus) as a function of hydrostatic pressure makes it possible to directly estimate shock wave compression behavior. Numerous analytical and empirical relations have been developed for relating pressure, volume and bulk modulus, including those of Birch<sup>(46,47)</sup>, Murnaghan<sup>(48)</sup> and Keane<sup>(49,50)</sup>. The use of these relations is discussed in Appendix E and results are summarized below:

##### Birch EOS

$$P_T = 1565 \left[ (1+\mu)^{7/3} - (1+\mu)^{5/3} \right] \left[ 1 - 0.180 \left\{ (1+\mu)^{2/3} - 1 \right\} \right] \quad (13)$$



MSL-70-23, Vol. IV

Murnaghan EOS, Isotherm

$$P_T = 277.4 \left[ (1+\mu)^{3.76} - 1 \right] \quad (14)$$

Murnaghan EOS, Adiabatic

$$P_S = 290.6 \left[ (1+\mu)^{3.62} - 1 \right] \quad (15)$$

Keane EOS,  $K_\infty^{S'} = 0.95$

$$P_S = 4220 \left[ (1+\mu)^{0.95} - 1 \right] - 2931 \ln (1+\mu) \quad (16)$$

In the above equations, subscripts T and S indicate isothermal and isentropic values, respectively.

Duvall gives a method of calculating the increase in entropy across a shock which can be applied to the Murnaghan equation to give: (51,52)

$$P_H = P_S + \frac{\gamma_0 K_0^S}{12} \left( K_{0S}^{S'} + 1 \right) \left( \frac{\mu}{1+\mu} \right)^3$$

$$P_H = P_S + 450 \left( \frac{\mu}{1+\mu} \right)^3 \quad (17)$$

Zel'dovich gives an expression relating  $P_S$  and  $P_T$ , assuming  $\gamma/v$  is constant: (52,53)

$$P_S = P_T + 3T_0 K_0^T \left[ \exp \left\{ \gamma_0 \left( \frac{\mu}{1+\mu} \right) \right\} - (1+\mu) \right]$$

$$P_S = P_T + 7.74 \left[ \exp \left\{ 1.11 \left( \frac{\mu}{1+\mu} \right) \right\} - (1+\mu) \right] \quad (18)$$

The above equations of state are compared to the shock wave EOS in Table IV. The entropy correction based on the Murnaghan equation has been applied to the Birch and Keane equations as well. The ultrasonic equations of state show good agreement with each other but are 5 to 7% below the shock wave hydrostat.

TABLE IV

EQUATIONS OF STATE COMPARISON-HYDROSTAT, ALPHA TITANIUM

$\mu = \frac{v_0}{v} - 1$	$P_H$ , HUGONIOT MEAN PRESSURE (kbar)				
	BIRCH EQ. 13	MURNAGHAN		KEANE EQ. 16	SHOCK WAVE EQ. 11
		EQ. 14	EQ. 15		
0.015	16.0	16.0	16.1	16.5	17.3
0.030	32.6	32.6	32.8	33.5	35.2
0.045	49.9	49.9	50.2	51.2	53.7
0.060	67.8	68.0	68.3	69.4	72.9
0.075	86.4	86.8	87.1	88.2	92.7

The shock velocity-particle velocity relationship can also be determined from ultrasonic data. Following the method of Ruoff<sup>(54)</sup> one obtains:

$$U_S = C_B + S u_p + A u_p^2 \quad (19)$$

MSL-70-23, Vol. IV

$$\left. \begin{aligned}
 \text{where } C_B &= \left( \frac{K_0^S}{10\rho_0} \right)^{1/2} \\
 S &= 1/4 \left( K_{OS}^{S'} + 1 \right) \\
 A &= \frac{1}{24 C_B} \left[ S \left( 7 - K_{OS}^{S'} + 4\gamma_0 \right) + 2K_0^S K_{OS}^{S''} \right]
 \end{aligned} \right\} (20)$$

For titanium:

$$U_S = 4.83 + 1.155 u_p + 0.078 u_p^2$$

The  $u_p^2$  coefficient ( $A = 0.078$ ) was calculated assuming  $K_{OS}^{S''} = 0$ . If one assumed  $A = 0$ , then  $K_{OS}^{S''} = -0.0043$ . Since the uncertainty in  $K_{OS}^{S''}$  is on the order of  $\pm 0.01$ , the  $A$  coefficient will be taken as zero, which gives:

$$U_S = 4.83 + 1.155 u_p \tag{21}$$

This is compared with the linear  $U_S - u_p$  relation obtained from low-pressure shock wave data in Figure 14.

The hydrostatic compressibility of titanium was determined by Bridgman and reported by Gschneidner<sup>(55)</sup> as:

$$-\frac{\Delta v}{v_0} = \frac{\mu}{1+\mu} = 0.9328 \times 10^{-3} P_T - 2.358 \times 10^{-6} P_T^2 \tag{22}$$

Comparing this with the shock wave and ultrasonic results presented in this report gives:

$P_T$ , ISOTHERMAL PRESSURE (kbar)

<u><math>\mu</math></u>	<u>Shock Wave Eq. 11*</u>	<u>Ultrasonics Eq. 14</u>	<u>Hydrostatic Eq. 22</u>
0.01	11.4	10.6	10.9
0.02	23.2	21.4	22.3
0.03	35.2	32.6	34.2

\* Corrected for isothermal conditions.

The hydrostatic data indicates a compressibility midway between that obtained from shock wave and from ultrasonics data, for pressures up to 35 kbars.

YIELD BEHAVIOR

A complete description of the low-pressure equation of state requires consideration of yield behavior or the hugoniot elastic limit. Values of compressive yield were obtained by three independent methods.

A. Uniaxial Stress

The yield level was determined in uniaxial stress ( $\sigma_\sigma$ ) as a function of strain rate and then converted to uniaxial strain using:

$$\sigma_e = \sigma_\sigma \left( \frac{1-\nu}{1-2\nu} \right) \tag{23}$$

<u>Strain Rate (<math>\text{sec}^{-1}</math>)</u>	<u><math>\sigma_e</math> 12.7mm Stock (kbar)</u>
$10^3$	15.4
$10^{-3}$	9.1

MSL-70-23, Vol. IV

B. Wave Profiles

The elastic precursor level was measured as a function of propagation distance using quartz gages. These profiles are discussed in the section on Wave Propagation.

Propagation Distance (mm)	$\sigma_e$ 12.7mm Stock (kbar)
2	16.5
10	14.0

C. Hugoniot

The yield level in uniaxial strain was inferred by comparison of the elastic ( $\rho_0 C_L$ ) and plastic ( $\sigma_H$  vs.  $u_p$ ) hugoniot, i.e., by defining the elastic limit as the intersection of the elastic response line and the curve-fit to the stress-particle velocity data

$$10 \rho_0 C_L u_e = A + B u_e + C u_e^2$$

Solving for  $u_e$  gives

$$u_e = 0.054 \text{ mm}/\mu\text{sec}$$

$$\therefore \sigma_e = 14.9 \text{ kbar}$$

For an isotropic, polycrystalline metal with elastic-perfectly plastic behavior and no strain-rate or time-dependent effects,

one would expect the same yield to be obtained by each method. Alpha titanium exhibits both strain-rate sensitivity and elastic precursor decay, with resulting variations in the Hugoniot elastic limit. These variations are not excessive, however, and a yield level can be assumed which is in fair agreement with that determined by the three methods. For this particular titanium, the equilibrium yield in uniaxial strain was taken as 15 kbar, and this value was used in the EOS transformations made in obtaining Equations 11 and 12.

#### METALLOGRAPHIC STUDIES

Twinning as a deformation mode in alpha titanium has been well established, under various loading conditions and at low (quasi-static testing) and high (shock wave loading) strain rates (see, e.g., Refs. 11,12,17,25,56,57). The structure of titanium after shock loading at stresses up to 125 kbar is shown in Figures 16 to 18. The compressive pulse duration for these specimens was  $\sim 2$   $\mu$ sec and the shock wave propagation direction in the pictures was vertical. The specimens were not backed by momentum traps and so were subjected to tensile stresses during unloading, however, the photomicrographs were taken of regions free of any visible cracks. There were almost no twins visible in the as-received material (12.7 mm plate), but twin density increased significantly with increasing peak stress. Macrohardness increased slightly with peak stress.

Dislocation densities in 0.048 mm foil specimens of alpha titanium in the as-received condition and after shock loading to 39 kbar were estimated by transmission electron microscopy.

MSL-70-23, Vol. IV

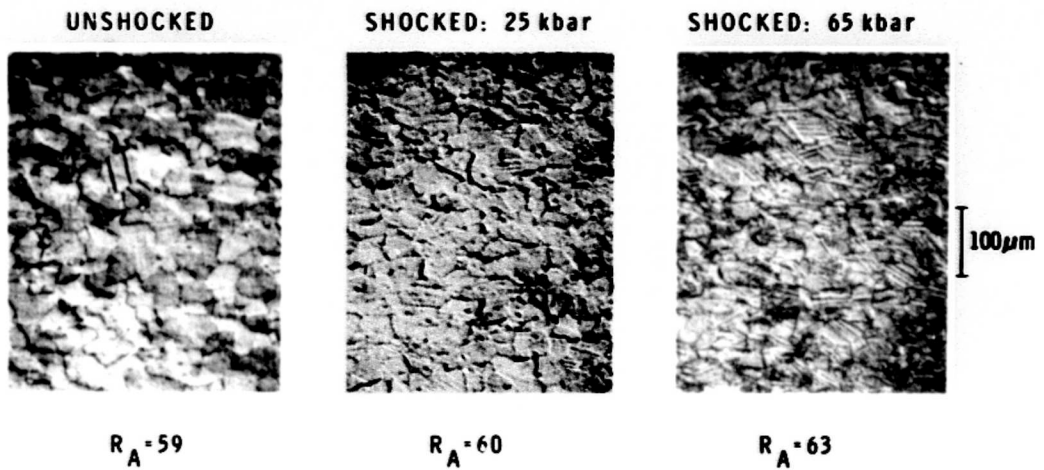


Figure 16      Titanium Microstructure, As-Received and Shocked (12.7 mm Plate)

Reproduced from  
best available copy. 

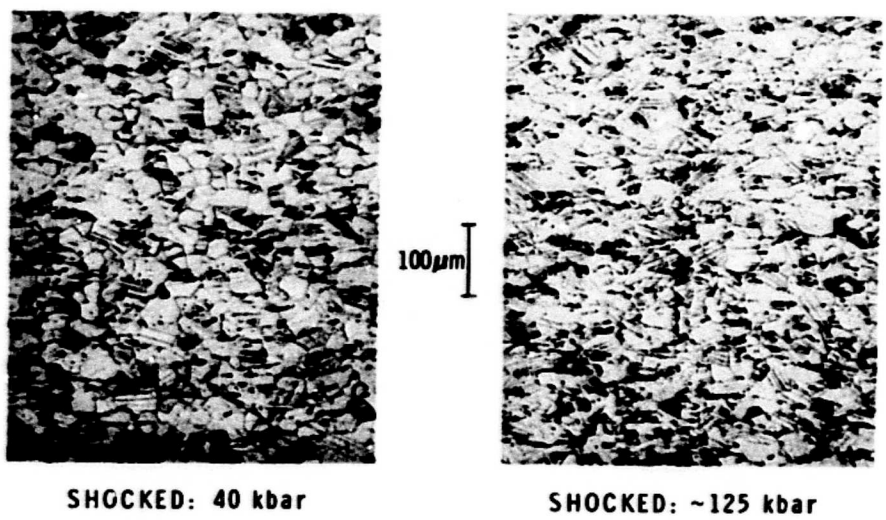


Figure 17      Titanium Microstructure, Shocked (12.7 mm Plate)

Reproduced from  
best available copy.

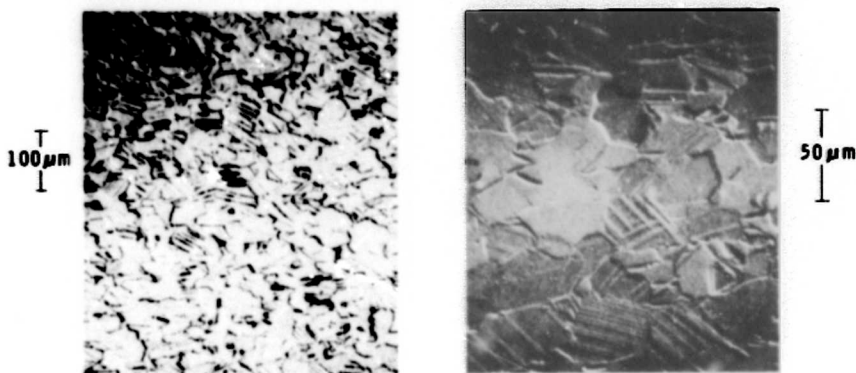


Figure 18 Titanium Microstructure, Shocked to 40 kbar (12.7 mm Plate)

Specimens were prepared by electropolishing the 0.048 mm foils in a solution of 60 ml 70% perchloric acid, 590 ml methanol, and 350 ml butyl cellosolve. The solution was cooled to approximately 5°C and a voltage of 12 volts was applied. The microscope used was an A.E.I. Model EM6G at an accelerating voltage of 100 kv. A tilting stage was used to obtain the necessary contrast conditions. The as-received material is shown in Figure 19 and had a fine equiaxed grain structure with a grain size on the order of 5 μm diameter. The dislocation density was low, and in some regions no dislocations were visible at all. The overall density was estimated by counting the number of intersections with the surface of the foil to be  $\sim 10^7$  dislocations/cm<sup>2</sup>. The shock loaded material, shown in Figure 20, also had equiaxed grains but with a high dislocation density. Twins were observed in many grains. The dislocation density was estimated to be  $\sim 2 \times 10^9$  dislocations/cm<sup>2</sup>.



MSL-70-23, Vol. IV



Figure 19 As-Received Titanium Foil, Transmission Electron Micrographs

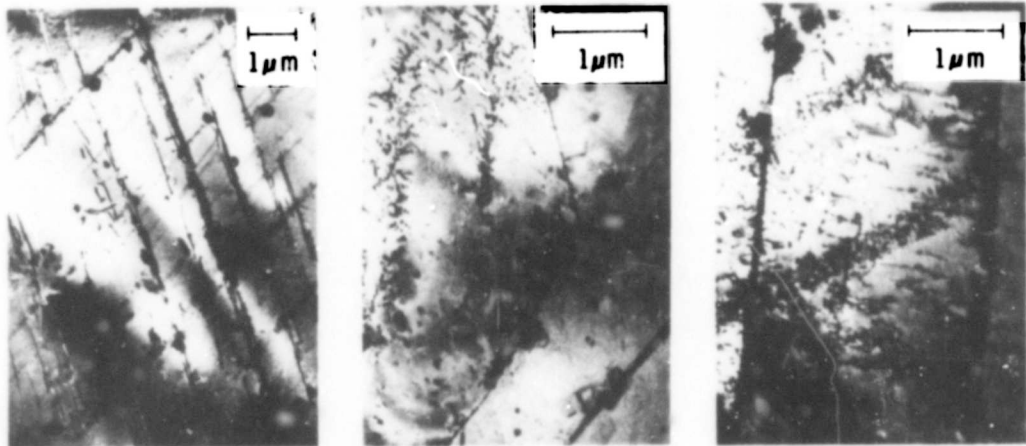


Figure 20 Shocked (39 kbar) Titanium Foil, Transmission Electron Micrographs

Both estimates presented above are probably low due to the following effects:

1. Migration of dislocations to the surface of the foil during electropolishing.
2. Only a fraction of the dislocations present is visible under a particular diffraction condition.<sup>(58)</sup>
3. Variations of dislocation density from region to region and relatively small total area viewed.
4. Difficulty in counting the number of intersections in regions of high density.

Effect (1) is expected to be small in titanium. Effect (2) can be estimated to render approximately 25% of the dislocations invisible. No quantitative estimate of effects (3) and (4) can be made. In view of these limitations, it is considered that the densities quoted above can be regarded as order of magnitude estimates only.

MSL-70-23, Vol. IV

## SECTION V

## WAVE PROPAGATION

Compressive wave development and elastic precursor decay are used as basic input data for material response models, while a complete understanding of shock wave propagation requires inclusion of release wave behavior. Profiles of shock waves propagated through a specimen were recorded as stress-time or velocity-time histories. The stress-time data were obtained with quartz gages and the results were transformed to material stress by application of an impedance matching technique,<sup>(38)</sup> assuming time-independent behavior. The velocity-time data were obtained with a velocity interferometer and are presented as measured. All wave profiles obtained (quartz gage and velocity interferometer) are given in Appendix F for reference.

## COMPRESSIVE WAVE BEHAVIOR

Structure in the compressive wave is shown in the quartz gage data in Figures 21 and 22.\* The wave front is characterized by an elastic portion and a transition to a spreading plastic wave. Because of the impedance difference between titanium and quartz, the elastic wave is partially reflected back into

---

\* In this and subsequent figures containing quartz gage data, tilt refers to the time required for a step-input to sweep across the gage electrode diameter.

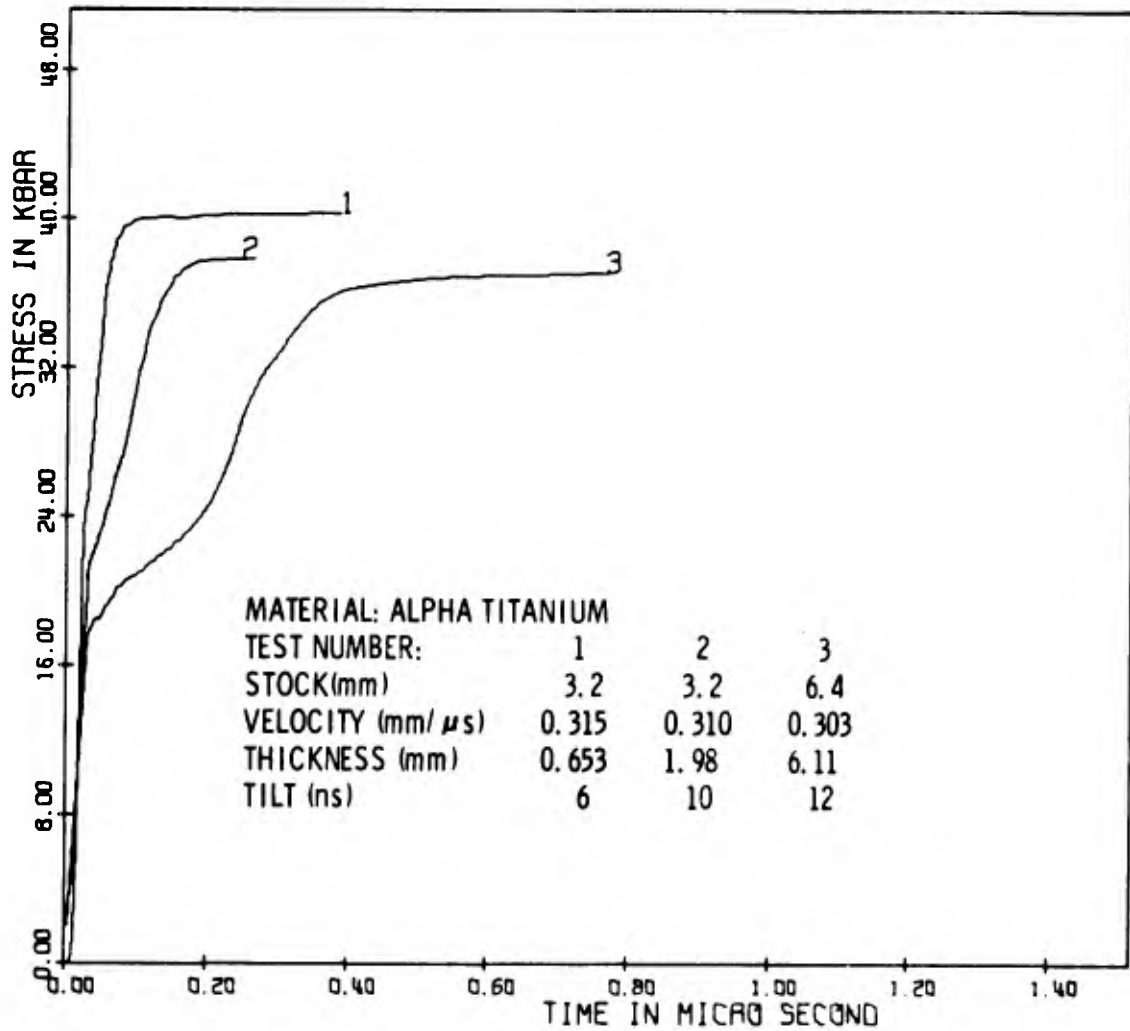


Figure 21 Compressive Waves, Propagation Distance Dependence (3.2 mm and 6.4 mm Stock)

MSL-70-23, Vol. IV

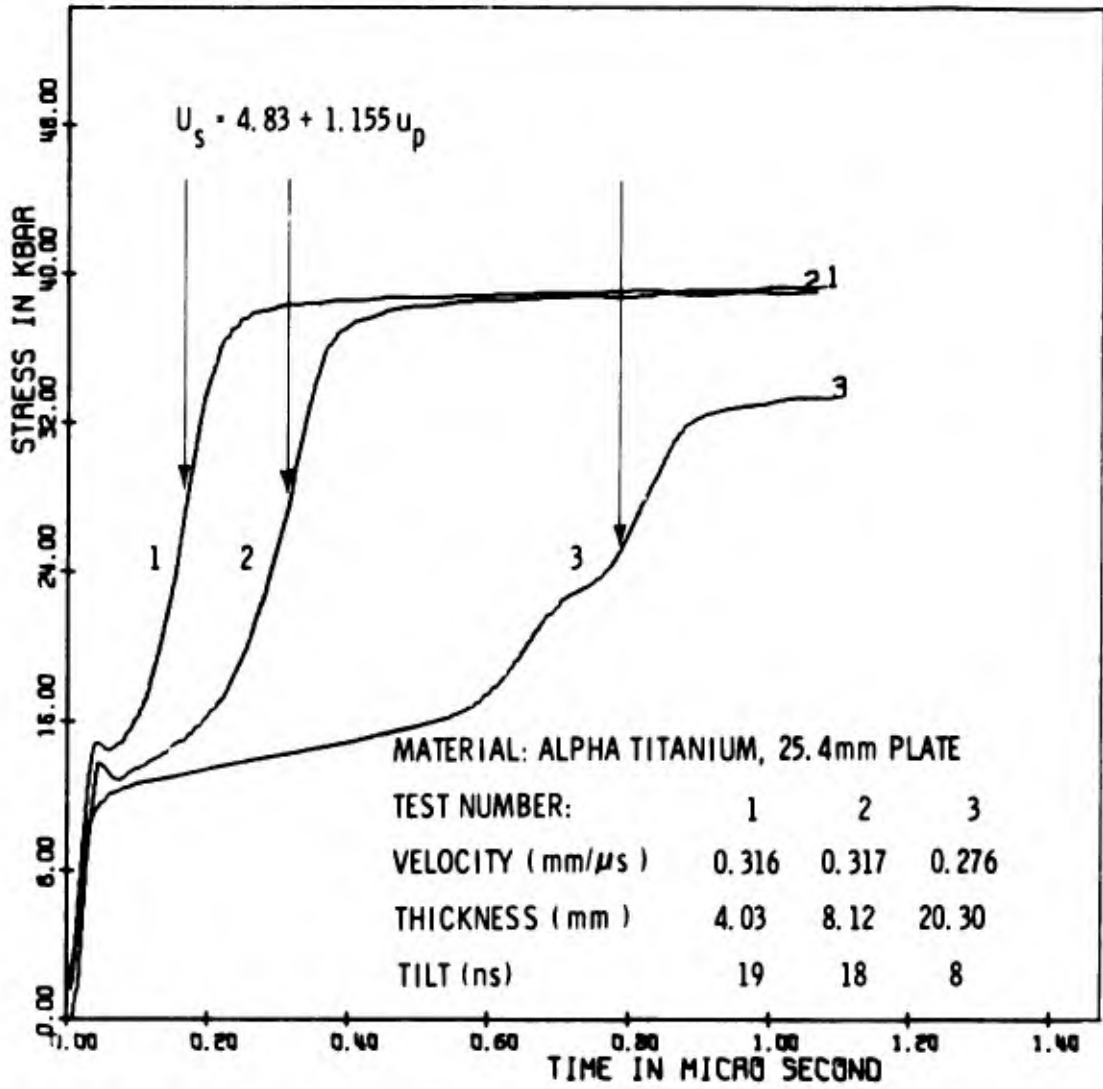


Figure 22 Compressive Waves, Propagation Distance Dependence (25.4 mm Stock)

the target. This reflected wave then interacts with the plastic wave which results in a perturbation on the plastic wave front. As thickness increases, the perturbations become more pronounced (see 20.3 mm target in Figure 22). Stress relaxation behind the precursor was evident for propagation distances of 4 and 8 mm, but only with as-received 25.4 mm stock. The other materials, in the as-received condition, did not show relaxation, at least for the test conditions studied. However, annealing of an 8 mm target from 12.7 mm stock did result in measurable relaxation as shown in Figure 23. Also, a test with an 8 mm target from 25.4 mm stock did not show relaxation when tested at only 23 kbar peak stress, as shown in Figure 24. Although metallurgical examinations were not performed, these variations in relaxation behavior may be related to differences or changes in initial dislocation density and dislocation multiplication in the elastic wave front.

The shock velocities as calculated from the shock wave Hugoniot (Equation 11) are indicated in Figure 22. Although the calculated plastic wave velocity lies within the rise-time of the measured wave, the plastic wave is not a step pulse and shows spreading with propagation distance, at least for stresses below  $\approx 40$  kbar. This means that transformation of the Hugoniot from the  $\sigma_H - u_p$  plane to  $\sigma_H - u$  or  $U_S - u_p$  by assuming ideal elastic-plastic wave structure and steady-state conditions may lead to some uncertainty at lower stresses.

Dislocation models for predicting compressive wave development utilize measurements of elastic precursor decay to evaluate various constants related to dislocation density and multiplication (see, e.g., Ref. 59). Unfortunately, it is very

MSL-70-23, Vol. IV

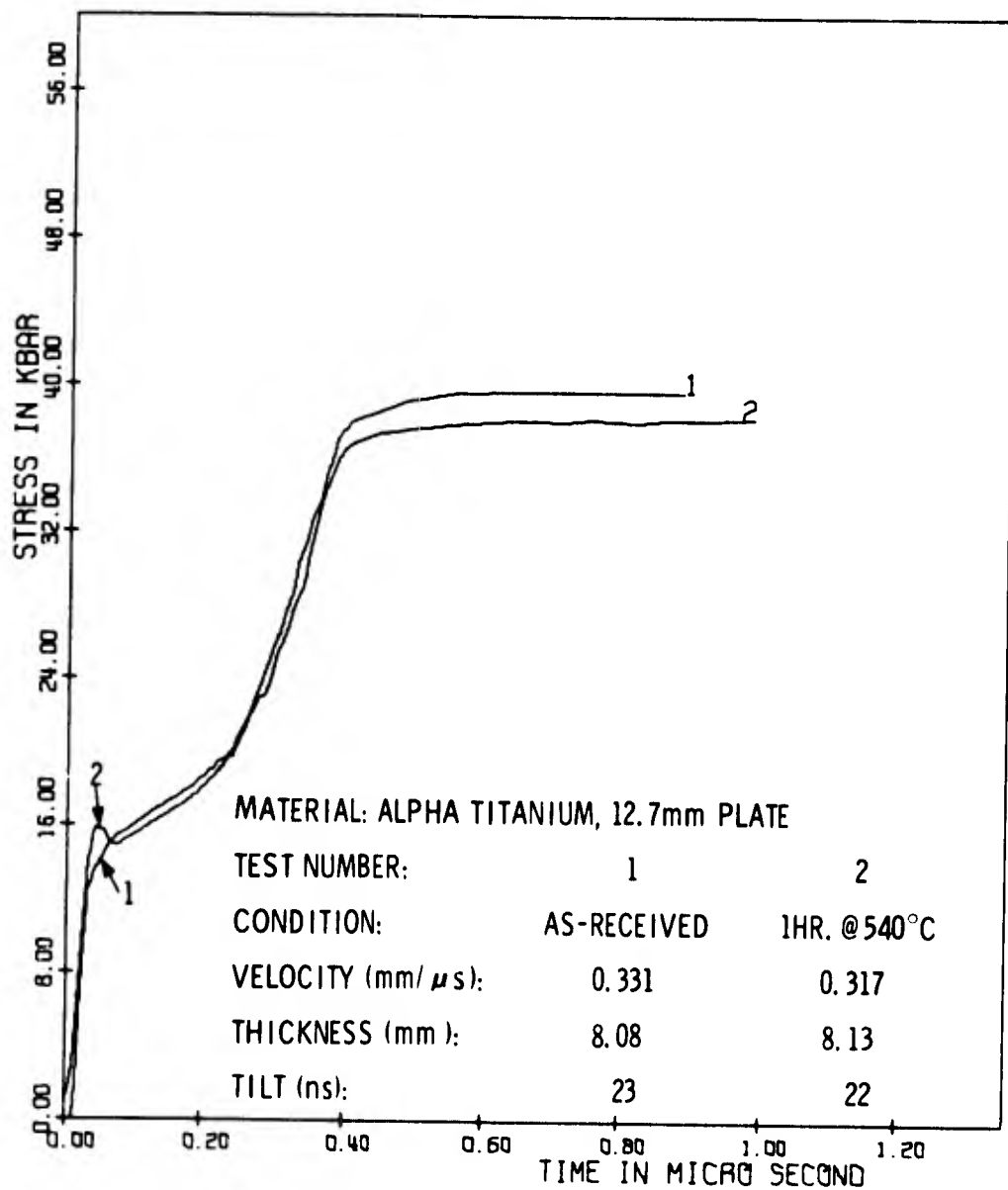


Figure 23 Compressive Waves, As-Received and Annealed Material (12.7 mm Stock)

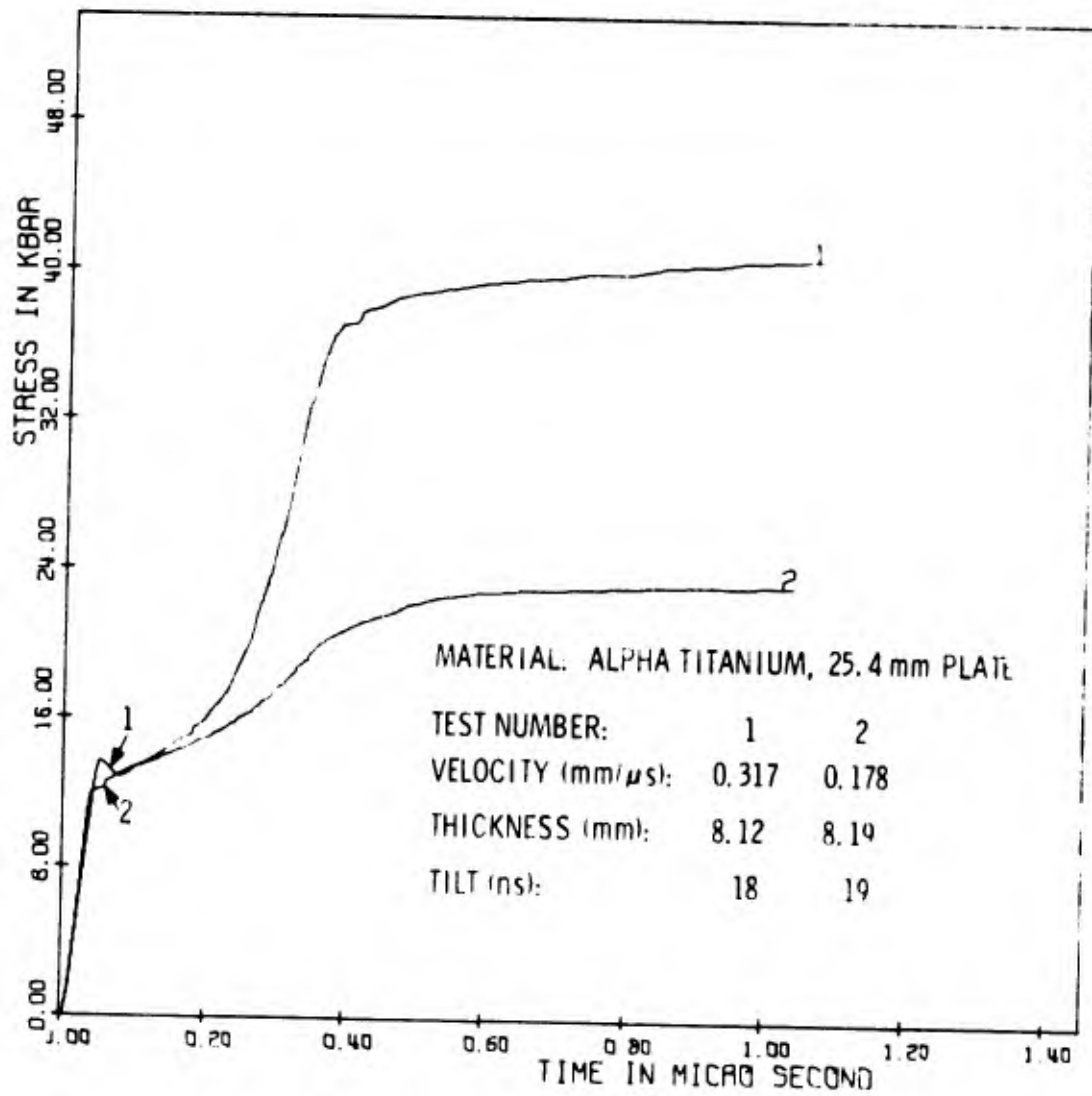


Figure 24 Compressive Waves, Peak Stress Dependence (25.4 mm Stock)



## MSL-70-23, Vol. IV

difficult to obtain accurate elastic precursor level data at propagation distances less than  $\sim 2$  mm and it is in this region (0 to 2 mm) that most of the precursor decay occurs for many metals. Also, even at larger distances there is always some uncertainty in the precursor level due to both material scatter and dispersion characteristics and to experimental errors (particularly tilt). The result is that much of the data presently available, when given realistic uncertainty bars, can be used to support a number of different models of precursor attenuation.

Precursor decay data for titanium, as determined from quartz gage data, is summarized in Figure 25. The calculated initial elastic impact stress was 43 kbar for these tests and the precursor level has dropped  $\sim 60\%$  in 2 mm of travel. Over the range of propagation distance studied, the precursor level in 3.2 and 6.4 mm stock was 3 to 4 kbar greater than in 12.7 or 25.4 mm stock. This difference is illustrated by the comparison of compressive waves for 4 mm targets from 6.4 and 25.4 mm stock given in Figure 26.

The uncertainty bars in Figure 25 reflect the dispersion and rounding at the elastic front which is due to at least three factors. First, since quartz gages average stress over the electrode area, small differences in wave front arrival times at the specimen/gage interface would give a finite rise-time rather than an instantaneous stress jump. These differences may be due to wave reflections and dispersion at grain boundaries and to slight differences in local wave velocity arising from grain anisotropy. Second, the finite thickness of the epoxy between the specimen and the gage will increase the apparent rise-time in the wave front because of impedance differences. Third, the influence of shock wave tilt on a

finite-area gage is to smooth out abrupt changes in stress level as well as to increase recording rise-time of the wave front. This becomes particularly severe at short propagation distances where separation of the elastic and plastic waves is only on the order of tens of nanoseconds.

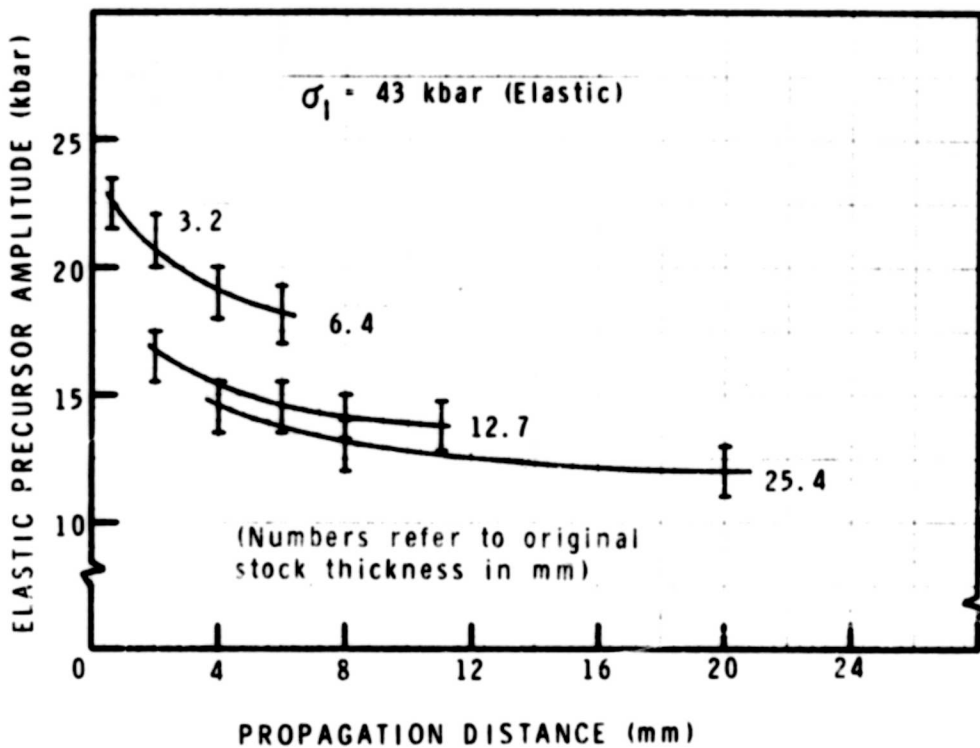


Figure 25 Elastic Precursor Decay in Titanium

MSL-70-23, Vol. IV

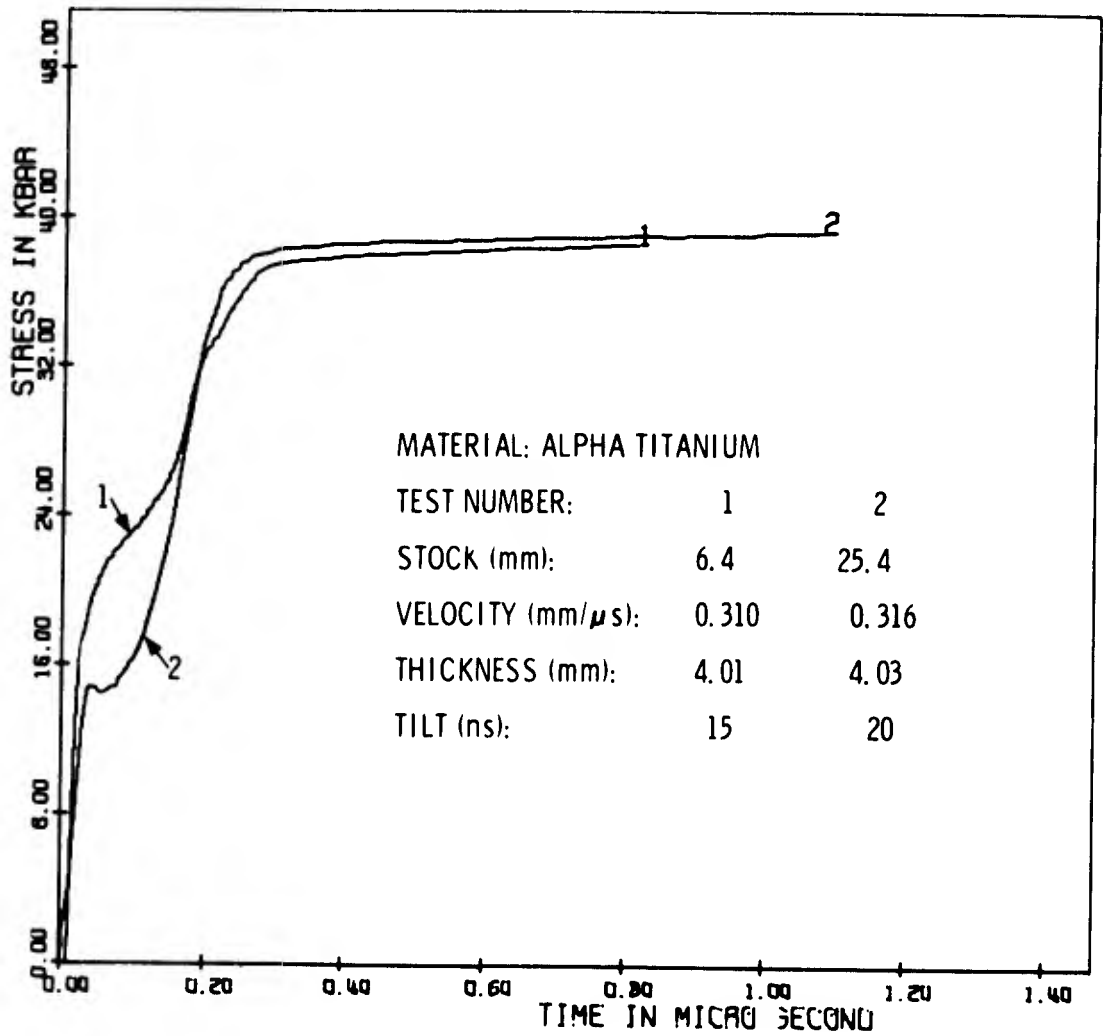


Figure 26 Compressive Waves, Material Differences

## RELEASE WAVES AND WAVE ATTENUATION

Release waves were studied by using relatively thin impactors and measuring the complete wave profile with the laser velocity interferometer. After impact, elastic and plastic waves propagate from the impact surface into both impactor and target. The waves that reach the impactor rear surface reflect as rarefaction waves, unloading the material. These unloading waves propagate across the impact surface into the target and are recorded at the target rear surface after arrival of the compressive wave.

An unattenuated wave profile is shown in Figure 27. (Additional impact data for velocity interferometer tests are given in Table V). The target had a fused quartz window on the rear face to reduce the magnitude of unloading due to reflection of the compressive wave. This prevents spall fracture in the target. The measured interface velocity is higher than particle velocity in the target since the impedance of titanium is greater than fused quartz. Structure is evident in the release wave, however, the development of this structure is influenced by the compressive wave in the impactor. This is because the elastic and plastic waves spread in the impactor such that all the unloading does not occur at the same time, i.e., the release wave does not start out as an abrupt pressure drop.

If target thickness is large enough compared to impactor thickness, the release wave will overtake the compressive wave and attenuate the peak stress. Wave attenuation is shown in Figure 28 for an initial stress of  $\sim 41$  kbar and in Figure 29 for an initial stress of  $\sim 152$  kbar. At the higher stress level, the impactors were backed by Plexiglas so the stress wave was released only  $\sim 70\%$ . The attenuation results are shown in

MSL-70-23, Vol. IV

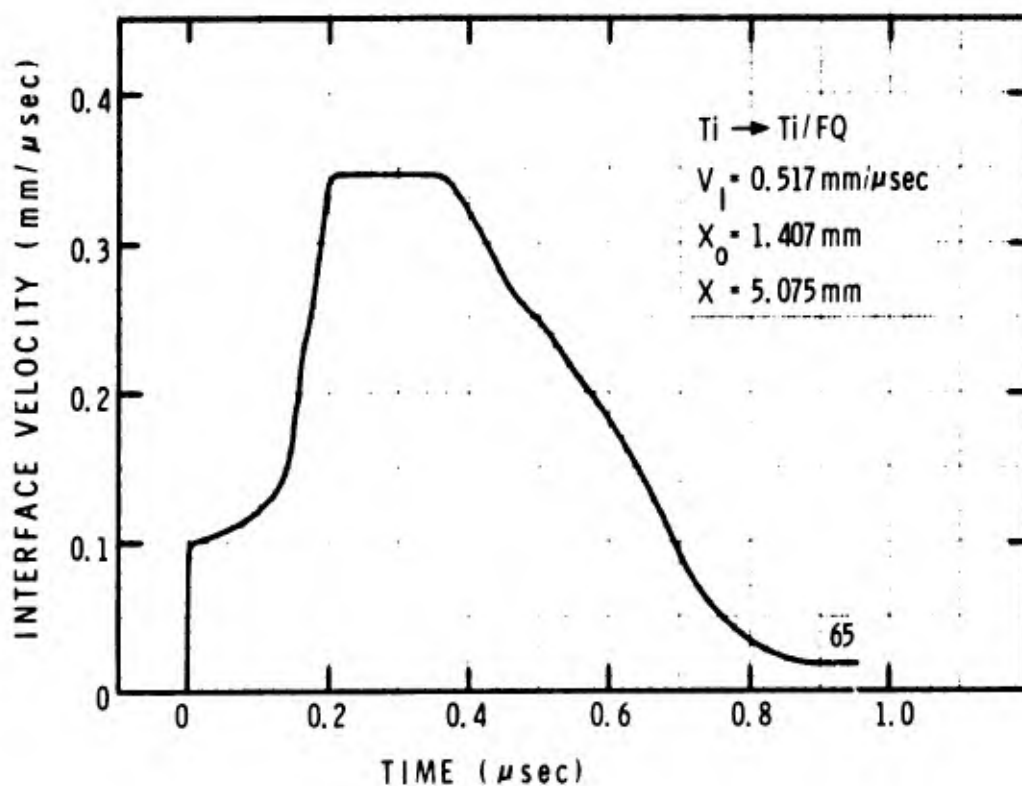


Figure 27 Complete Wave Profile, Titanium

TABLE V  
VELOCITY INTERFEROMETER TEST DATA, ALPHA TITANIUM

Test No.	$V_I$ Impact Velocity (mm/.s)	Max. Stress (kbar)	$X_0$ Impactor Thickness (mm)	X Target Thickness (mm)	X/ $X_0$	Stock (mm)	Config. <sup>1</sup>
24	0.320	40	0.883	2.014	2.28	3.2	Ti-Ti/FQ
26	0.335	42	0.944	4.041	4.28	6.4	Ti-Ti/FQ
54	0.326	41	1.110	2.022	1.82	3.2	Ti-Ti
56	0.383	47	1.107	2.007	1.81	3.2	Ti-Ti
57	0.322	40	1.138	8.108	7.13	12.7	Ti-Ti/FQ
58	0.328	41	0.950	12.164	12.80	12.7	Ti-Ti/FQ
65	0.517	64	1.407	5.075	3.61	6.4	Ti-Ti/FQ
76 <sup>2</sup>	1.232	153	0.231	2.482	10.74	3.2	Ti-Ti/FQ
77 <sup>2</sup>	1.230	152	0.226	5.085	22.49	6.4	Ti-Ti/FQ
119 <sup>2</sup>	1.214	150	0.226	0.874	3.87	3.2	Ti-Ti/FQ
176	0.380	47	0.958	8.113	8.47	12.7	Ti-Ti

1. E.g., Ti-Ti is titanium impactor into titanium target with free rear surface (FQ is fused quartz window).

2. Plexiglas-backed impactor.

MSL-70-23, Vol. IV

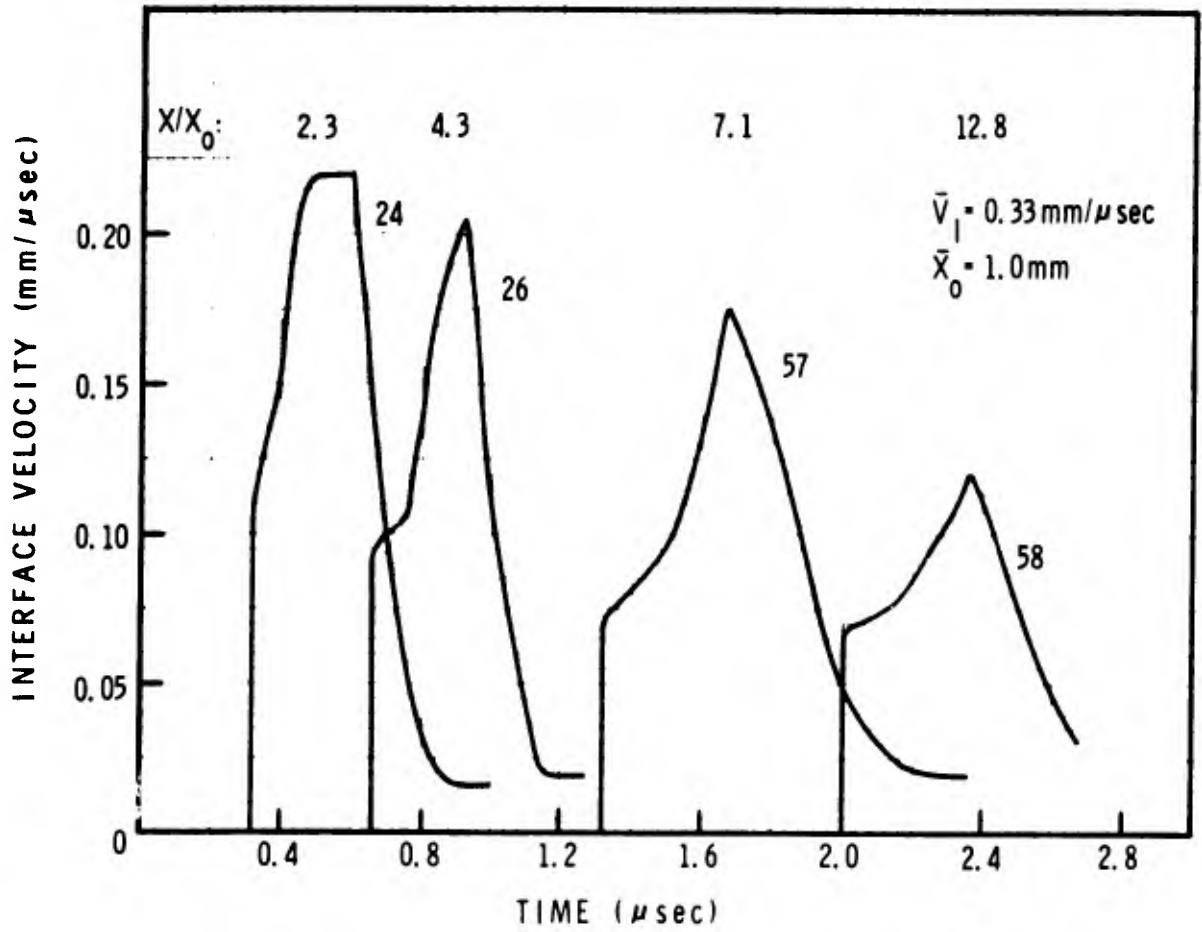


Figure 28 Wave Attenuation in Titanium, Low Pressure

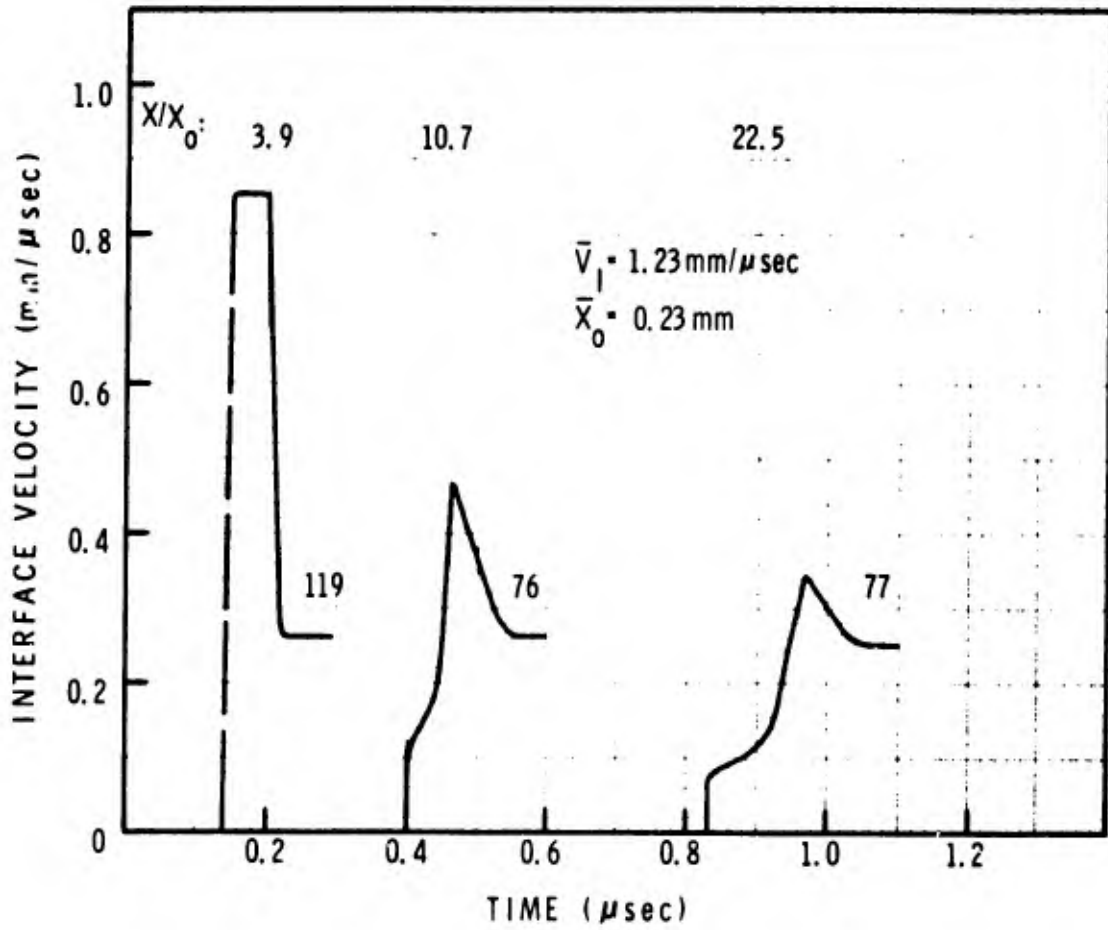


Figure 29 Wave Attenuation in Titanium, High Pressure



MSL-70-23, Vol. IV

Figure 30 in terms of decrease in peak stress vs.  $X/X_0$ . Also shown are calculated overtaking points assuming ideal elastic-plastic compression and release waves. This is given by:

$$\frac{X}{X_0} = \frac{\frac{1}{c_L} + \frac{1-u_p/U_S}{c_L - u_p}}{\frac{1}{U_S} - \frac{1-u_p/U_S}{c_L + u_p}} \quad (24)$$

where  $c_L^1$  is elastic release wave velocity ( $\approx 6.35$  mm/ $\mu$ s for 41 kbar and  $\approx 6.9$  mm/ $\mu$ s for 152 kbar<sup>(60)</sup>).

The experimental results for 152 kbar are consistent with the calculated overtaking point<sup>\*</sup>, but the results for 41 kbar show attenuation sooner than calculated. This can be attributed to the ramped plastic compressive wave at this stress. If the velocity ( $\approx 4.4$  mm/ $\mu$ s) of the trailing portion of the plastic wave at 41 kbar is used for  $U_S$  rather than the value (5.22 mm/ $\mu$ s) obtained from Equation 11, then the calculated overtaking point is  $X/X_0 = 4.0$ . This value is in better agreement with the experimental results for 41 kbar.

---

\* The calculation used the high pressure equation of state, however, the possible influence of the phase change on wave attenuation was not included.

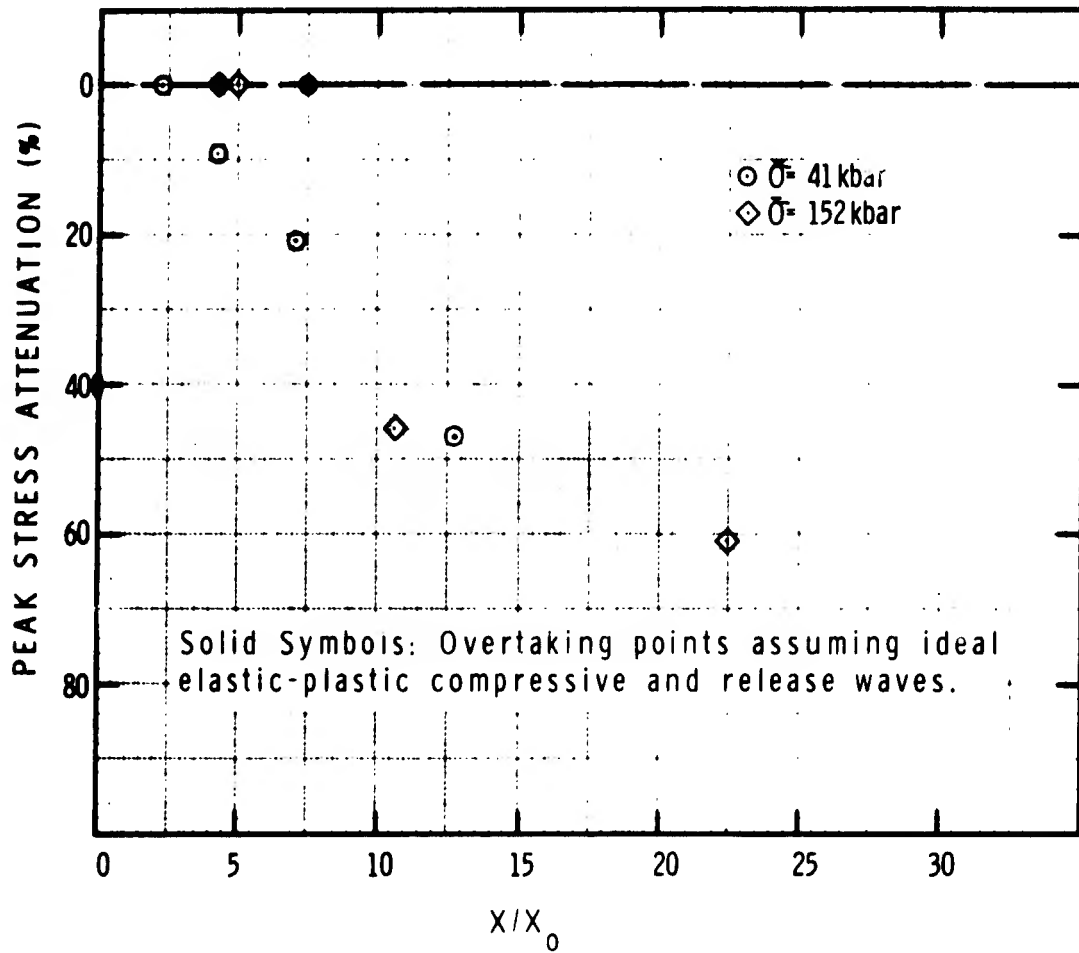


Figure 30 Peak Stress Attenuation in Titanium

MSL-70-23, Vol. IV

## SECTION VI

## SPALL FRACTURE

Spall fracture by plate impact results from reflection of compressive waves from a relatively low impedance interface (normally a free surface) and subsequent wave interaction. Spall studies were carried out with both passive and active techniques. Passive methods involve the recovery and examination of shock-loaded specimens. Metallographic examination establishes the type and degree of damage, which can be correlated with test parameters such as velocity, impactor thickness and target thickness. Active methods utilize the laser velocity interferometer and provide time-resolved data on the influence of spall fractures on shock wave profiles, as measured at the rear surface.

## RECOVERY TESTS

Spall behavior of titanium was studied by carrying out a series of impact and recovery tests, where the target was sectioned across a diameter, polished, etched, and examined optically at a magnification of 50X.\* The specimens were then graded or classified according to the degree of fracture that was observed, which ranged from no visible damage to complete material separation. The onset of significant fracture is generally referred to

---

\* Spall fracture in alpha titanium was also studied under the PREDIX program by Keller and Tuler (Ref. 61) using exploding foil techniques and by Stefansky and Shea (Ref. 62) using electron beam techniques.

as incipient spall and is a critical point since it can be used to deduce the dynamic fracture strength, and corresponds to generation of sufficient free surfaces within the material to reflect a portion of the interacting release waves as a compressive wave. The incipient spall threshold was defined as the impact velocity (for a given set of impact parameters) corresponding to cracking over at least 50% of the width of the section estimated to be under a condition of plane strain during the time of loading.

Incipient spall velocity results are summarized in Table VI. Note that the velocity for 6.4 mm stock is almost 50% higher than for 3.2 mm stock, for the same  $X_0$  and  $X$ . This is probably related to differences in structural and mechanical properties of the two materials. A few tests with 2 mm targets machined from 12.7 mm stock showed the 3.2 and 12.7 mm materials to be equivalent in spall behavior. The data for 20°C tests with 3.2 and 12.7 mm stock and unattenuated pulses are given in Figures 31 and 32. The symbols are defined as:

- Complete Separation
- ⊙ Above Incipient
- ⊗ Incipient Spall
- Below Incipient
- No Visible Damage

As is typically the case with metals<sup>(63-65)</sup>, the impact velocity for incipient spall increases for decreasing impactor thickness. This implies that peak stress (and therefore strain) required to create spall fractures increases with decreasing pulse width or time of loading. The behavior of 0.54 mm targets (Figure 31) is not consistent with an exponential-type

MSL-70-23, Vol. IV

TABLE VI  
 INCIPIENT SPALL DATA FOR ALPHA TITANIUM

$X_0$ Impactor Thickness (mm)	X Target Thickness (mm)	Stock (mm)	X/ $X_0$	T Temperature (°C)	$\Delta t_e$ Pulse Width* (.s)	$V_s$ Spall Velocity (mm/.s)
0.22	0.54	3.2	2.45	20	0.072	0.315
0.55	0.96	3.2	1.75	20	0.18	0.295
1.04	1.99	3.2	1.91	20	0.34	0.220
1.07	2.04	6.4	1.91	20	0.35	0.325
2.04	4.06	12.7	1.99	20	0.67	0.175
4.09	8.14	12.7	1.99	20	1.34	0.160
0.98	2.02	3.2	2.06	500	0.32	0.280
0.96	8.12	12.7	8.46	20	0.31	0.320

$$* \Delta t_e = \frac{2X_0}{C_L}$$

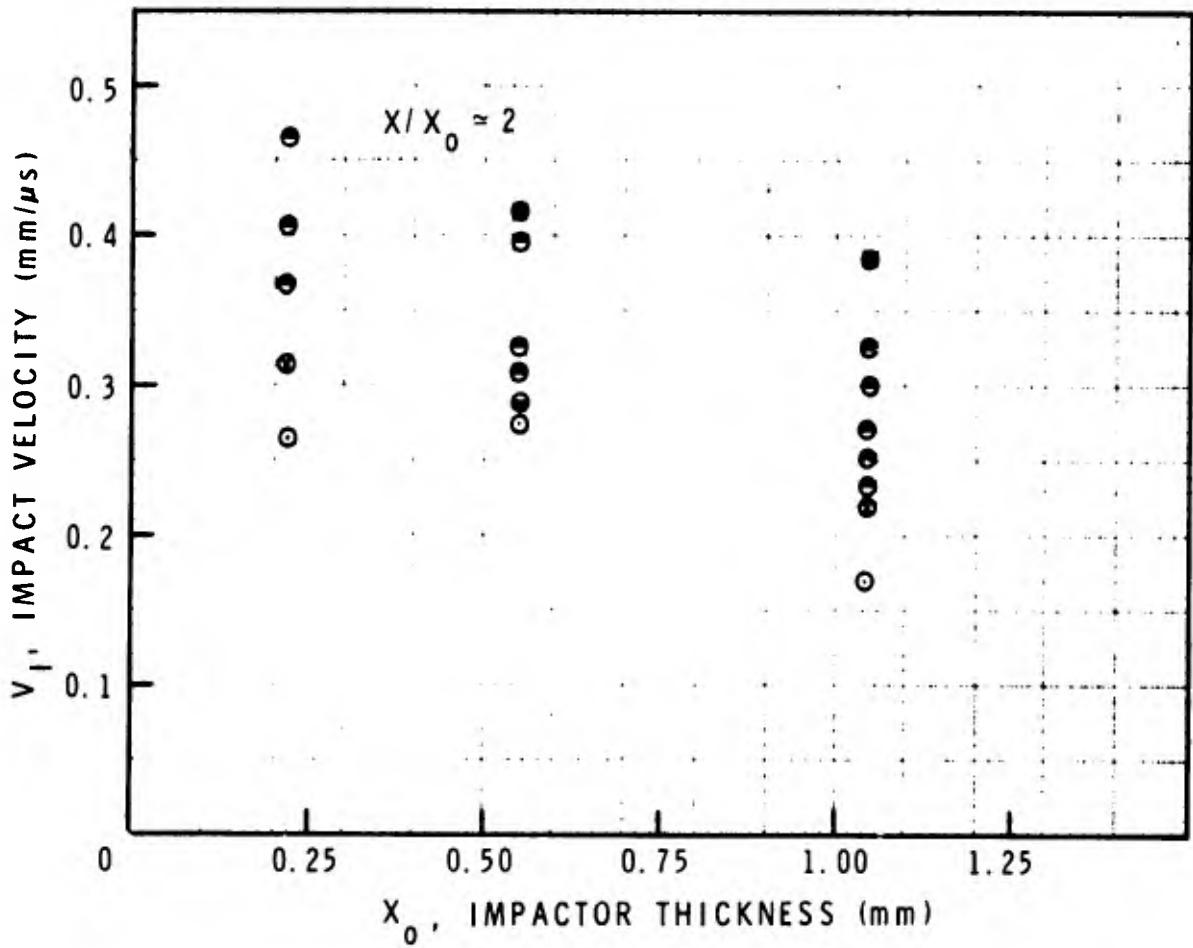


Figure 31 Spall Data for Titanium, 3.2 mm Stock (20°C)

MSL-70-23, Vol. IV

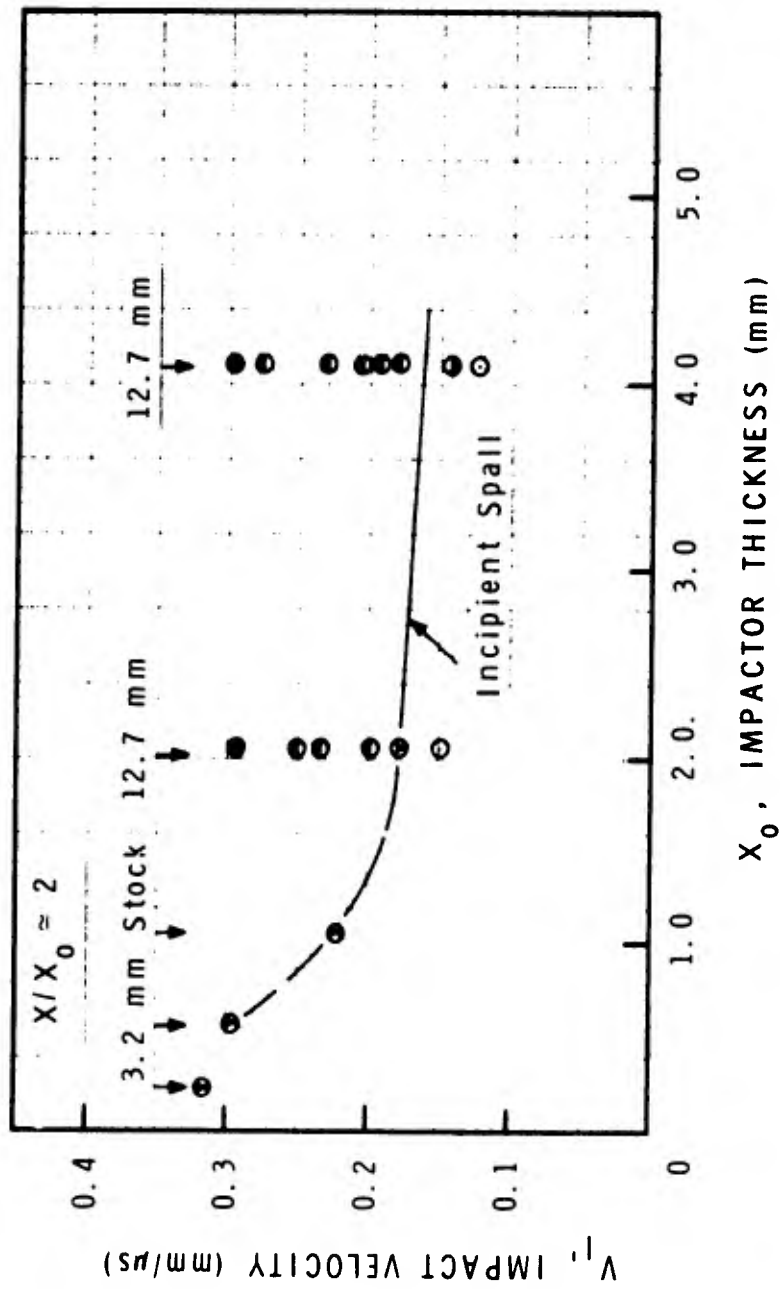


Figure 32 Spall Data for Titanium (20°C)

increase in spall velocity with decreasing impactor thickness. Although it is possible there is a limiting incipient spall velocity for very thin pulses, this anomolous behavior may be related to metallurgical effects since grain size and crack length are beginning to be significant relative to target thickness. Maiden and Green<sup>(66,67)</sup> reported the incipient spall threshold of 6Al-4V titanium (static tensile strength  $\sim 10$  kbar) for 2.5 and 5.0 mm targets. Incipient spall velocities were 0.40 and 0.35 mm/ $\mu$ sec, respectively, which are about double those for alpha titanium.

Representative photomicrographs of recovered specimens from the 20°C tests are shown in Figures 33 to 35.\* The specimens were polished and etched to provide maximum contrast between cracks and sound material. The procedure followed was:

1. Wet grind, 230/400/600 grit silicon carbide paper.
2. Preliminary polish, 6 $\mu$ m, 3 $\mu$ m and 1 $\mu$ m diamond paste.
3. Intermediate polish, <20 $\mu$ m magnesium oxide slurry.
4. Swab etch, 10 ml hydroflouric acid (HF), 10 ml nitric acid (HNO<sub>3</sub>), 30 ml lactic acid,  $\sim 1$  sec (20°C).
5. Repeat (3) for final polish.
6. Swab etch, 2 m. hydroflouric acid (HF), 4 ml nitric acid (HNO<sub>3</sub>), 94 ml water,  $\sim 3$  sec (20°C).
7. Repeat (3) and (6) as necessary.

Note that the 0.54 mm target (Figure 33) shows an almost random distribution of cracks across two-thirds of the thickness. Because of this behavior (typical for this thickness), 0.54 mm

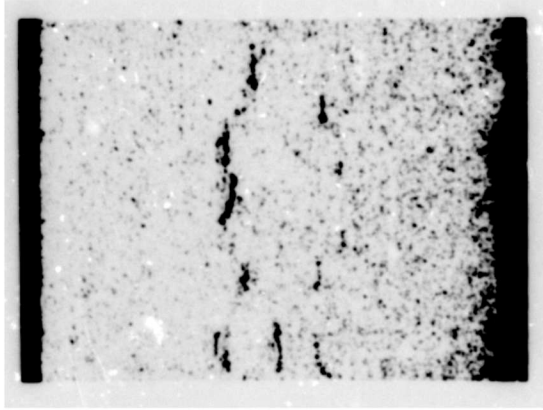
---

\* All spall photomicrographs in this report are oriented such that initial shock wave propagation was from bottom to top.



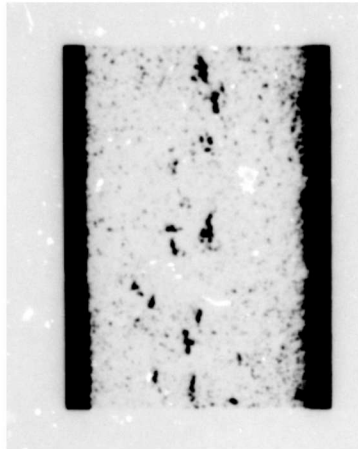
MSL-70-23, Vol. IV

1.04 mm → 1.99 mm



0.232 mm/μs

0.55 mm → 0.96 mm



0.308 mm/μs

Reproduced from  
best available copy.

0.22 mm → 0.54 mm



0.314 mm/μs

Figure 33  
Spall Fractures in Titanium, 3.2 mm  
Stock (20°C)

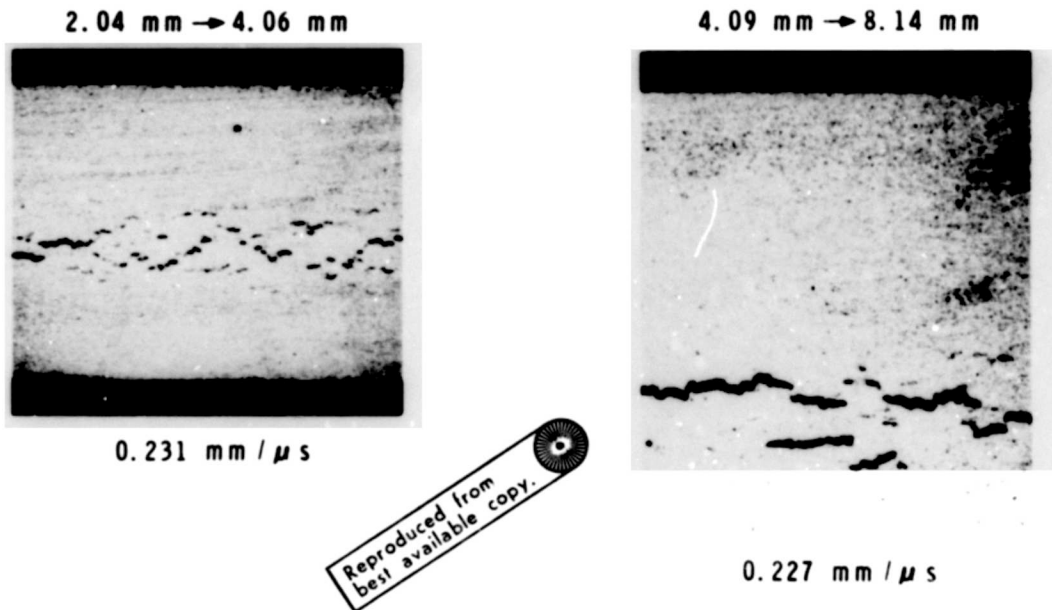


Figure 34 Spall Fractures in Titanium, 12.7 mm Stock (20°C)

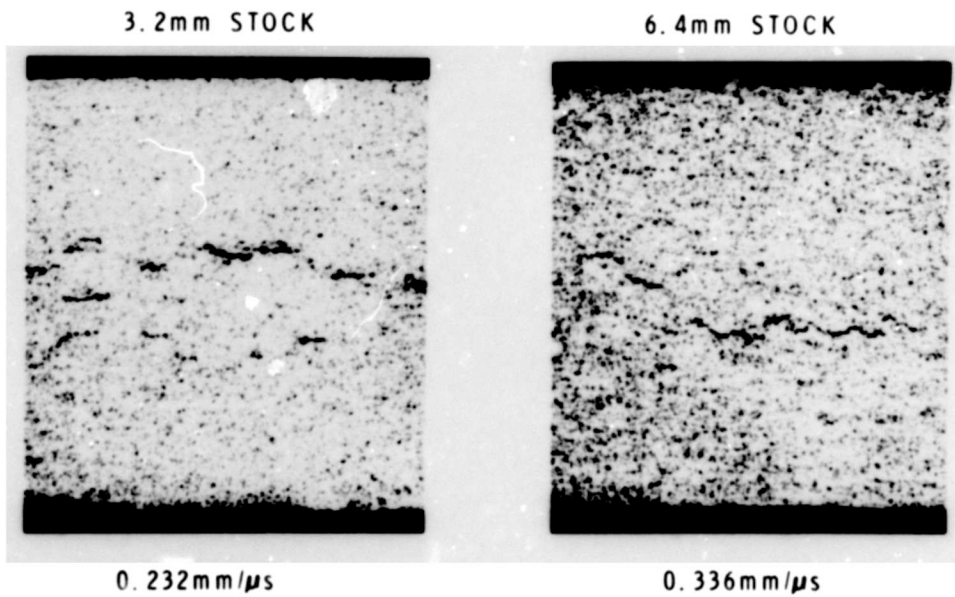


Figure 35 Spall Fractures in Titanium, Material Effects (1 mm + 2 mm, 20°C)

MSL-70-23, Vol. IV

target data was not considered representative of bulk material response. Figure 35 shows the difference in spall fracture for the 3.2 and 6.4 mm materials. For the same impactor/ target combination and approximately the same damage level, the velocity is over 40% higher for the 6.4 mm stock.

Scanning microfractographs of fracture surfaces for completely spalled specimens are shown in Figures 36 and 37. The 3.2 and 6.4 mm stock both showed ductile fracture, but the 6.4 mm material had much smaller void formation. The 12.7 mm stock, even though its incipient spall threshold was the same as 3.2 mm (for the same thickness), showed a coarser fracture with numerous brittle fracture facets. This may be due to grain boundary failure resulting from embrittlement by impurity elements.

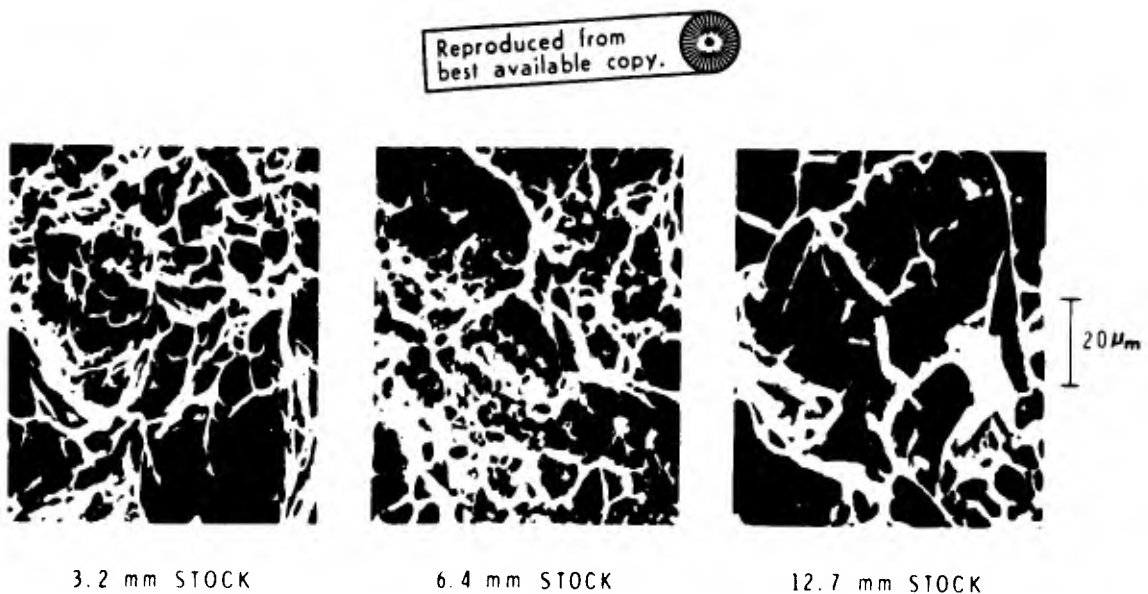


Figure 36 Spall Fracture Surfaces in Titanium, Material Effects (20°C)

Reproduced from  
best available copy.

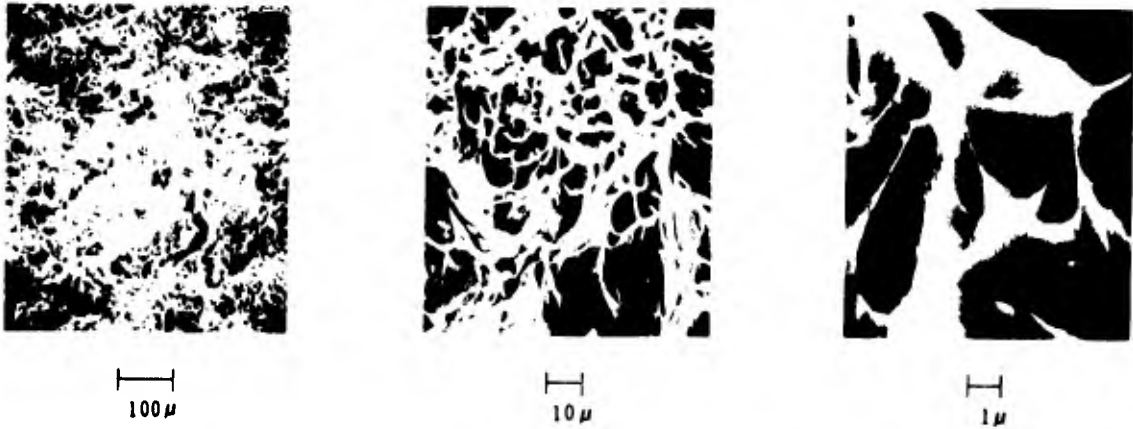


Figure 37 Spall Fracture Surface in Titanium,  
3.2 mm Stock (0.5 mm → 1 mm, 20°C)

Temperature dependence of spall in titanium is given in Figure 38. The impact velocity for incipient spall has increased for a temperature increase of 20° to 500°C. This behavior may be related to the increased ductility of titanium at elevated temperature, particularly above 400°C.<sup>(19)</sup> However, as Charest has pointed out<sup>(68)</sup>, the use of a room temperature impactor and a heated target (as was done here), gives impedance differences that influence release wave structure and therefore stress-time history in the target. Optical and scanning electron microscope pictures of titanium specimens tested at several temperatures are shown in Figures 39 to 41. Ductile rupture is evident at 20° and 500°C, but there are indications of brittle, cleavage-type fracture at -195°C.

MSL-70-23, Vol. IV

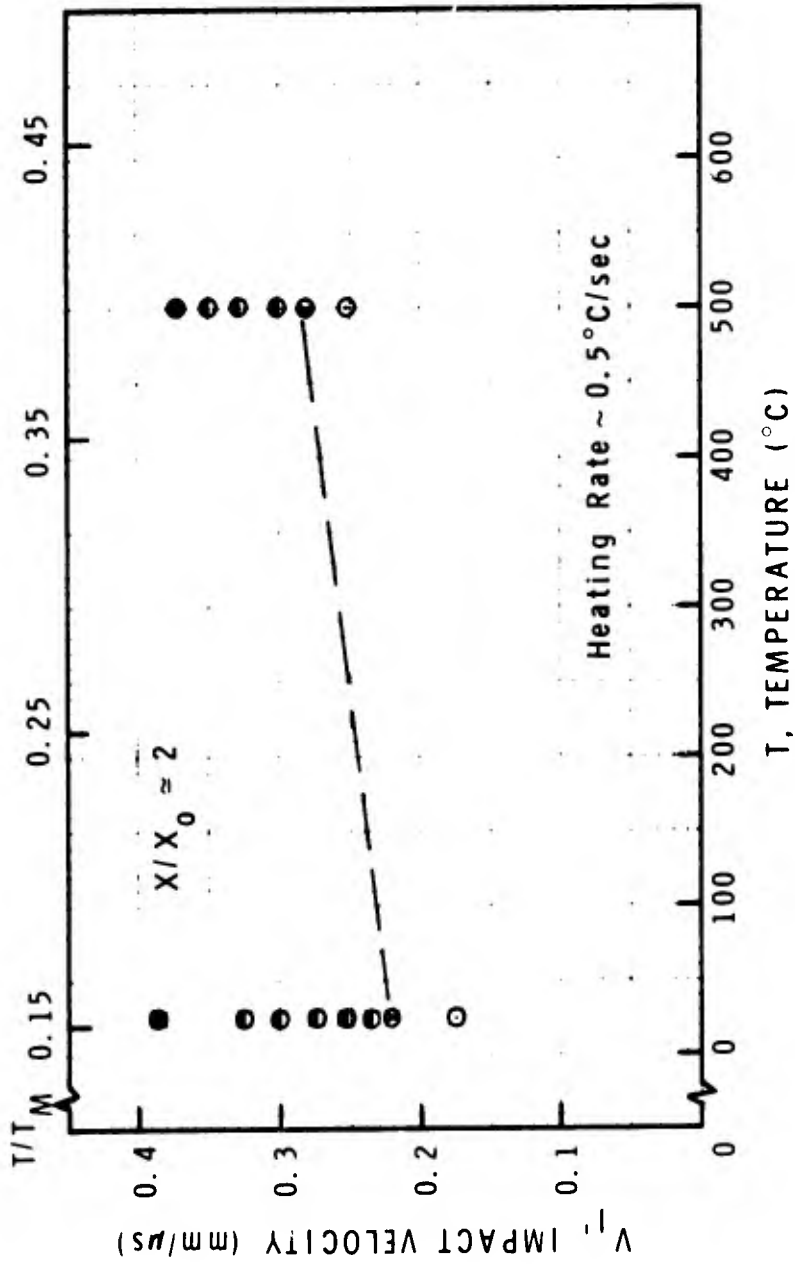


Figure 38 Spall Data for Titanium, Temperature Effect (1 mm → 2 mm, 3.2 mm Stock)

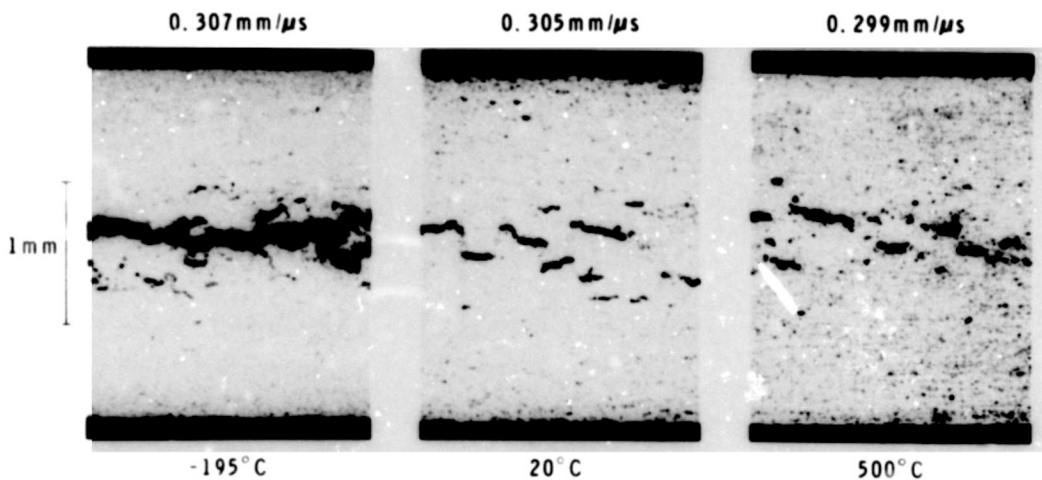



Figure 39 Spall Fractures in Titanium, Temperature Effects (1 mm → 2 mm, 3.2 mm Stock)

Reproduced from  
best available copy. 

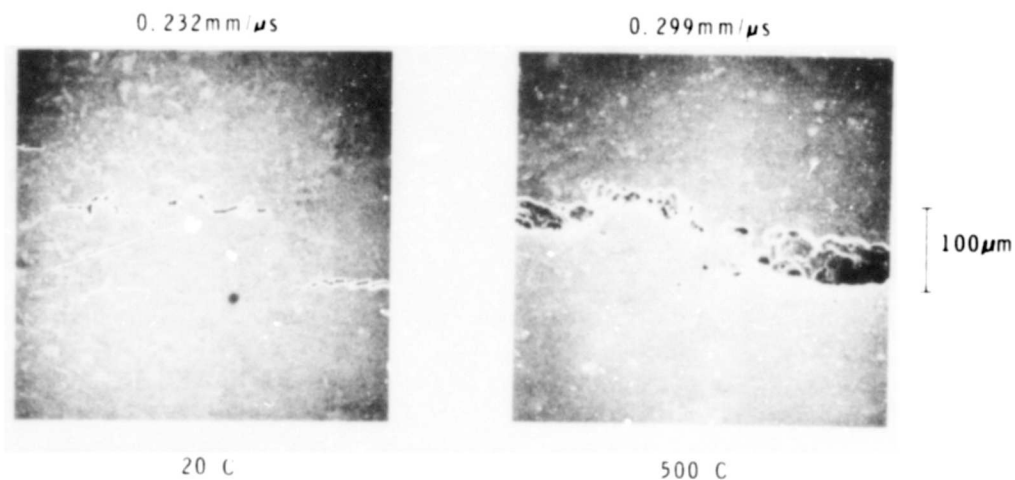


Figure 40 Spall Fractures in Titanium, Temperature Effects (1 mm → 2 mm, 3.2 mm Stock)

MSL-70-23, Vol. IV

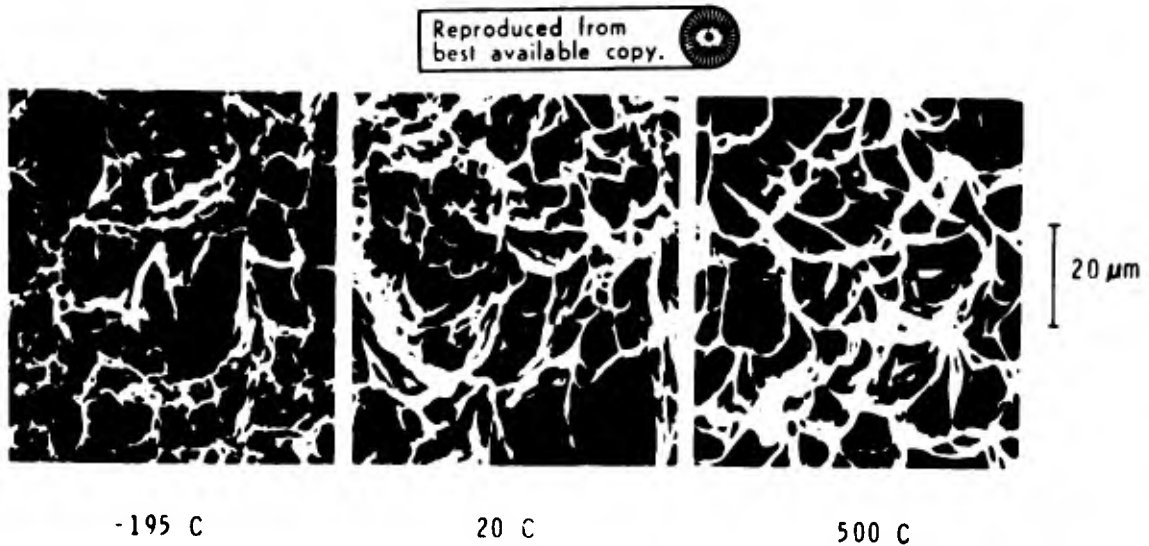


Figure 41 Spall Fracture Surfaces in Titanium,  
Temperature Effects (1 mm  $\rightarrow$  2 mm,  
3.2 mm Stock)

#### SPALL PROFILES

Complete wave profiles were obtained under spall-producing conditions using a titanium-into-titanium configuration, with a free rear surface on the impactor to give complete release and a free rear surface on the target for reflection of the compressive wave. The wave interactions resulting from such a test are shown schematically in Figure 42, with several simplifying assumptions. The shock is shown as a single wave and unloading or release is considered as a simple rarefaction fan. Also, small interactions between shock waves are omitted, and fracture is assumed to occur along a single surface (spall plane) rather than in a volume around this plane. Wave interactions are shown as if the material exhibits time-dependent fracture, i.e., the percentage of fractured area increases with time until the entire spall surface has separated. After separation, any waves trapped in the spalled piece reverberate, giving a sinusoidal motion to the rear surface.

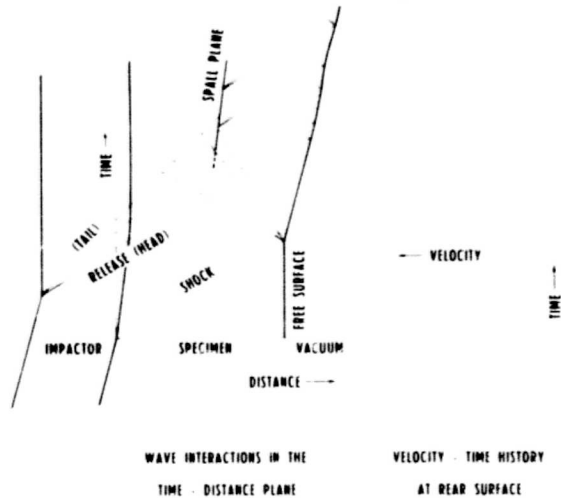


Figure 42 Wave Interaction in Spall Test and Velocity-Time History

Measured profiles for unattenuated pulses are given in Figure 43, with photomicrographs of the recovered and sectioned targets. Also shown for reference are the incipient and complete spall levels for this impactor/target combination as determined from recovery tests. Evidence of fracture is shown as a reversal of the release wave. The amount of pullback (decrease in free surface velocity to the point of first reversal) may be related to the spall strength of the material for a given impact geometry. An empirical relation for this has been given by Taylor as: <sup>(69)</sup>

$$\sigma_S = \rho C (\Delta u_{fs}/2) \quad (25)$$

where  $\sigma_S$  is spall strength,  $\rho$  and  $C$  are local density and longitudinal wave speed, and  $\Delta u_{fs}$  is pullback.



MSL-70-23, Vol. IV

The data in Figure 43 give  $\sigma_s \approx 30$  kbar. This calculated spall strength is not constant for a given material since it is proportional to  $\Delta u_{fs}$ . This factor has been found to change with target temperature, pulse width and pulse shape for 6061-T6 aluminum<sup>(70)</sup>, and other metals such as titanium probably show similar behavior. However, for a given set of impact conditions (thicknesses, temperature), the pullback is relatively insensitive to maximum compressive stress as well as to degree of fracture.

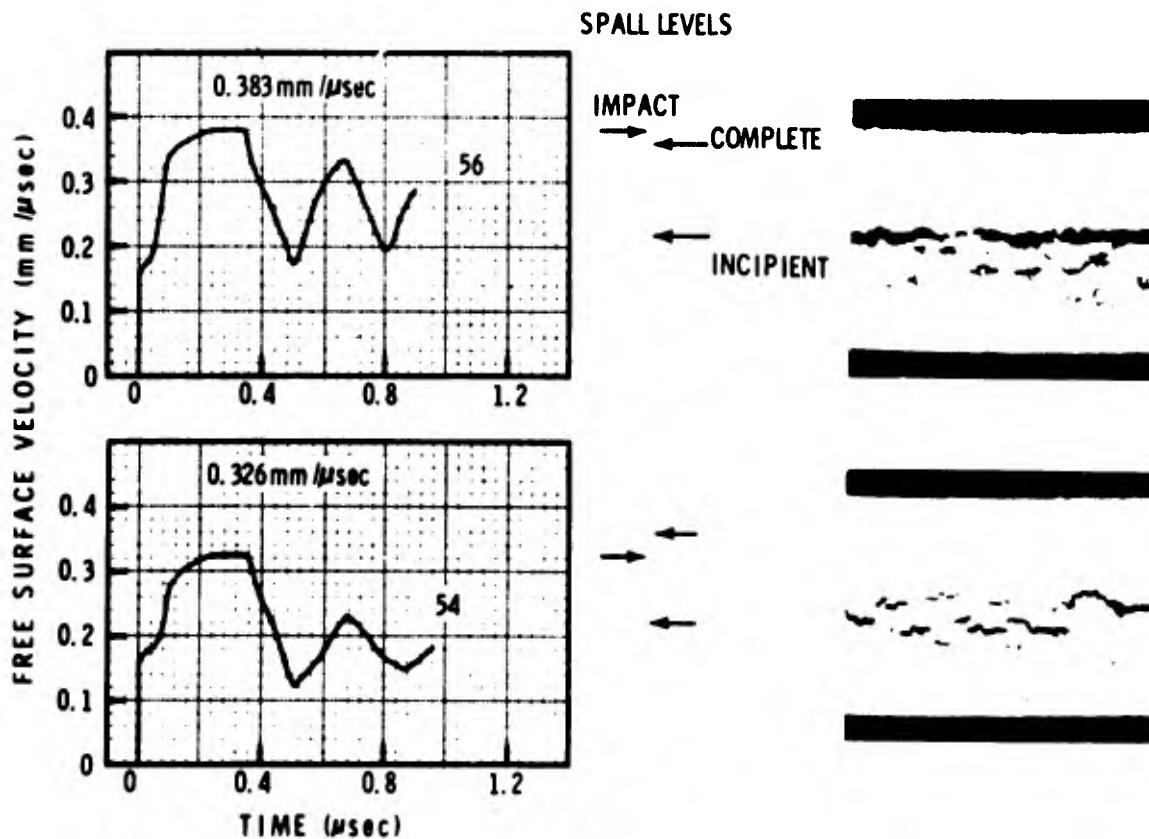


Figure 43 Spall Wave Profiles in Titanium

The spall profile from Test 56 is compared with that calculated using SWAP-7<sup>(71)</sup> in Figure 44. SWAP-7 is a method of characteristics code for elastic-plastic wave propagation calculations. Fracture was included by forming a new free surface at the nominal spall plane when the tensile stress at that plane reached the spall strength. The calculated profile agrees with the measured profile reasonably well on the basis of velocity levels and wave pullback times. However, as would be expected, the actual wave structure is not matched since effects such as precursor decay, non-steady state waves, strain rate sensitivity, strain hardening, Bauschinger effect and time-dependent fracture are not included. The spall profile from an attenuated pulse test, where the impact velocity was above that required for spall, is given in Figure 45.

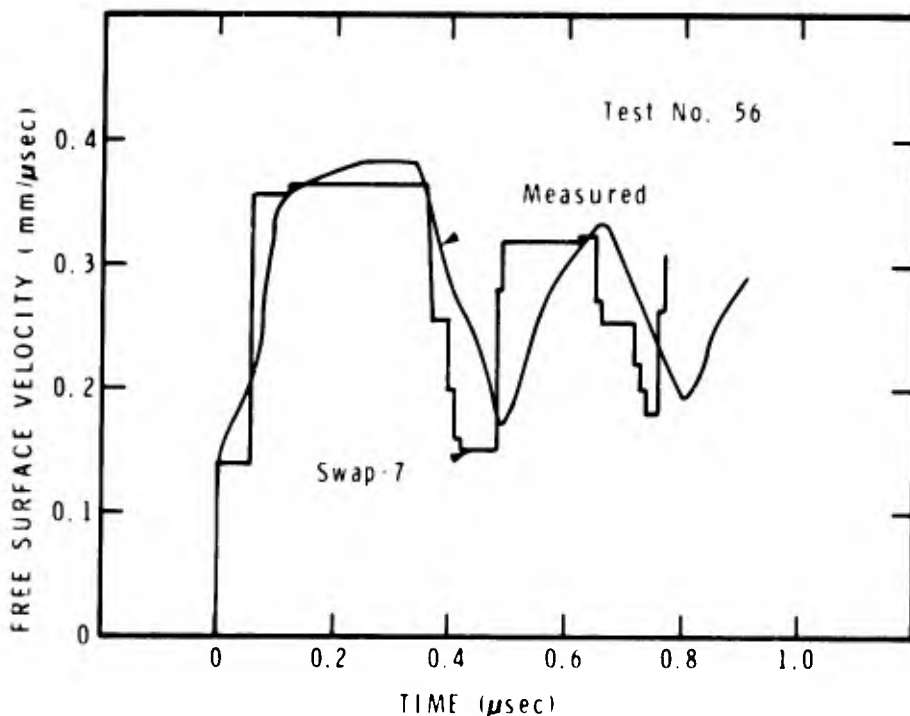


Figure 44 Measured and Calculated Spall Profiles, Titanium

MSL-70-23, Vol. IV

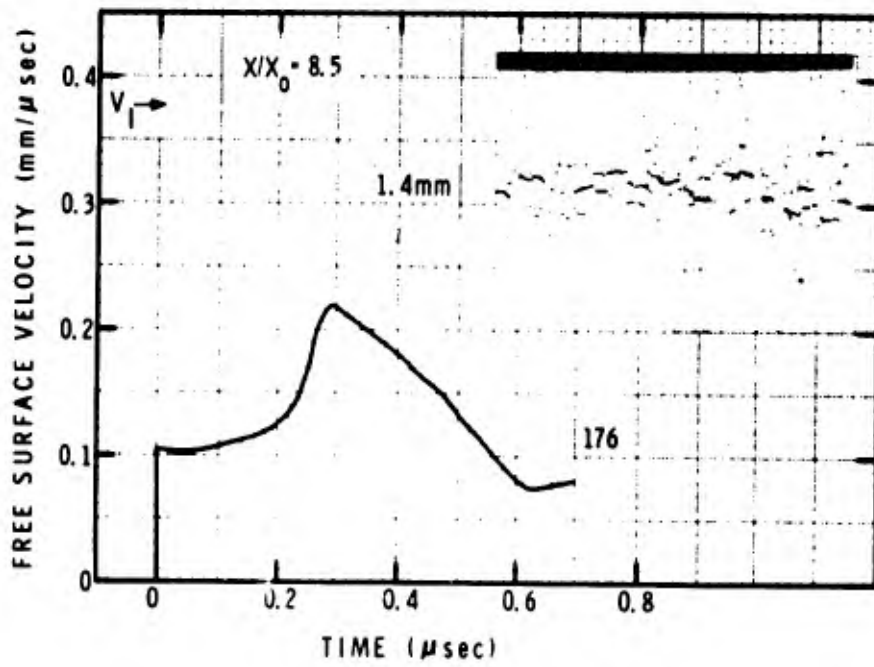


Figure 45 Attenuated Spall Profile in Titanium

## SUMMARY

The dynamic properties of alpha titanium were measured under uniaxial stress and uniaxial strain conditions. The material tested was sheet and plate stock with average hardness of 59R<sub>A</sub>. Material response to compressive uniaxial stress deformation showed evidence of a yield drop above a strain rate of ~ 100/sec and slight strain-hardening. At 20°C, the yield increased from ~ 5.3 kbar at 0.005/sec to ~ 9 kbar at 600/sec, while at 370°C the yield increased from ~ 0.6 kbar at 0.006/sec to ~ 5 kbar at 1100/sec.

Longitudinal and shear wave velocities were measured as functions of temperature and pressure, giving the following (in mm/μsec):

$$C_L = 6.135 - 0.00083T$$

$$C_S = 3.261 - 0.00076T$$

(T in °C)

$$C_L = 6.118 + 0.0056P$$

$$C_S = 3.246 + 0.00140P$$

(P in kbar)

Principal elastic constants were evaluated at T = 20°C and P = 0, including:

MSL-70-23, Vol. IV

$$\text{Bulk Modulus} = K_0^S = 1052 \text{ kbar}$$

$$\left( \frac{\partial K^S}{\partial P} \right)_S = 3.62, \quad \left( \frac{\partial K^S}{\partial P} \right)_T = 3.68$$

$$\text{Shear Modulus} = G_0^S = 474 \text{ kbar}$$

$$\left( \frac{\partial G^S}{\partial P} \right)_S = 0.68, \quad \left( \frac{\partial G^S}{\partial P} \right)_T = 0.75$$

$$\text{Poisson's Ratio} = 0.304$$

Elastic wave velocity data were also used in determining the Gruneisen parameter  $\gamma$  and the Debye temperature  $\theta$ :

$$\gamma = 1.11 \text{ @ } T = 20^\circ\text{C and } P = 0$$

$$\frac{\partial \gamma}{\partial T} = -0.00036/^\circ\text{C @ } T = 20^\circ\text{C}$$

$$\frac{\partial \gamma}{\partial P} = -0.0058/\text{kbar @ } P = 0$$

$$\theta = 415^\circ\text{K}$$

The shock wave hugoniot was determined experimentally to be:

$$\sigma_H = 2.5 + 225 u_p + 49.9 u_p^2 \quad (\sigma_H < 90 \text{ kbar})$$

Assumption of an ideal elastic-plastic wave structure with a 15 kbar hugoniot elastic limit and equilibrium initial and final states gave:

$$\sigma_H = 4.5 + 1130u + 1410u^2$$

$$P_H = 1130\mu + 1410\mu^2$$

$$U_S = 5.02 + 1.245 u_p$$

The hydrostat as determined from elastic constants data was:

$$P_H = 4220 \left[ (1+\mu)^{0.95} - 1 \right] - 2931 \ln (1+\mu) + 450 \left( \frac{\mu}{1+\mu} \right)^3$$

(Keane equation of state)

Measurements of shock wave stress and velocity indicated a phase change ( $\alpha \rightarrow \omega$ ) in the range of 90 to 125 kbars.

Measurements of compressive wave development showed the wave front to be characterized by a well-defined elastic portion and a transition to a spreading plastic wave. Elastic precursor decay was  $\sim 60\%$  to 17 kbar after 6 mm of travel. Peak pressure attenuation was  $\sim 45\%$  at  $X/X_0 = 13$  for a 41 kbar, 0.3  $\mu\text{sec}$  pulse, and  $\sim 60\%$  at  $X/X_0 = 20$  for a 152 kbar, 0.08  $\mu\text{sec}$  pulse.

Spall fracture was determined for several elastic pulse widths ranging from 0.07 to 1.34  $\mu\text{sec}$ . The incipient spall threshold, expressed as impact velocity, increased with decreasing pulse width, and increased with increasing temperature for 20° and 500°C. Spall fractures were somewhat dispersed around the nominal spall plane. Failure was generally of a ductile nature, although void size varied for the different stock thicknesses and the 12.7 mm plate showed evidence of brittle-type grain boundary failure.

MSL-70-23, Vol. IV

## ACKNOWLEDGMENTS

The authors wish to thank Mr. N. H. Froula and Mr. A. R. McMillan for contribution to the equation of state and wave propagation studies, Mr. F. L. Schierloh for assistance in the strain rate work, Dr. B. Taylor for the transmission electron microscopy, and Dr. H. Chin for development of the data analysis programs. Also, the assistance of the following Materials and Structures Laboratory personnel in the experimental work is gratefully recognized:

Mr. B. Bielski and Mr. J. Wigton for specimen preparation; Mr. F. Stemczynski and Mr. E. Stretanski for EOS and wave profile tests; Mr. J. Havens for ultrasonics measurements; Mr. C. Woodcock for spall tests; Mr. J. Bonner and Mr. H. Simmons for strain rate tests; Mr. C. Whitchurch and Mr. L. Seltz for metallographic work; and Mrs. W. Trippen and Mrs. C. Strong for data analysis.

## REFERENCES

1. "A Selected Bibliography on Dynamic Properties of Materials", compiled by Christman, D. R., General Motors Corporation, Manufacturing Development, DASA 2511, June, 1970 (AD 710823).
2. Metals Handbook, 8th. Ed., Vol. 1: Properties and Selection of Metals, Lyman, T., Ed., American Society for Metals, Metals Park, Ohio, 1961.
3. Handbook of Chemistry and Physics, 45th. Ed., Weast, R. C., Ed., The Chemical Rubber Co., Cleveland, Ohio, 1964.
4. Thermophysical Properties of High Temperature Solid Materials, Vol. 1: Elements, Touloukian, Y. S., Ed., The McMillan Co., New York, N. Y., 1967.
5. Aerospace Structural Metals Handbook, Chapter Code 3701 (Ti, Commercially Pure Titanium), Mechanical Properties Data Center, Belfour Stulen Inc., Traverse City, Michigan, 1966.
6. Margolin, H. and Nielsen, J. P., "Titanium Metallurgy", Modern Materials, Vol. 2, Hausner, H. H., Ed., p. 225-325, Academic Press, New York, N. Y., 1960.
7. Cowan, J. A., Pawlowicz, A. T. and White, G. K., "Thermal Expansion of Polycrystalline Titanium and Zirconium", Cryogenics, Vol. 8, p. 155-157, 1968.
8. Babcock, S. G., Langan, J. J., Norvey, D. B., Michaels, T. E., Schierloh, F. L. and Green, S. J., "Characterization of Three Aluminum Alloys", General Motors Corporation, Manufacturing Development, AMMRC-CR-71-3, January, 1971 (AD 724195).
9. Holt, D. L., Babcock, S. G., Green, S. J. and Maiden, C. J., "The Strain-Rate Dependence of the Flow Stress in Some Aluminum Alloys", ASM Trans. Quart., Vol. 60, p. 152-159, 1967.
10. Morris, P. R., "Resolved Shear Stress in Elastically Anisotropic Polycrystals", Met. Trans., Vol. 2, p. 1949-1952, 1971.
11. Rogers, D. H. and Roberts, W. T., "Plastic Anisotropy of Titanium and Zinc Sheet - II. Crystallographic Approach", Int. J. Mech. Sci., Vol. 10, p. 221-229, 1968.



MSL-70-23, Vol. IV

12. Lii, Y., Ramachandran, V. and Reed-Hill, R. E., "Some Aspects of the Variation of the Strain Anisotropy in Titanium", Met. Trans., Vol. 1, p. 447-453, 1970.
13. Evans, K. R., "Deformation Mechanisms in Titanium and Titanium-Aluminum Alloys", AIME Trans., Vol. 242, p. 648-653, 1968.
14. Wang, C. and Chang, H., "Deformation Mechanisms in  $\alpha$ -Titanium at Low Temperatures", Foreign Technology Division, FTD-HT-23-1134-67, 1965 (AD 678087).
15. Gegel, H. L. and Duvall, T., "Thermally Activated Deformation in Alpha Titanium", Air Force Materials Laboratory, AFML-TR-69-59, April, 1969 (AD 853530).
16. Beevers, C. J. and Edmonds, D. V., "The Deformation and Fracture of Titanium/Oxygen/Hydrogen Alloys", AIME Trans., Vol. 245, p. 347-352, 1969.
17. Tung, P. P. and Sommer, A. W., "Dislocation Energetics in Alpha Titanium", Met. Trans., Vol. 1, p. 947-953, 1970.
18. Conrad, H., "Thermally Activated Deformation of  $\alpha$ -Titanium Below  $0.4 T_M$ ", Canad. J. Phys., Vol. 45, p. 581-590, 1967.
19. Orava, R. N., Stone, G. and Conrad, H., "The Effects of Temperature and Strain Rate on the Yield and Flow Stresses of  $\alpha$ -Titanium", ASM Trans., Vol. 59, p. 171-184, 1966.
20. Conrad, H., "Project Themis: Metal Deformation Processing", University of Kentucky, AFML-TR-71-18, April, 1971 (AD 884961).
21. Jones, R. L. and Conrad, H., "The Effect of Grain Size on the Strength of Alpha-Titanium at Room Temperature", AIME Trans., Vol. 245, p. 779-789, 1969.
22. Nicholas, T., "Strain-Rate and Strain-Rate-History Effects in Several Metals in Tension", Exp. Mech., Vol. 11, p. 370-374, 1971.
23. Sargent, G. and Conrad, H., "Stress Relaxation and Thermally Activated Deformation in Titanium", Scripta Met., Vol. 3, p. 43-50, 1969.
24. Armstrong, R. W. and Jindal, P. C., "On the Hardness and Recrystallized Grain Size of Alpha Titanium", AIME Trans., Vol. 242, p. 2513, 1968.

25. Christian, J. W., The Theory of Transformations in Metals and Alloys, Pergamon Press, New York, N. Y., 1965.
26. Williams, J. C., Boyer, R. R. and Blackburn, M. J., "The Influence of Microstructure on the Fracture Topography of Titanium Alloys", Electron Microfractography, ASTM-STP-453, American Society for Testing and Materials, p. 215-535, 1969.
27. Frederick, S. F. and Hanna, W. D., "Fracture Toughness and Deformation of Titanium Alloys at Low Temperatures", Met. Trans., Vol. 1, p. 2391-2398, 1970.
28. Seaman, L., Williams, R. F., Rosenberg, J. T., Erlich, D. C. and Linde, R. K., "Classification of Materials by Shock Properties", Stanford Research Institute, AFWL-TR-69-96, 1969 (AD 865505).
29. Fisher, E. S. and Renken, C. J., "Single-Crystal Elastic Moduli and the hcp+bcc Transformation in Ti, Zr, and Hf", Phys. Rev., Vol. 135, p. A482-A494, 1964.
30. Walsh, J. M., Rice, M. H., McQueen, R. G. and Yarger, F. L., "Shock-Wave Compressions of Twenty-Seven Metals, Equation of State of Metals", Phys. Rev., Vol. 108, p. 196-216, 1957.
31. Slater, J. C., Introduction to Chemical Physics, McGraw-Hill Book Co., New York, N. Y., 1939.
32. Dugdale, J. S. and MacDonald, D. K. C., "The Thermal Expansion of Solids", Phys. Rev., Vol. 89, p. 832-834, 1953.
33. Schreiber, E. and Anderson, O. L., "Pressure Derivatives of the Sound Velocities of Polycrystalline Alumina", Am. Ceram. Soc. J., Vol. 49, p. 184-190, 1966.
34. Anderson, O. L. and Dienes, G. J., Non-Crystalline Solids (Chapter 18), Ed. by Frechette, V. D., John Willey and Sons, New York, 1960.
35. Schuele, D. E. and Smith, C. S., "Low Temperature Thermal Expansion of RbI", J. Phys. Chem. Solids, Vol. 25, p. 801-814, 1964.
36. Alers, G. A., "Use of Sound Velocity Measurements in Determining the Debye Temperatures of Solids", Physical Acoustics, Vol. III, Part B (Lattice Dynamics), p. 1-42, Academic Press, New York, N. Y., 1965.

MSL-70-23, Vol. IV

37. Taylor, A. and Kagle, B. J., Crystallographic Data on Metal and Alloy Structures, Dover Publications, Inc., New York, N. Y., 1963.
38. Chin, H. C., "A Computer Program to Analyze X-Cut Quartz Data Obtained from Shock Loading", General Motors Corporation, Manufacturing Development, Materials and Structures Laboratory, MSL-70-15, 1970.
39. Bundy, F. P., "Formation of New Materials and Structures by High-Pressure Treatment", Irreversible Effects of High Pressure and Temperature on Materials, ASTM-STP-374, p.52-67, American Society for Testing and Materials, Philadelphia, Pa., 1964.
40. Jamieson, J. C., "Crystal Structures of Titanium, Zirconium and Hafnium at High Pressures", Science, Vol. 140, p. 72-73, 1963.
41. Jayaraman, A., Klement, W. and Kennedy, G. C., "Solid-Solid Transitions in Titanium and Zirconium at High Pressures", Phys. Rev., Vol. 131, p. 644-649, 1963.
42. Coleburn, N. L., "Shock-Induced Transformations of Titanium-Nickel Alloys", U.S. Naval Ordnance Laboratory, NOLTR-67-78, 1967 (AD 653080).
43. German, V. N., Bakanova, A. A., Tarasova, L. A. and Sumulov, Yu. N., "Phase Transformation of Titanium and Zirconium in Shock Waves", Sov. Phys.-Solid State, Vol. 12, p. 490-491, 1970.
44. McQueen, R. G., Marsh, S. P., Taylor, J. W., Fritz, J. N. and Carter, W. J., "The Equation of State Solids from Shock Wave Studies", High-Velocity Impact Phenomena, p. 293-417, Academic Press, New York, N. Y., 1970.
45. Isbell, W. M., Shipman, F. H. and Jones, A. H., "Hugoniot Equation of State Measurements for Eleven Materials to Five Megabars", General Motors Corporation, Manufacturing Development, Materials and Structures Laboratory, MSL-68-13, 1968 (AD 721920).
46. Birch, F., "The Effect of Pressure Upon the Elastic Parameters of Isotropic Solids, According to Murnaghan's Theory of Finite Strain", J. Appl. Phys., Vol. 9, p. 279-288, 1938.
47. Birch, F., "Elasticity and Constitution of the Earth's Interior", J. Geophys. Res., Vol. 57, p. 227-286, 1952.

48. Murnaghan, F. D., "The Compressibility of Media Under Extreme Pressures", Proc. Nat. Ac. Sci., Vol. 30, p. 244-247, 1944.
49. Keane, A., "An Investigation of Finite Strain in an Isotropic Material Subjected to Hydrostatic Pressure and its Seismological Applications", Australian J. Phys., Vol. 7, p. 323-333, 1954.
50. Anderson, O. L., "On the Use of Ultrasonic and Shock-Wave Data to Estimate Compressions at Extremely High Pressures", Phys. Earth Planet. Interiors, Vol. 1, p. 169-176, 1968.
51. Duvall, G. E. and Zwolinski, B. J., "Entropic Equations of State and Their Applications to Shock Wave Phenomena in Solids", Acoust. Soc. Am. J., Vol. 27, p. 1054-1058, 1955.
52. Lamberson, D. L., "The High Pressure Equation of State of Tantalum, Polystyrene and Carbon Phenolic Determined from Ultrasonic Velocities", Doctoral Dissertation, Air Force Institute of Technology (AFIT-SE), Wright-Patterson AFB, Ohio, 1969.
53. Zel'dovich, Y. B. and Raizer, Y. P., Physics of Shock Waves and High-Temperature Hydrodynamic Phenomena, Vol. 2, Academic Press, New York, N. Y., p. 688-709, 1967.
54. Ruoff, A. L., "Linear Shock-Velocity-Particle-Velocity Relationship", J. Appl. Phys., Vol. 38, p. 4976-4980, 1967.
55. Gschneidner, K. A., "Physical Properties and Interrelationships of Metallic and Semimetallic Elements", Solid State Physics, Vol. 16, p. 275-426, 1964.
56. Garde, A. M. and Reed-Hill, R. E., "The Importance of Mechanical Twinning in the Stress-Strain Behavior of Swaged High Purity Fine-Grained Titanium Below 424°K", Met. Trans., Vol. 2, p. 2885-2888, 1971.
57. Breedis, J. F. and Koul, M. K., "Strengthening of Titanium Alloys by Shock Deformation", Massachusetts Institute of Technology, AFML-TR-69-14, 1969 (AD 851481).
58. Partridge, P. G., "The Crystallography and Deformation Modes of Hexagonal-Close-Packed Metals", Met. Rev., Vol. 12, p. 169-194, No. 118, 1967.
59. Read, H. E., Triplett, J. R. and Cecil, R. A., "Dislocation Dynamics and the Formulation of Constitutive Equations for Rate Dependent Plastic Flow in Metals", Systems, Science, and Software, DASA 2638, Dec., 1970 (AD 722314).

## MSL-70-23, Vol. IV

60. McMillan, A. R., Isbell, W. M. and Jones, A. H., "High Pressure Shock Wave Attenuation", General Motors Corporation, Manufacturing Development, Materials and Structures Laboratory, DASA 2425, June, 1971.
61. Keller, D. V. and Tuler, F. R., "Predix Metals Report", Preliminary Draft, Effects Technology, Inc., CR-70-06, 1970.
62. Stefansky, T. and Shea, J. H., "Dynamic Fracture Experiments Using High-Energy Pulsed Electron Beams", Physics International Co., DASA 2699, July, 1971 (AD 727983).
63. Christman, D. R., Isbell, W. M., Babcock, S. G., McMillan, A. R. and Green, S. J., "Measurements of Dynamic Properties of Materials, Vol. III: 6061-T6 Aluminum", General Motors Corporation, Manufacturing Development, Materials and Structures Laboratory, DASA 2501-3, 1971.
64. Isbell, W. M., Christman, D. R. and Babcock, S. G., "Measurements of Dynamic Properties of Materials, Vol. VI: Tantalum", General Motors Corporation, Manufacturing Development, Materials and Structures Laboratory, DASA 2501-6, 1971.
65. Christman, D. R., Isbell, W. M. and Babcock, S. G., "Measurements of Dynamic Properties of Materials, Vol. V: OFHC Copper", General Motors Corporation, Manufacturing Development, Materials and Structures Laboratory, DASA 2501-5, 1971 (AD 728846).
66. Maiden, C. J. and Green, S. J., "Response of Materials and Structures to Suddenly Applied Stress Loads", General Motors Corporation, Manufacturing Development, Materials and Structures Laboratory, DASA 1716, October, 1965 (AD 476613).
67. Charest, J. A., "Spall Compendium", E,G&G, Santa Barbara Division, 1971.
68. Charest, J. A., Horne, D. E. and Jenrette, B. D., "Phenomenological Considerations for Spall Measurements", E,G&G, Santa Barbara, Division, S-56-TP, Jan., 1970.
69. Taylor, J. W., "Stress Wave Profiles in Several Metals", Dislocation Dynamics, p. 573-589, McGraw-Hill Book Co., New York, N. Y., 1968.

70. Isbell, W. M. and Christman, D. R., "Shock Propagation and Fracture in 6061-T6 Aluminum from Wave Profile Measurements", General Motors Corporation, Manufacturing Development, Materials and Structures Laboratory, DASA 2419, April, 1970 (AD 705536).
71. Barker, L. M., "SWAP-7: A Stress-Wave Analyzing Program", Sandia Laboratories, SC-RR-67-143, April, 1967.

$$\nu = [0.5 - (C_S/C_L)^2] / [1.0 - (C_S/C_L)^2]$$

(Poisson's Ratio)

$$K = \rho C_B^2 = \rho (C_L^2 - 4/3 C_S^2)$$

(Bulk Modulus)

$$G = \rho C_S^2$$

(Shear or Rigidity Modulus)

$$E = 2\rho(1+\nu) C_S^2$$

(Young's or Elastic Modulus)

$$\lambda = 2\rho\nu C_S^2 / (1-2\nu)$$

(Lamé's Parameter)

$$K_0^T = \frac{K_0^S}{1 + \nu \gamma_0^T}$$

where  $\gamma_0^T = \frac{\rho K_0^S}{\rho_0 c_p}$

$$K_{0S}^{S'} = K_{0T}^{S'} + \left( \frac{\rho K_0^S}{\rho_0 c_p} \right) \gamma_0^T \left( \frac{\rho_0 c_p}{K_0^S} \right)$$

MSL-70-23, Vol. IV

$$K_{0T}^{T'} = K_{0T}^{S'} + \beta \gamma_0 T \left( \frac{K_0^T}{K_0^S} \right) \left[ 1 - \frac{2}{\beta K_0^T} \left( \frac{\partial K^T}{\partial T} \right)_0 - 2K_{0T}^{S'} \right]$$

$$+ \left[ \beta \gamma_0 T \left( \frac{K_0^T}{K_0^S} \right) \right]^2 \left[ K_{0T}^{S'} - 1 - \frac{1}{\beta^2} \left( \frac{\partial \beta}{\partial T} \right)_0 \right]$$

$$K_{0S}^{T'} = K_{0T}^{T'} + \left( \frac{\partial K^T}{\partial T} \right)_0 \left( \frac{\gamma_0 T}{K_0^S} \right)$$

$$\left( \frac{\partial K^S}{\partial T} \right)_S = \left( \frac{\partial K^S}{\partial T} \right)_0 + K_{0T}^{S'} \left( \frac{K_0^S}{\gamma_0 T} \right)$$

$$\left( \frac{\partial K^T}{\partial T} \right)_0 = \frac{\left( \frac{\partial K^S}{\partial T} \right)_0 - \beta \gamma_0 K_0^T - \beta T K_0^T \left( \frac{\partial \gamma}{\partial T} \right)_0 - \gamma_0 T K_0^T \left( \frac{\partial \beta}{\partial T} \right)_0}{(1 + \beta \gamma_0 T)}$$

$$\left( \frac{\partial K^T}{\partial T} \right)_S = \left( \frac{\partial K^T}{\partial T} \right)_0 + K_{0T}^{T'} \left( \frac{K_0^S}{\gamma_0 T} \right)$$

$$G_0^T = G_0^S = G_0$$

$$G_{0T}^T = G_{0T}^{S'} = G_{0T}'$$



$$G'_{0S} = G'_{0T} + \left( \frac{\partial G}{\partial T} \right)_0 \left( \frac{\gamma_0^T}{K_0^S} \right)$$

$$\left( \frac{\partial G}{\partial T} \right)_S = \left( \frac{\partial G}{\partial T} \right)_0 + G'_{0T} \left( \frac{K_0^S}{\gamma_0^T} \right)$$

MSL-70-23, Vol. IV

APPENDIX B

GRUNEISEN PARAMETER ESTIMATES

1. The Gruneisen parameter is expressed thermodynamically as

$$\gamma = - \frac{1}{\rho c_p} \left( \frac{\partial V}{\partial T} \right)_P \left( \frac{\partial P}{\partial V} \right)_S = \frac{\beta K S}{\rho c_p}$$

For an isotropic elastic solid, this becomes

$$\gamma = \frac{\beta}{c_p} \left( c_L^2 - \frac{4}{3} c_S^2 \right)$$

Substituting appropriate values for titanium gives

$$\gamma_0 = 1.11$$

2. Slater developed a relation that was an extension of the Debye Theory for a three-dimensional continuum, and assumed Poisson's ratio was independent of volume and  $\gamma$  is the same for all vibrational frequencies:

$$\gamma = - \frac{V}{2} \left( \frac{\partial^2 P / \partial V^2}{\partial P / \partial V} \right) - \frac{2}{3}$$

which simplifies at zero pressure to

$$\gamma_0 = \frac{1}{2} \left( K_{0S}^{S'} - \frac{1}{3} \right) = 2S - \frac{2}{3}$$

where S is from  $U_S = C_B + Su_p$ .

Ultrasonic data gives  $S = 1.155$  and  $\gamma = 1.64$ .

Shock wave data gives  $S = 1.245$  and  $\gamma = 1.82$ .

3. Dugdale and MacDonald give an expression for plane wave velocity vs. volume in a three-dimensional continuum that leads to an expression for  $\gamma$  differing from Slater's by a constant (1/3):

$$\gamma = - \frac{V}{2} \left( \frac{\partial^2 P / \partial V^2}{\partial P / \partial V} \right) - 1$$

which simplifies at zero pressure to

$$\gamma_0 = \frac{1}{2} \left( K_{0S}^{S'} - 1 \right) = 2S - 1$$

From ultrasonic data,  $\gamma = 1.31$ .

From shock wave data,  $\gamma = 1.49$ .

4. Anderson and Dienes give expressions for  $\gamma$  in terms of the longitudinal and shear modes of wave propagation:

MSL-70-23, Vol. IV

$$\gamma_L = \frac{1}{3} + \frac{K_0^T}{C_L} \left( \frac{dC_L}{dP} \right)_0$$

$$\gamma_S = \frac{1}{3} + \frac{K_0^T}{C_S} \left( \frac{dC_S}{dP} \right)_0$$

Ultrasonic data gives  $\gamma_L = 1.29$  and  $\gamma_S = 0.67$

5. Schuele and Smith give expressions for the "low-temperature" and "high-temperature" Gruneisen ratio, where low-temperature is the range in which it is assumed the solid behaves as a continuum and high-temperature is the range where all vibrational modes are excited and  $\gamma$  is constant:

$$\gamma_{LT} = \frac{1}{2+\epsilon^3} \left( \epsilon^3 \gamma_L + 2\gamma_S \right)$$

$$(\epsilon = C_S/C_L)$$

$$\gamma_{HT} = \frac{1}{3} \left( \gamma_L + 2\gamma_S \right)$$

Using ultrasonic data and  $\gamma_L$  and  $\gamma_S$  from above gives

$$\gamma_{LT} = 0.71 \text{ and } \gamma_{HT} = 0.88.$$

(All of the ultrasonics data used in this Appendix are for zero pressure and 20°C).

6. Fisher and Manghnani\* discuss the influence of changes in c/a ratio with pressure on calculations of the Gruneisen parameter. They reported values of  $\bar{\gamma}_L = 0.50$  and  $\bar{\gamma}_H = 1.06$  for "low" and "high" temperatures, respectively.

---

\* Fisher, E. S. and Manghnani, M. H., "Effect of Axial Ratio Changes on the Elastic Moduli and Gruneisen  $\gamma$  for Lower Symmetry Crystals", J. Appl. Phys., Vol. 41, p. 5059-5062, 1970.

APPENDIX C

GRUNEISEN PARAMETER, PRESSURE DERIVATIVE

1. Thermodynamic Relation -

$$\gamma = \frac{\beta K^S}{\alpha c_p}$$

$$\left( \frac{\partial \gamma}{\partial P} \right)_T = \gamma_0 \left[ \frac{1}{\beta} \left( \frac{\partial \beta}{\partial P} \right)_T + \frac{1}{K^S} \left( \frac{\partial K^S}{\partial P} \right)_T - \frac{1}{\rho} \left( \frac{\partial \rho}{\partial P} \right)_T - \frac{1}{c_p} \left( \frac{\partial c_p}{\partial P} \right)_T \right]$$

This can be simplified by using:\*

$$\left( \frac{\partial \beta}{\partial P} \right)_T = \left( \frac{1}{K^T} \right)^2 \left( \frac{\partial K^T}{\partial T} \right)_P$$

$$\left( \frac{\partial \rho}{\partial P} \right)_T = \frac{\rho}{K^T}$$

$$\left( \frac{\partial c_p}{\partial P} \right)_T = - \frac{T}{\alpha} \left[ \left( \frac{\partial \beta}{\partial T} \right)_P + \beta^2 \right]$$

\* See, e.g. Thurston, R. N., "Ultrasonic Data and the Thermodynamics of Solids", IEEE Proc., Vol. 53, p. 1320-1336, 1965.

to give:

$$\left(\frac{\partial \gamma}{\partial P}\right)_T = \gamma_0 \left[ \frac{1}{\beta K^T} \left(\frac{\partial K^T}{\partial T}\right)_P + \frac{1}{K^S} \left(\frac{\partial K^S}{\partial P}\right)_T - \frac{1}{K^T} + \frac{T}{c_P \rho} \left\{ \left(\frac{\partial \beta}{\partial T}\right)_P + \beta^2 \right\} \times 23.9 \right]$$

This can be modified to:

$$\left(\frac{\partial \gamma}{\partial P}\right)_T = \frac{\gamma_0}{K^S} \left[ \left(\frac{\partial K^S}{\partial P}\right)_T + \frac{1}{\beta K^T} \left(\frac{\partial K^S}{\partial T}\right)_P - 1 - \gamma - T \left(\frac{\partial \gamma}{\partial T}\right)_P \right]$$

2. Constant  $\gamma/V$ :

$$\frac{\gamma}{V} = \frac{\gamma_0}{V_0} \quad \text{or} \quad \gamma = \rho_0 \gamma_0 V$$

$$\left(\frac{\partial \gamma}{\partial P}\right)_T = \rho_0 \gamma_0 \left(\frac{\partial V}{\partial P}\right)_T$$

but  $\left(\frac{\partial V}{\partial P}\right)_T = -\frac{1}{c^2} \left(\frac{\partial \rho}{\partial P}\right)_T = -\frac{1}{\rho K^T}$

so  $\left(\frac{\partial \gamma}{\partial P}\right)_T = -\frac{\rho_0 \gamma_0}{\rho K^T}$

MSL-70-23, Vol. IV

$$\text{Letting } \rho = \rho_0 \left( \frac{K_0^T + K_{0T}^{T'} P}{K_0^T} \right)^{1/K_{0T}^{T'}}$$

$$\text{and } K^T = K_0^T + K_{0T}^{T'} P$$

gives:

$$\left( \frac{\partial \rho}{\partial P} \right)_T = \frac{-\rho_0}{\left( \frac{1}{K_0^T} \right) \left( 1/K_{0T}^{T'} \right) \left( K_0^T + K_{0T}^{T'} P \right) \left( 1 + K_{0T}^{T'} \right) / K_{0T}^{T'}}$$

At  $P = 0$ , this reduces to

$$\left( \frac{\partial \rho}{\partial P} \right)_T = - \frac{\rho_0}{K_0^T}$$



APPENDIX D

DEVIATORIC STRESS ESTIMATES

The shock wave equation of state for titanium is given by:

$$\left. \begin{aligned} \sigma_H &= 2.5 + 225 u_p + 49.9 u_p^2 \\ \sigma_H &= 4.5 + 1130\mu + 1410\mu^2 \\ P_H &= 1130\mu + 1410\mu^2 \quad (\text{Hydrostat}) \end{aligned} \right\} \quad (\text{D-1})$$

where  $\mu = (v_o/v) - 1$ .

The deviatoric stress ( $\sigma_D$ ) can be defined as the difference between the dynamic stress-compression path ( $\sigma_H - \mu$ ) and the hydrostat, and is a measure of the material's ability to support shear. If the material strain hardens, the deviatoric stress will be a function of  $\mu$ . In Equation D-1,  $\sigma_D$  was assumed constant at 4.5 kbar which gives  $P_H = \sigma_H - 4.5$ .

The deviatoric stress can also be estimated from uniaxial stress data, shock wave data or ultrasonics data as follows:

$$\sigma_D = \sigma_H - P_H = \frac{2}{3} Y \quad (\text{D-2})$$

where Y is flow stress under uniaxial stress conditions.

- A. The flow stress at low strain rate from the uniaxial stress tests (see Figure 4) is  $\sim 7$  kbar, which gives  $\sigma_D = 4.7$  kbar.

MSL-70-23, Vol. IV

B. For a hugoniot elastic limit ( $\sigma_e$ ) of 15 kbar, the relation  $Y = \sigma_e (1-2\nu/1-\nu)$  gives  $Y = 8.4$  kbar. From Equation D-2,  $\sigma_D = 5.6$  kbar.

C. Since  $\sigma_D$  can also be taken as the difference between  $\sigma_H$  and  $P_H$  at a compression corresponding to the hugoniot elastic limit, one has

$$\sigma_D = \sigma_H - P_H = \sigma_e - P_e$$

where

$$\sigma_e = \rho_0 C_L^2 \left( \frac{\mu_e}{1+\mu_e} \right) = 1684 \left( \frac{\mu_e}{1+\mu_e} \right)$$

$$P_e = \rho_0 C_B^2 \left( \frac{\mu_e}{1+\mu_e} \right) = 1050 \left( \frac{\mu_e}{1+\mu_e} \right)$$

For  $\sigma_e = 15$  kbar:  $\mu_e = 0.0090$  and  $P_e = 9.3$  kbar. This gives  $\sigma_D = 5.7$  kbar.

The agreement of these estimates with the value of 4.5 kbar from Equation D-1 is considered good, taking into account the assumptions underlying each method and the experimental inaccuracies.

Also, it should be noted that the stress-axis intercept is larger in the  $\sigma_H - \mu$  plane than the  $\sigma_H - u_p$  plane. Assuming linear elastic and hydrostatic behavior up to the elastic limit, then:

$\sigma_H - u_p$  plane -

$$\sigma_{D_u} = \rho_0 u_e (C_L - C_B)$$

$\sigma_H - \mu$  plane -

$$\sigma_{D_\mu} = \frac{\mu_e}{1+\mu_e} \left( \rho_0 C_L^2 - \rho_0 C_B^2 \right)$$

Using the approximations  $u_e \approx \mu_e/C_L$  and  $\mu_e \approx \mu_e/(1+\mu_e)$ , and subtracting:

$$\Delta\sigma_D = \sigma_{D_u} - \sigma_{D_\mu} = \rho_0 C_B \mu_e (C_L - C_B)$$

For  $\sigma_e = 15$  kbar,  $\mu_e = 0.0090$  and  $\Delta\sigma_D = 2.5$  kbar, compared to  $\Delta\sigma_D = 2.0$  kbar from  $\sigma_H - u_p$  and  $\sigma_H - \mu$  given in Equation D-1.

MSL-70-23, Vol. IV

APPENDIX E

EQUATIONS OF STATE, ULTRASONICS

Numerous analytical and empirical relations have been developed for determining equations of state from ultrasonics data. Some of these are presented here.

1. The Birch equation of state for the isotherm can be expressed as:<sup>\*</sup>

$$P_T = \frac{3}{2} K_0^T \left[ (1+\mu)^{7/3} - (1+\mu)^{5/3} \right] \left[ 1 - \xi \left\{ (1+\mu)^{2/3} - 1 \right\} \right]$$

$$\text{where } \xi = \frac{12-3 K_{0T}^{T'}}{4}$$

$$P_T = 1565 \left[ (1+\mu)^{7/3} - (1+\mu)^{5/3} \right] \left[ 1 - 0.18 \left\{ (1+\mu)^{2/3} - 1 \right\} \right]$$

---

\* Another parameter sometimes used with this equation of state is

$$\alpha \left[ (1+\mu)^{2/3} - 1 \right]^2$$

$$\text{where } \alpha = \frac{3}{8} \left[ K_0^T K_{0T}^{T''} - 7K_{0T}^{T'} + \left( K_{0T}^{T'} \right)^2 + \frac{143}{9} \right]$$

However, this term can usually be neglected, contributing <0.2% at 50 kbar for titanium.

2. The Murnaghan equation of state is derived by assuming the bulk modulus is linear with pressure which gives:

$$\text{Isotherm} - P_T = \frac{K_0^T}{K_{0T}^T} \left[ \begin{array}{cc} & K_{0T}^{T'} \\ (1+\mu) & - 1 \end{array} \right]$$

$$P_T = 277.4 \left[ \begin{array}{cc} & 3.76 \\ (1+\mu) & - 1 \end{array} \right]$$

$$\text{Adiabat} - P_S = \frac{K_0^S}{K_{0S}^S} \left[ \begin{array}{cc} & K_{0S}^{S'} \\ (1+\mu) & - 1 \end{array} \right]$$

$$P_S = 290.6 \left[ \begin{array}{cc} & 3.62 \\ (1+\mu) & - 1 \end{array} \right]$$

3. Instead of a linear bulk modulus-pressure relation, Keane assumed:

$$dK^S = \left[ \frac{(K_0^{S'} - K_\infty^{S'}) K_0^S}{K^S} + K_\infty^{S'} \right] dP$$

where  $K_\infty^{S'}$  is the limiting value of  $K^{S'}$  at very high pressure.

This leads to:

$$P_S = \frac{K_0^S K_{0S}^{S'}}{(K_\infty^{S'})^2} \left[ (1+\mu) K_\infty^{S'} - 1 \right] - \frac{(K_{0S}^{S'} - K_\infty^{S'}) K_0^S}{K_\infty^{S'}} \ln (1+\mu)$$

MSL-70-23, Vol. IV

Huang\* gives the upper bound for  $K^{S'}$  as:

$$K^{S'} = 4S - \frac{11}{3} = K_{0S}^{S'} - \frac{8}{3} = 0.95$$

This gives:

$$P_S = 4220 \left[ (1+\mu)^{0.95} - 1 \right] - 2931 \ln (1+\mu)$$

---

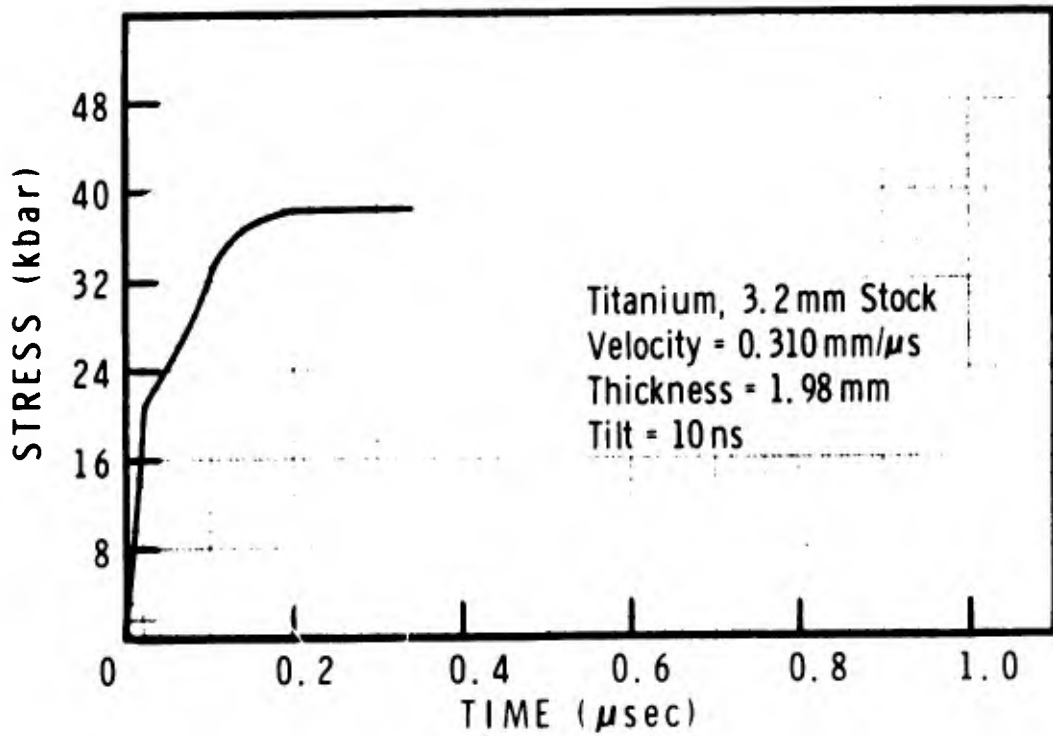
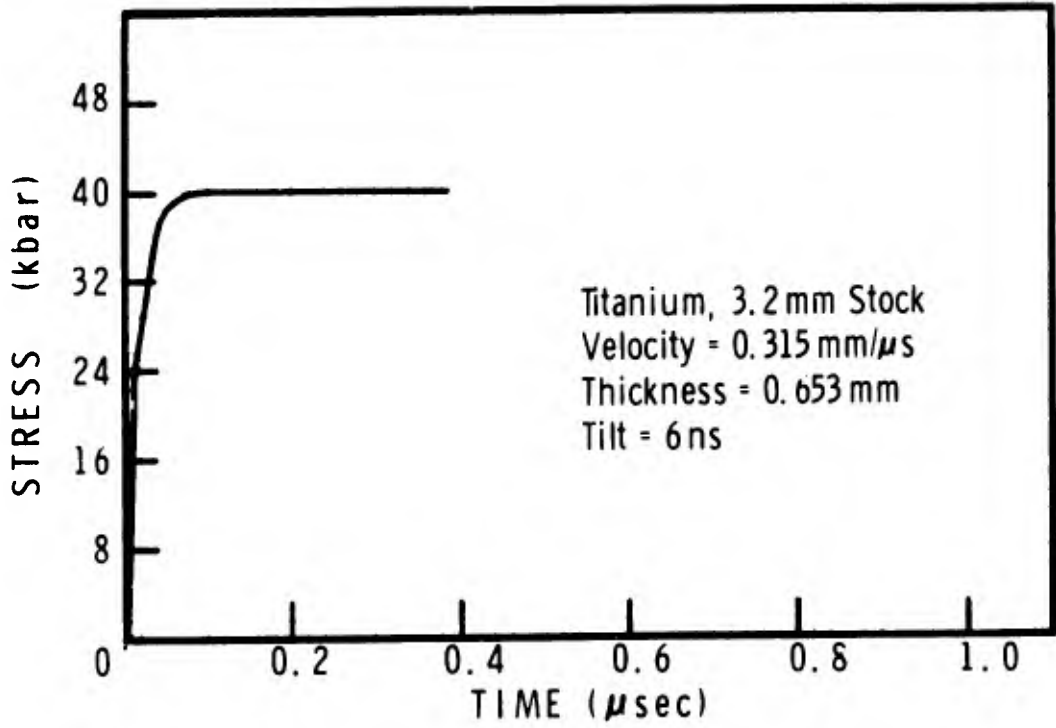
\* Huang, Y. K., "Analytical Approach to the Shock Compressibility of the 18 Cubic-Lattice Metals", J. Chem. Phys., Vol. 53, p. 571-575, 1970.

APPENDIX F

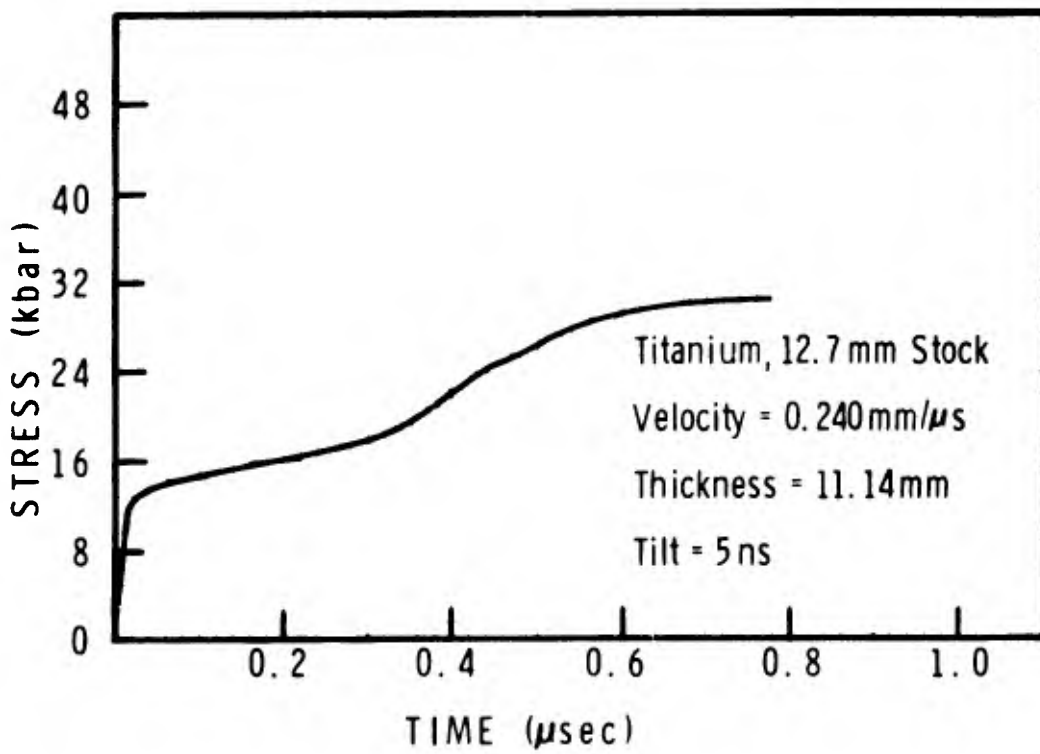
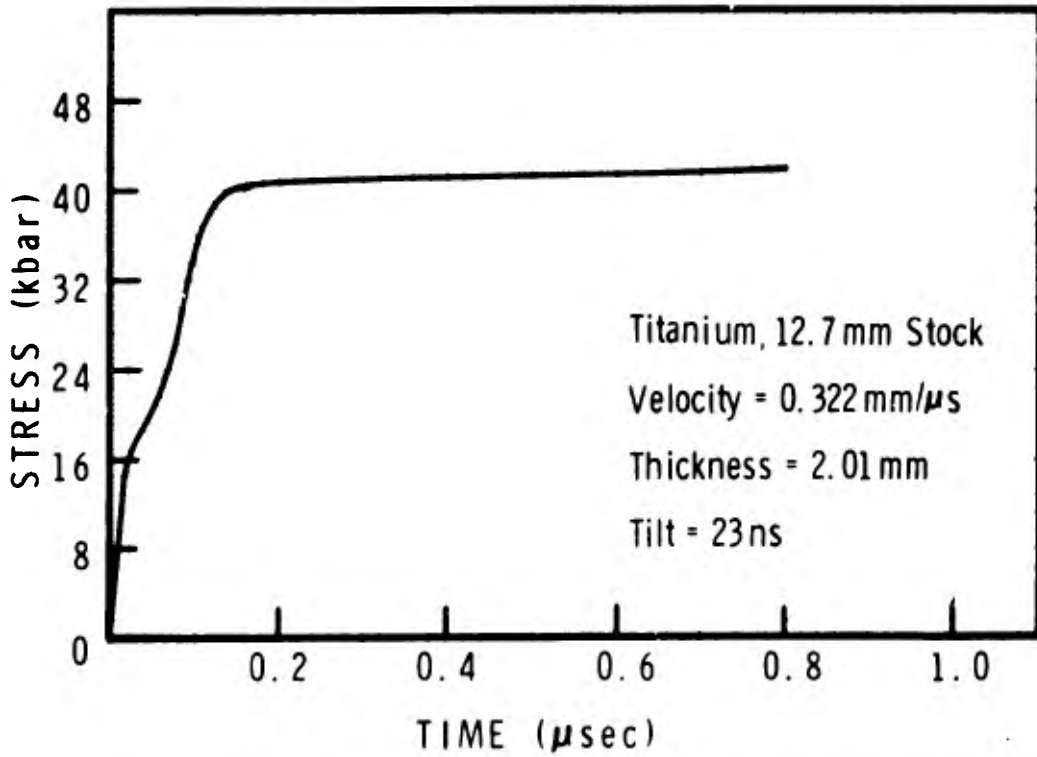
WAVE PROFILES

(Quartz Gage and Velocity Interferometer)

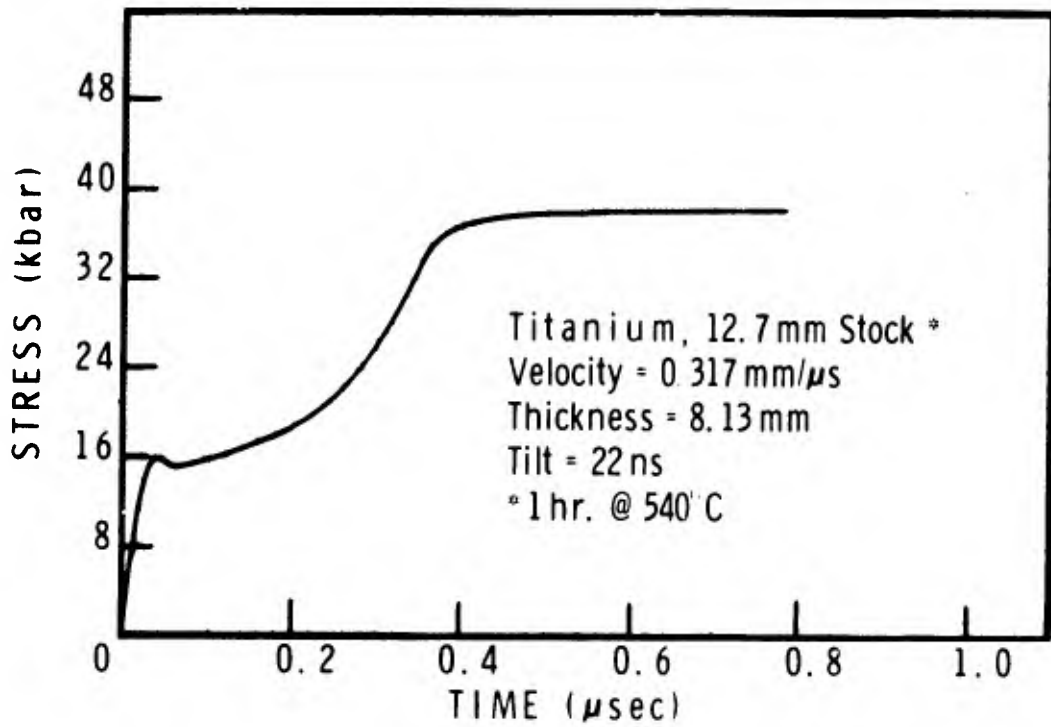
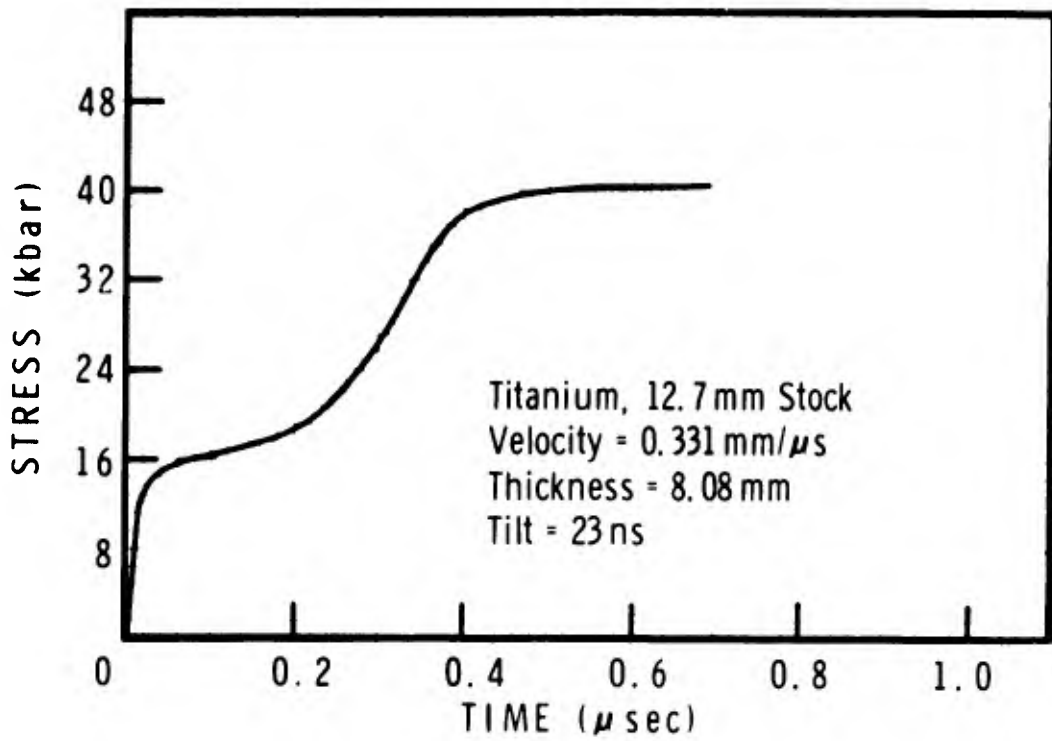
MSL-70-23, Vol. IV

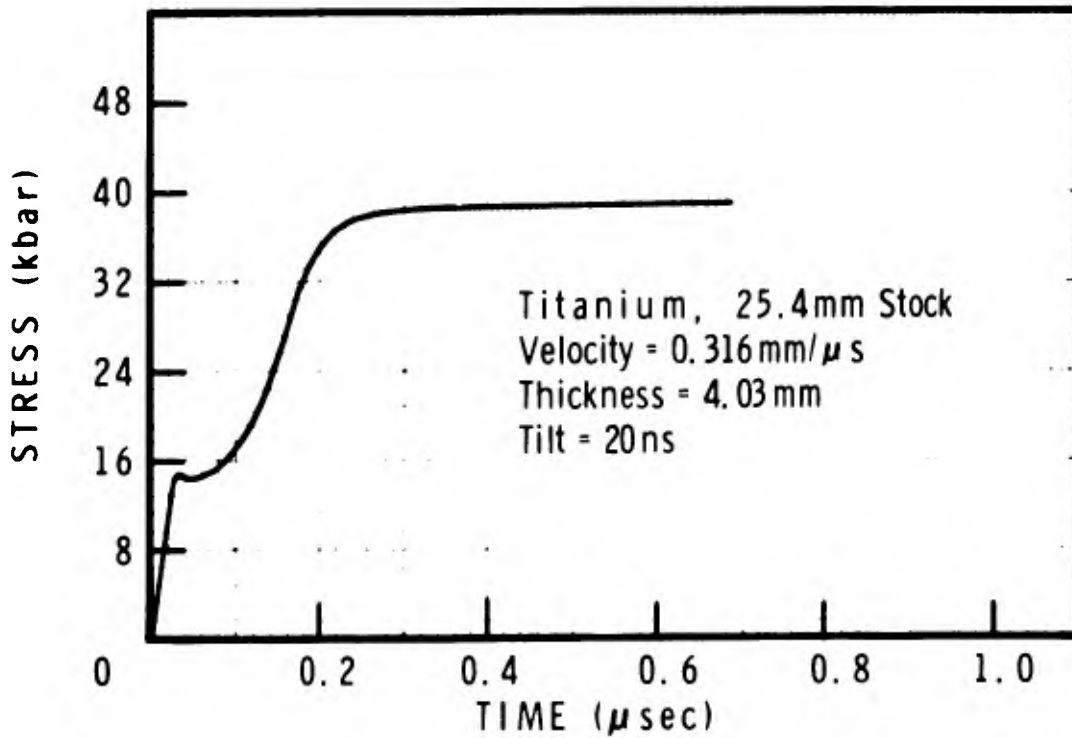
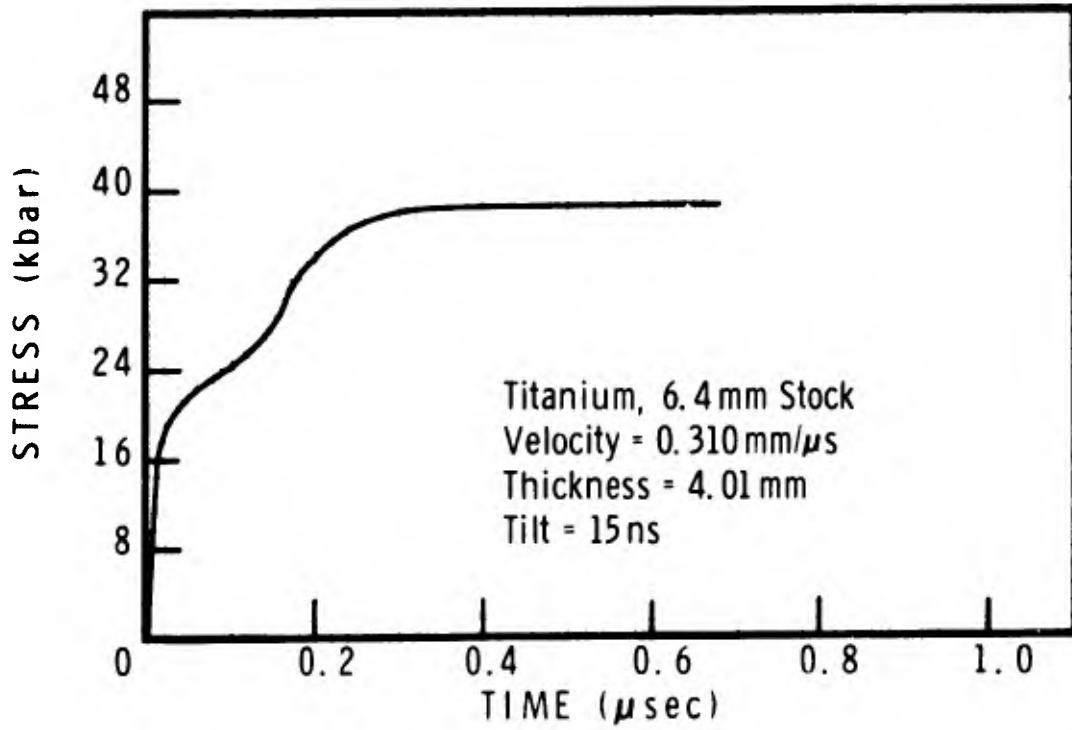




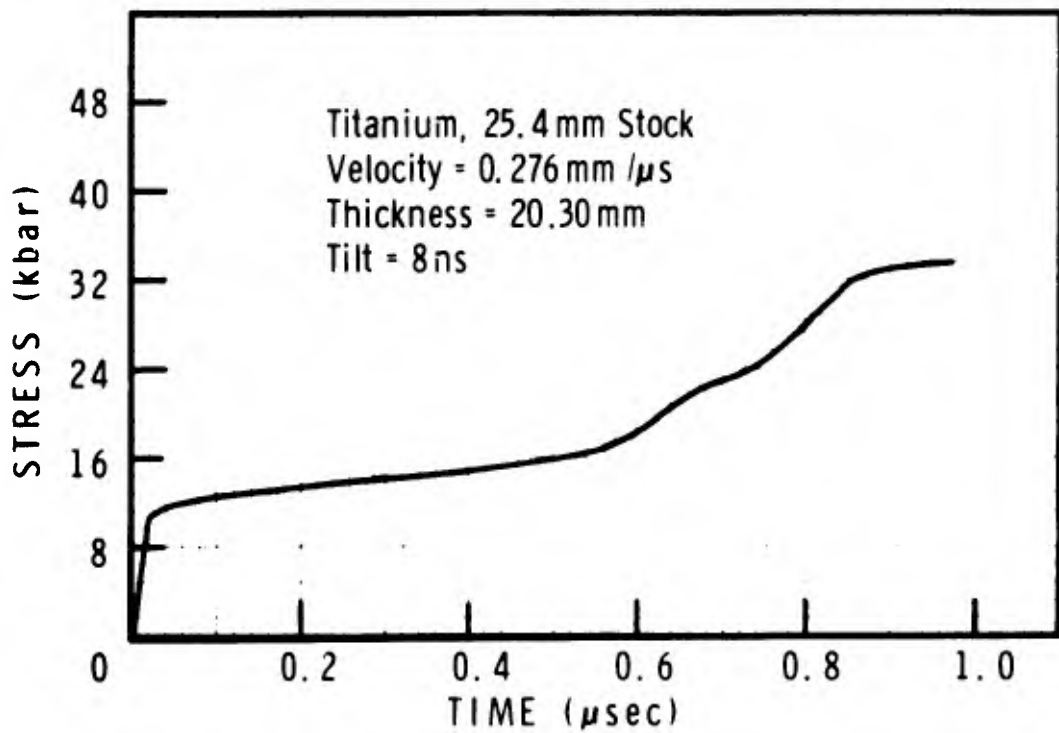
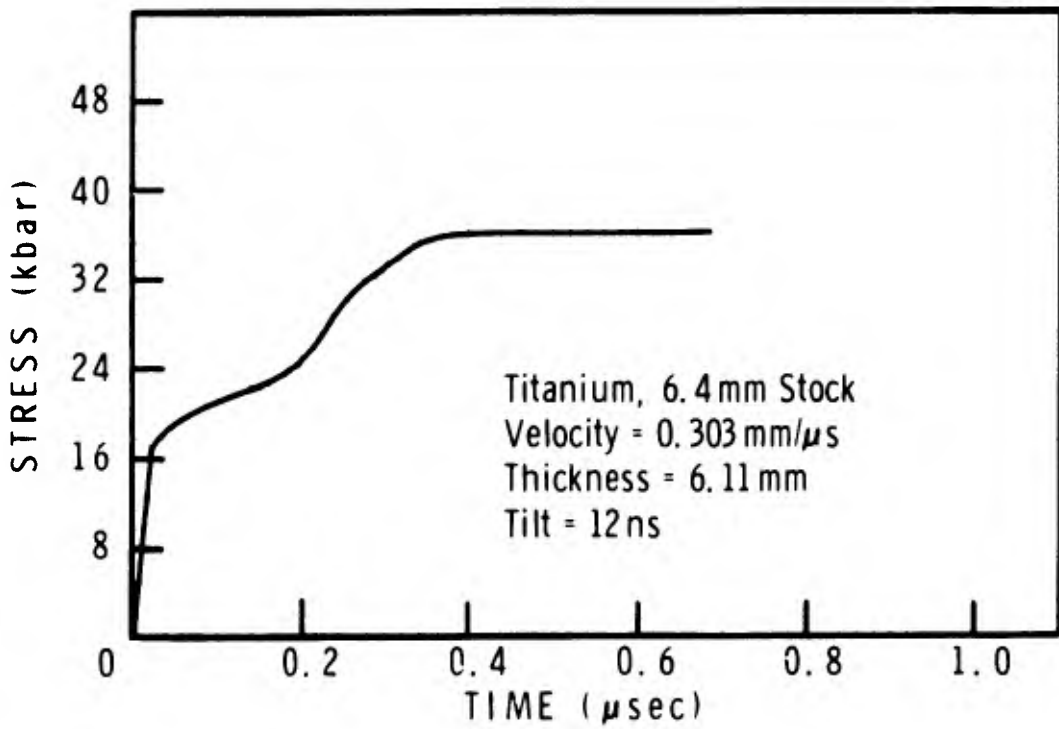


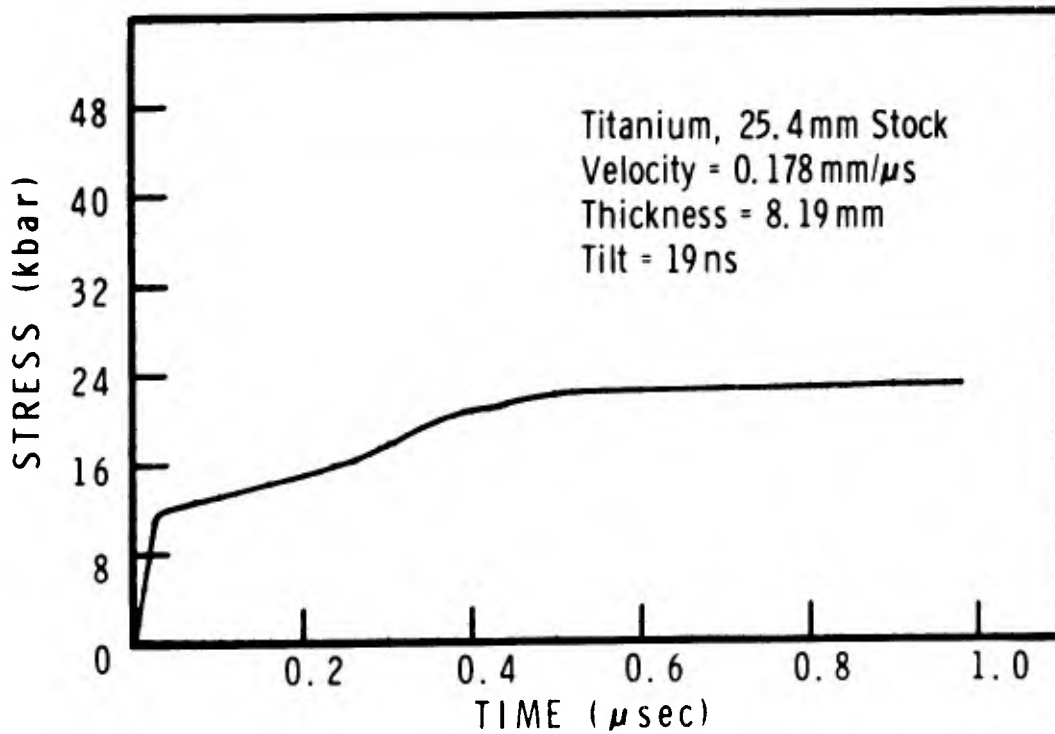
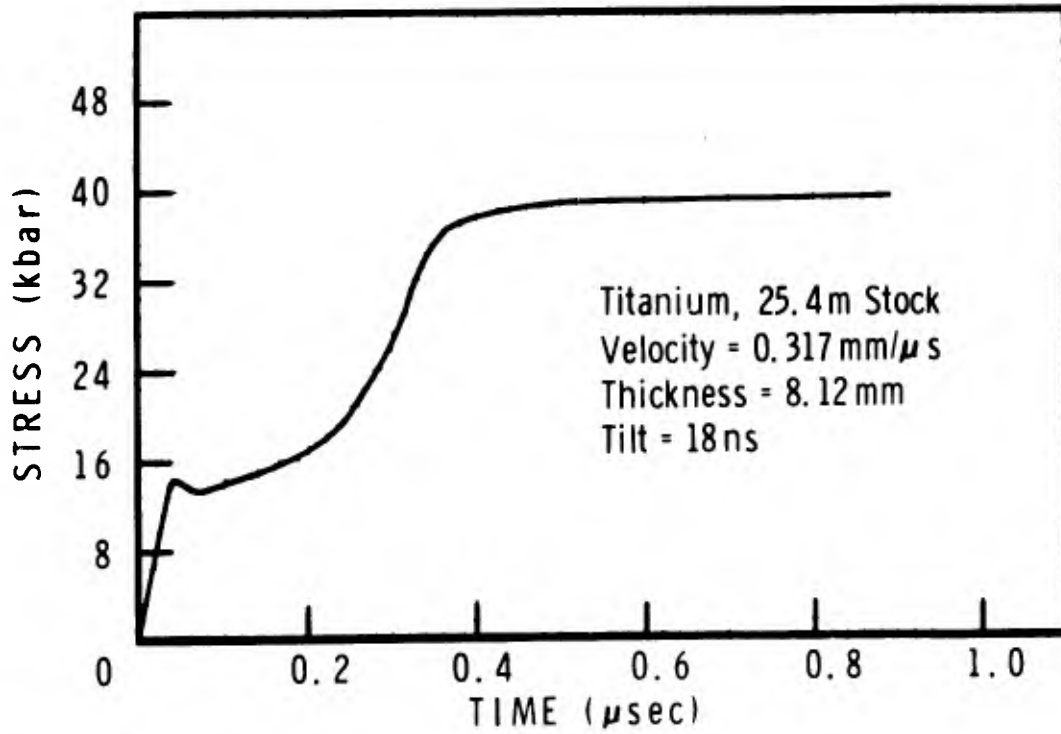
MSL-70-23, Vol. IV



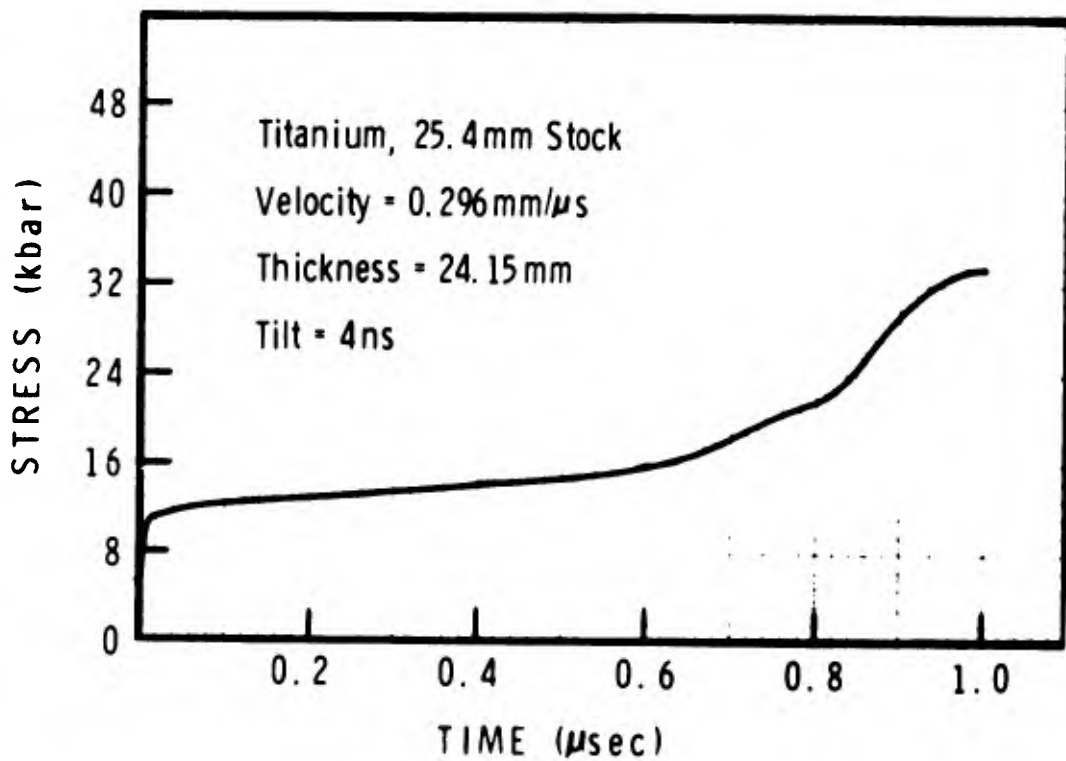
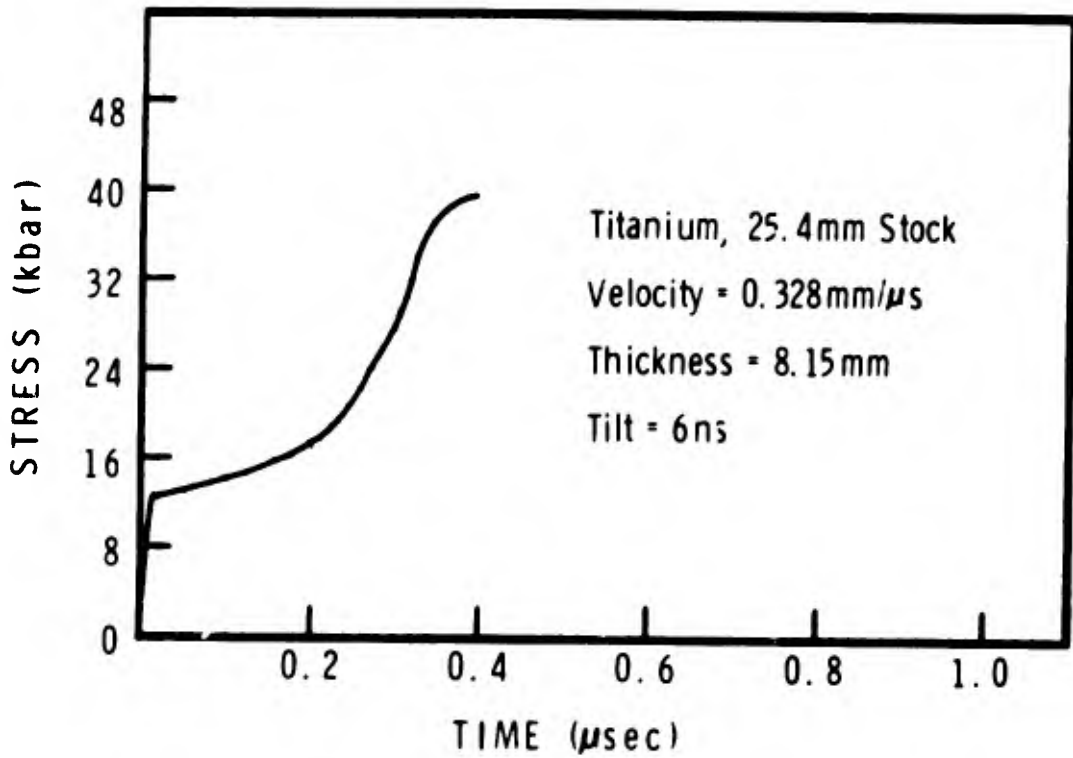


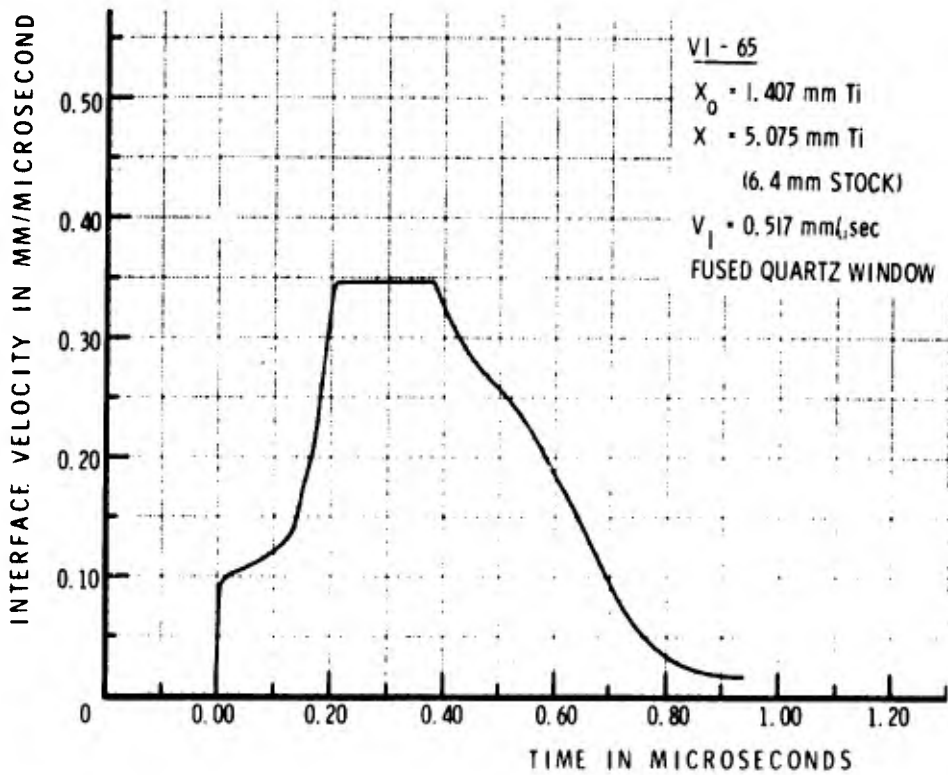
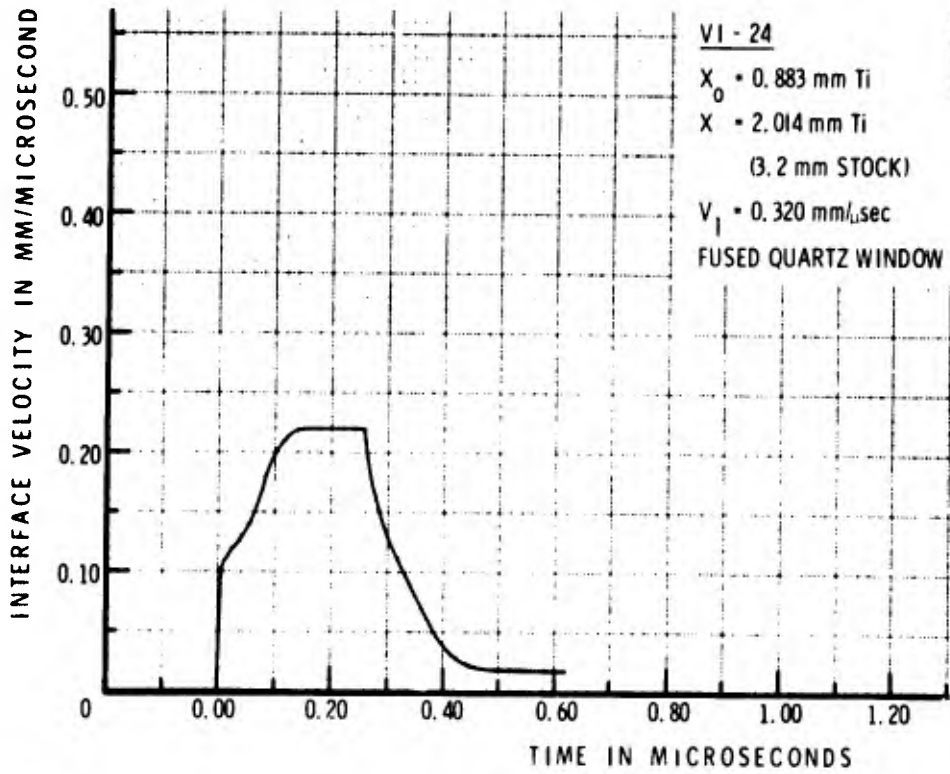
MSL-70-23, Vol. IV



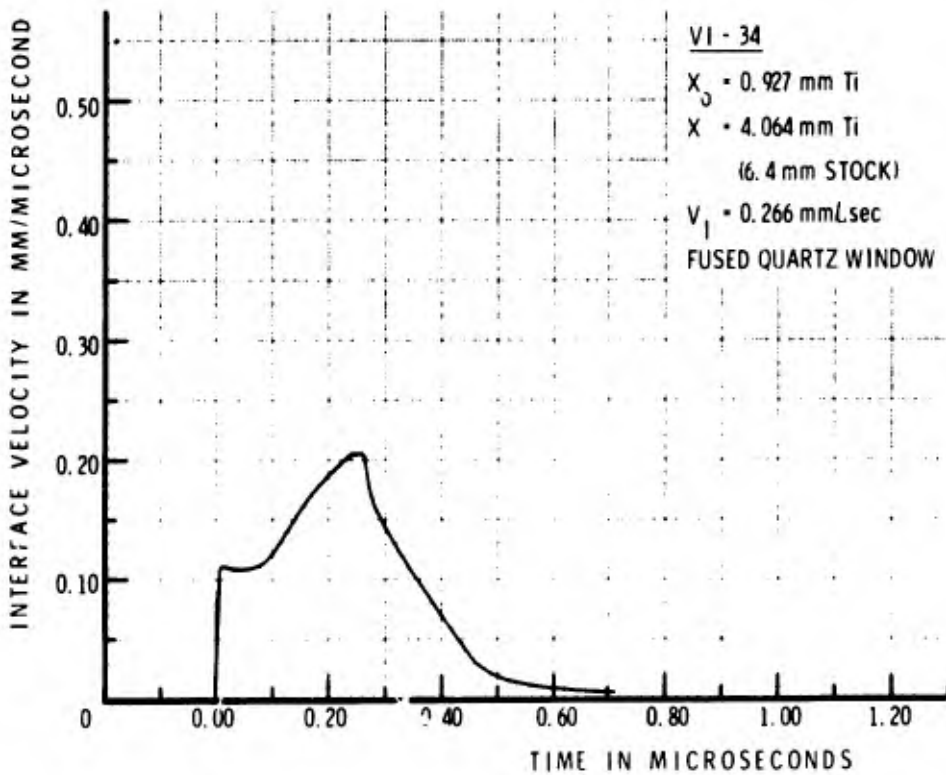
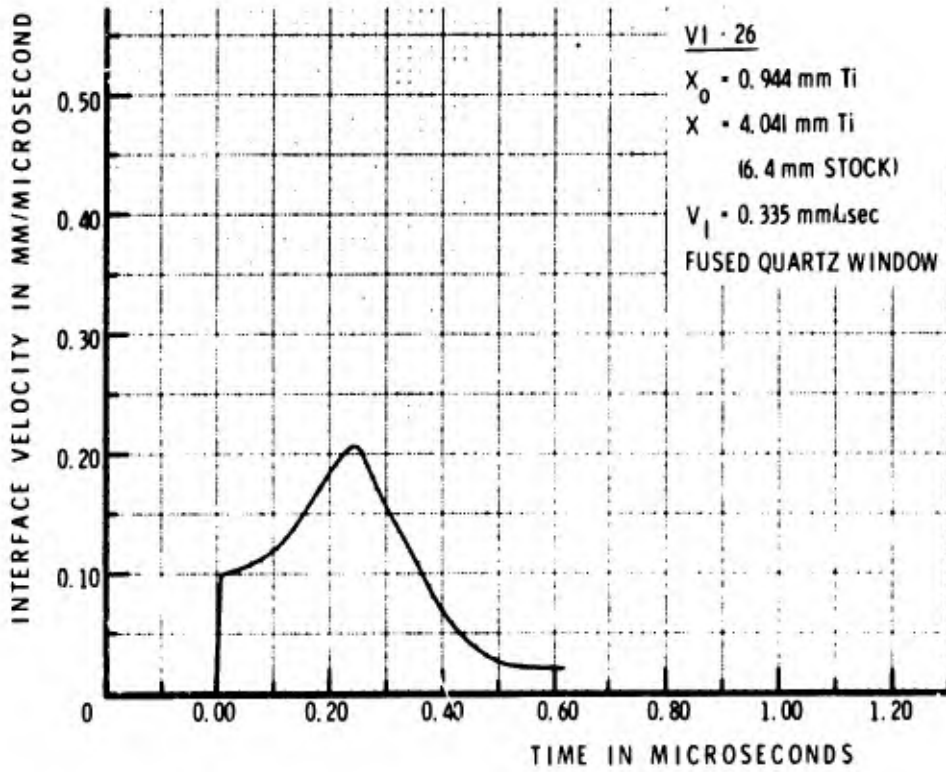


MSL-70-23, Vol. IV

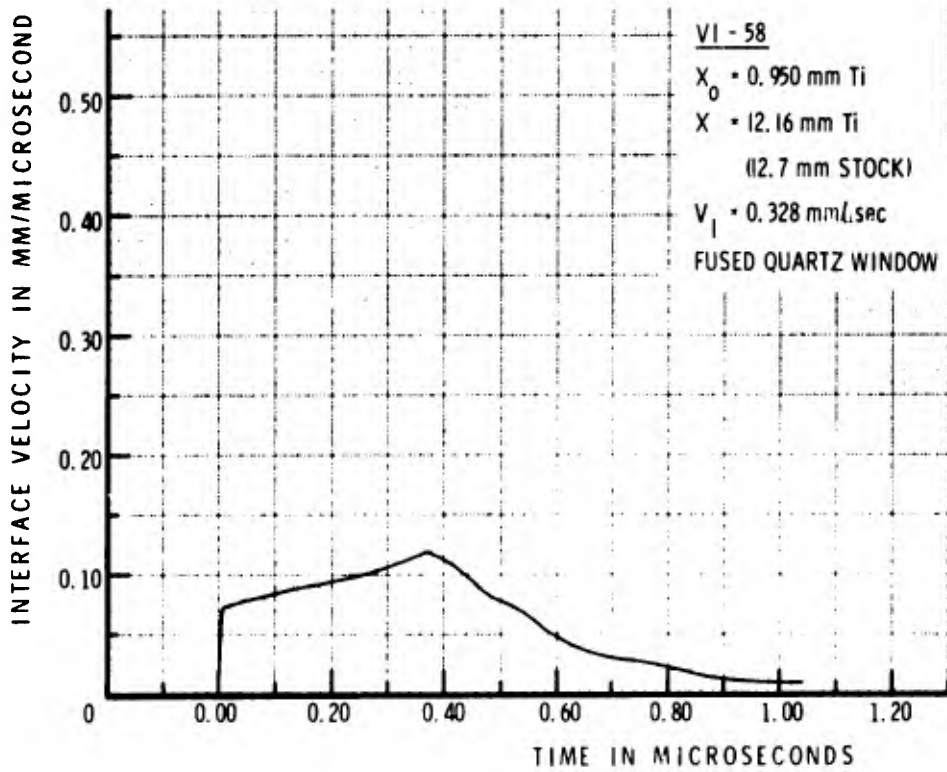
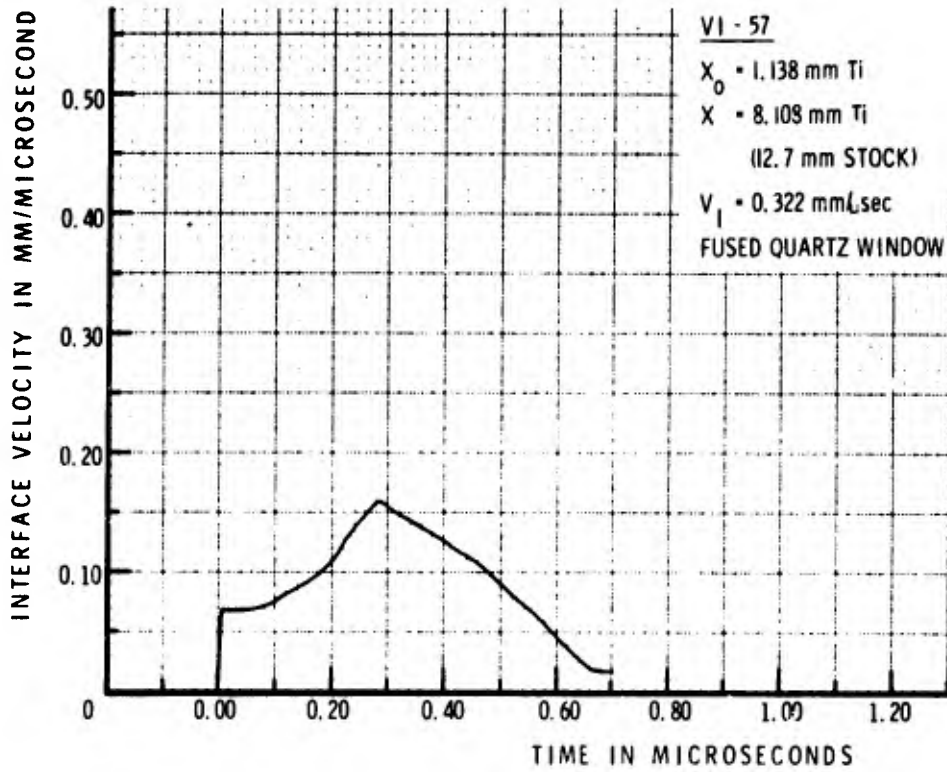




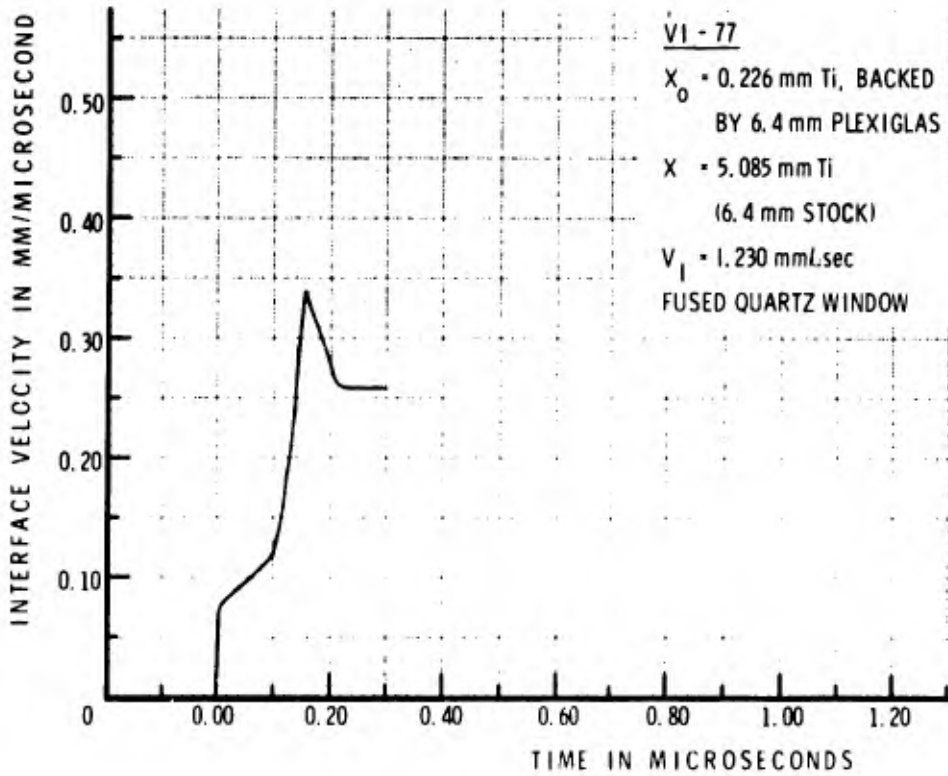
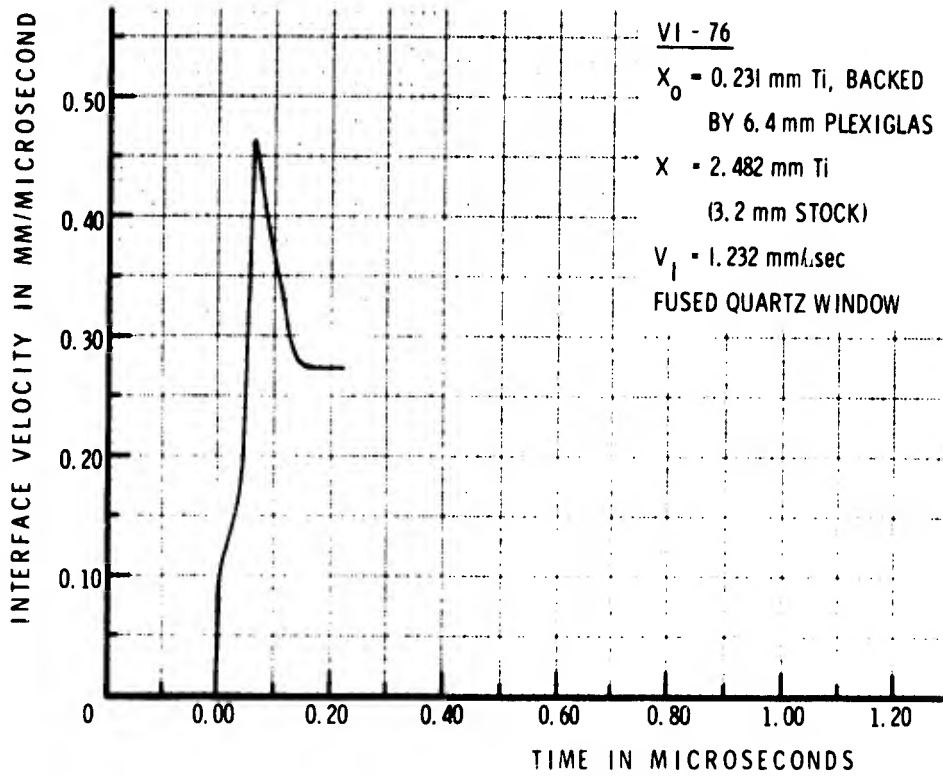
MSL-70-23, Vol. IV

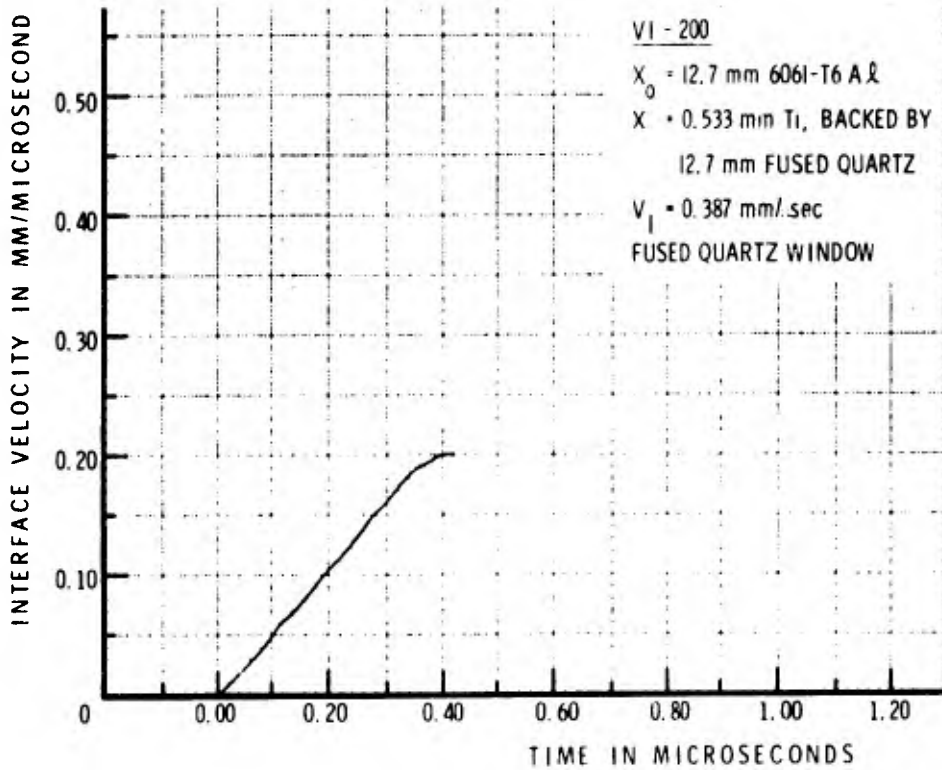
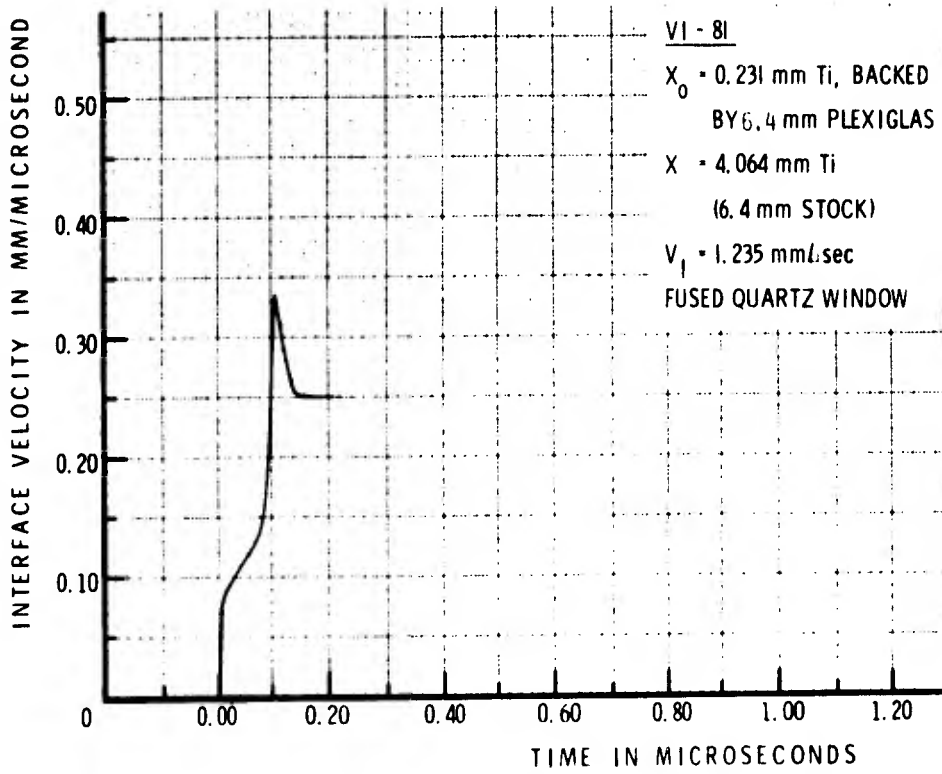




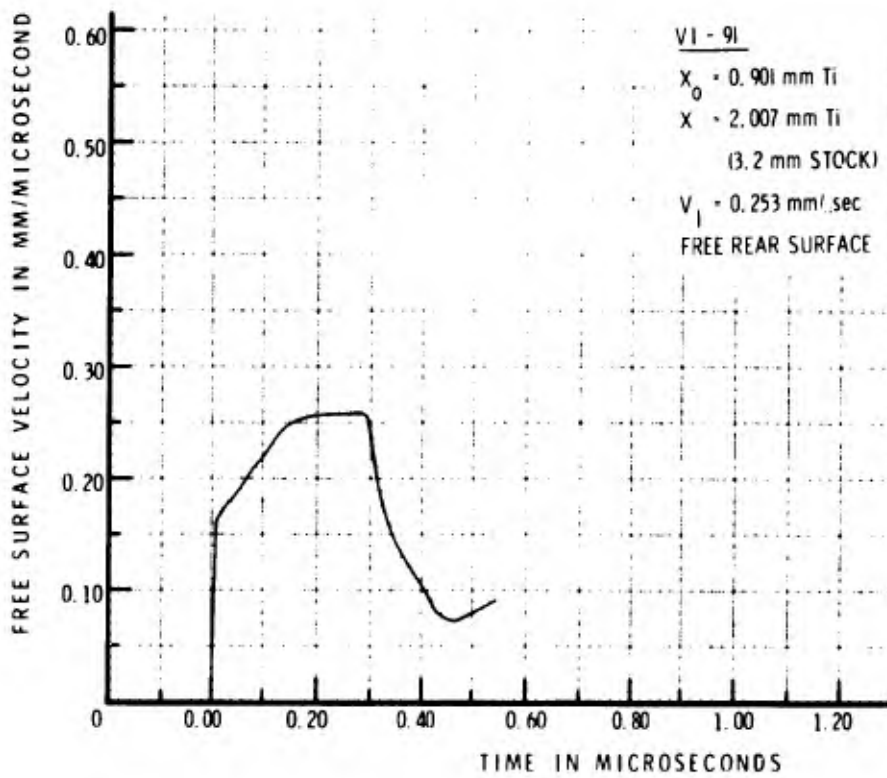
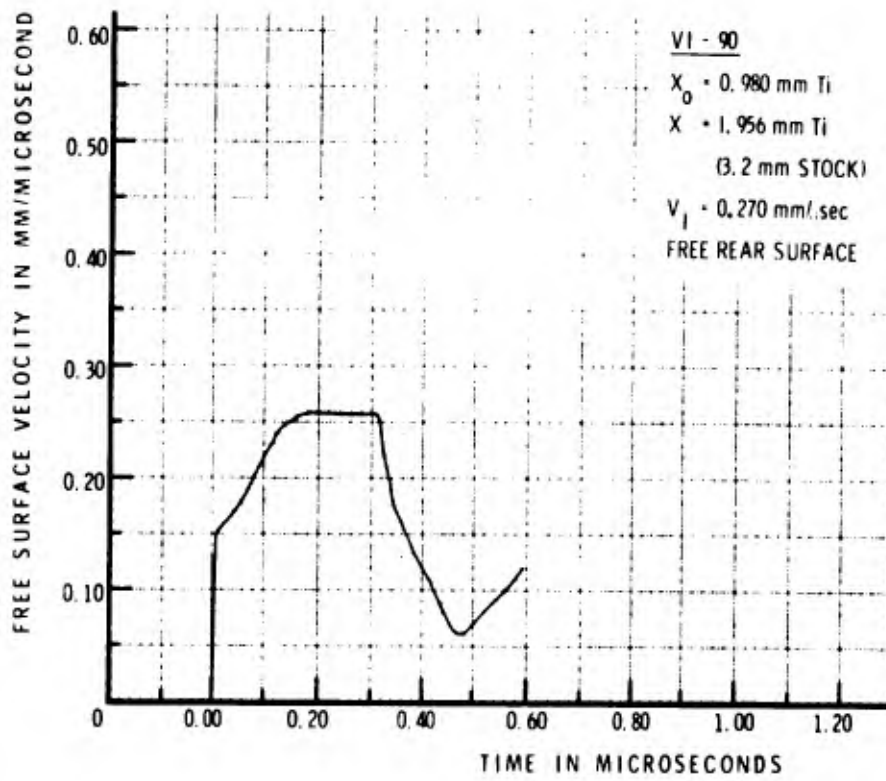


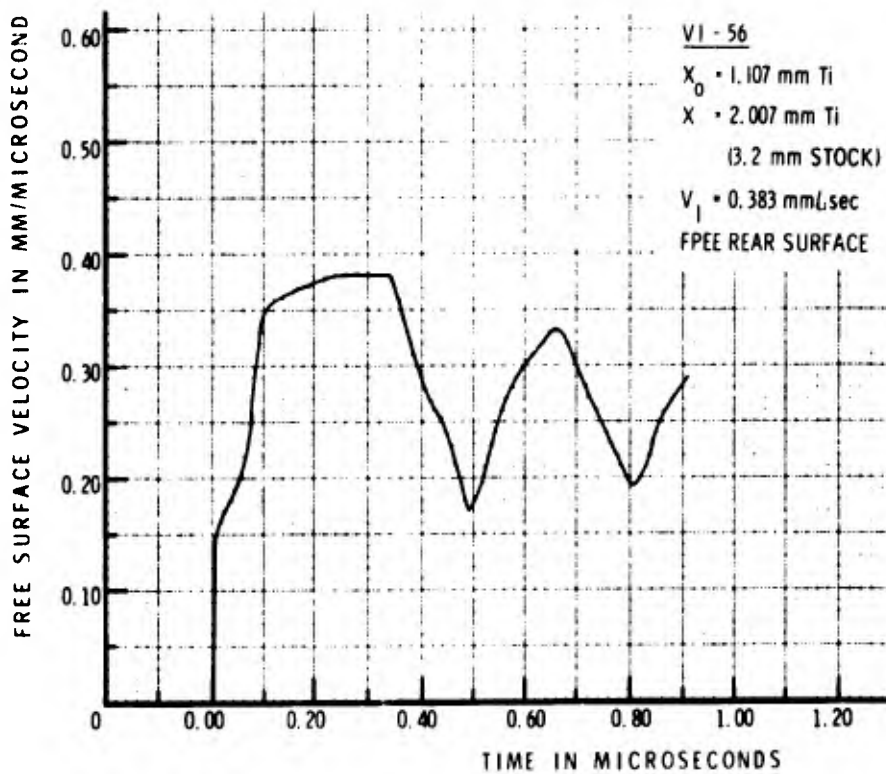
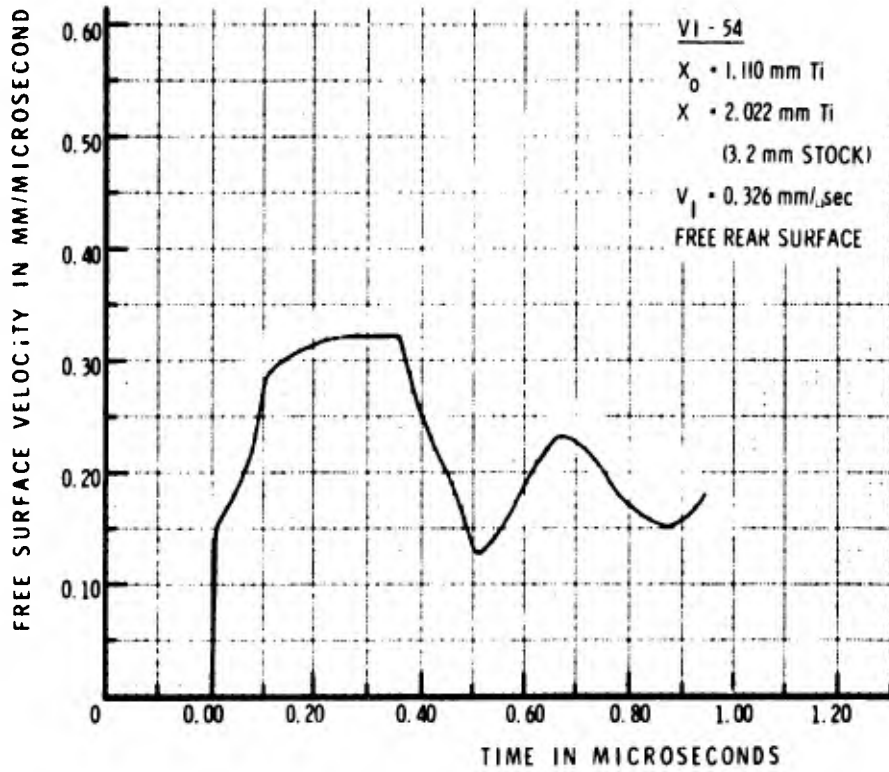
MSL-70-23, Vol. IV



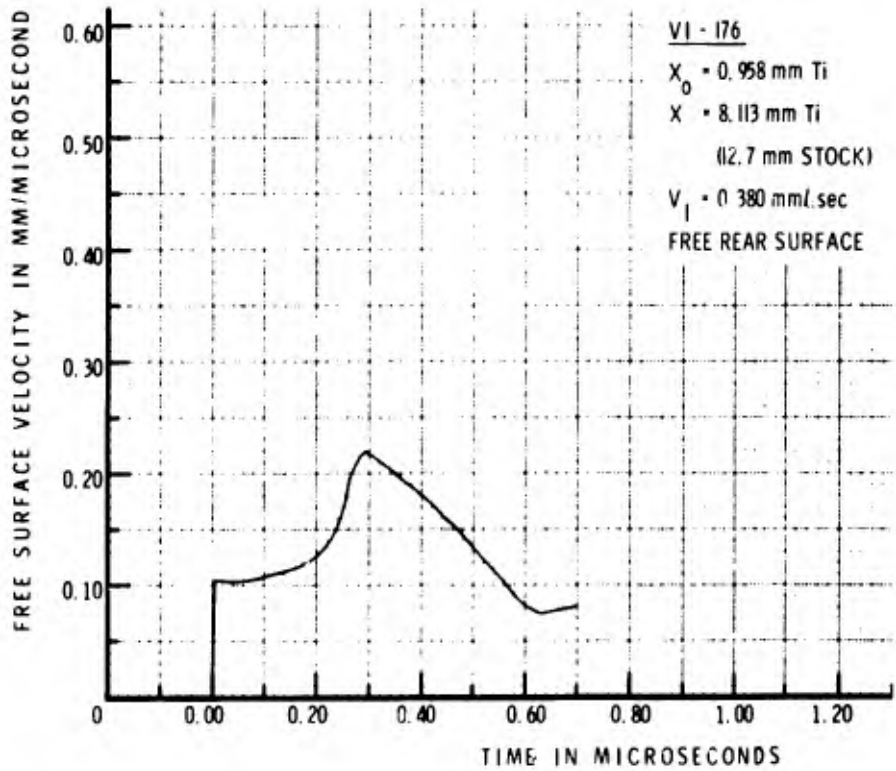
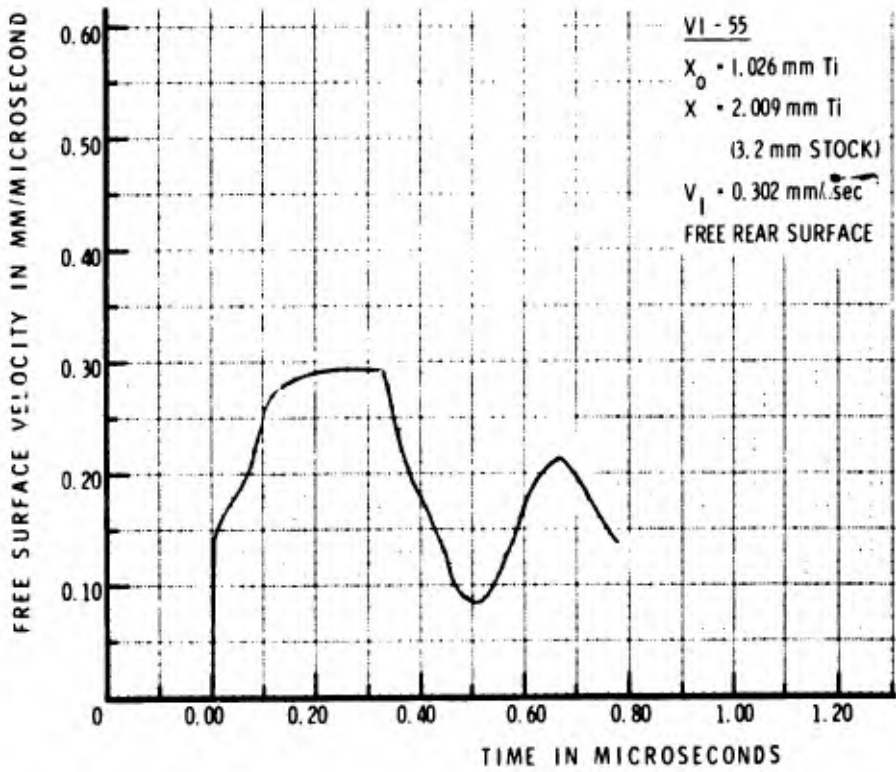


MSL-70-23, Vol. IV





MSL-70-23, Vol. IV



UNCLASSIFIED

Security Classification

DOCUMENT CONTROL DATA - R & D

(Security classification of title, body of abstract and indexing annotation must be entered when the overall report is classified)

1. ORIGINATING ACTIVITY (Corporate author) Manufacturing Development, General Motors Corporation, General Motors Technical Center, Warren, Michigan 48090		2a. REPORT SECURITY CLASSIFICATION UNCLASSIFIED	
3. REPORT TITLE Final Report - Measurement of Dynamic Properties of Materials Volume IV - Alpha Titanium		2b. GROUP	
4. DESCRIPTIVE NOTES (Type of report and inclusive dates) Final Report (in Six Volumes)			
5. AUTHOR(S) (First name, middle initial, last name) Douglas R. Christman, Thomas E. Michaels, William M. Isbell, Stephen G. Babcock			
6. REPORT DATE 1971 November	7a. TOTAL NO. OF PAGES 128	7b. NO. OF REFS 71	
8a. CONTRACT OR GRANT NO. DASA01-68-C-0114	9a. ORIGINATOR'S REPORT NUMBER(S) MSL-70-23, Vol. IV		
b. PROJECT NO. NWER XAXA	9b. OTHER REPORT NUMBER(S) (Any other numbers that may be assigned this report) DASA-2501-4		
c. Task & Subtask A106			
d. Work Unit 07			
10. DISTRIBUTION STATEMENT Approved for public release; distribution unlimited.			
11. SUPPLEMENTARY NOTES		12. SPONSORING/MILITARY AGENCY NAME(S) AND ADDRESS(ES) Director Defense Nuclear Agency Washington, D. C. 20305	
13. ABSTRACT Results of an experimental study on the dynamic properties of alpha titanium are presented. Areas studied included stress-strain-strain rate and reverse loading behavior, elastic constants, equation of state, compressive and release wave characteristics, and spall fracture. The material showed approximately elastic-plastic behavior with some strain hardening under uniaxial stress compression (0.005 to 1000/sec strain rates). The material also exhibited strain-rate sensitivity which was temperature dependent. Longitudinal and shear wave velocities at 20°C were 6.118 and 3.246 mm/μsec, and temperature and pressure dependence was also measured and various elastic constants were calculated. The shock wave equation of state (EOS) up to 90 kbar was determined as $\sigma_H = 2.5 + 225 u_p + 49.9 u_p^2$ . Shock wave measurements indicate a possible phase change between 90 and 125 kbars. The EOS was also calculated from the elastic constants and comparisons made with the shock wave EOS. Compressive wave tests showed an elastic-plastic wave structure with a well-defined precursor. The impact velocity required for spall fracture was found to increase with decreasing pulse width, and to increase with increasing temperature.			

14 KEY WORDS	LINK A		LINK B		LINK C	
	ROLE	WT	ROLE	WT	ROLE	WT
Stress-strain-strain rate Reverse loading behavior Elastic constants Equation of state Compressive and release wave characteristics Spall fracture Phase change						